Electrical Characterization of Methyl-terminated n-type Silicon Microwire/PEDOT:PSS Junctions for Solar Water Splitting Applications

By

Sommayeh Asgari

Thesis Submitted to the Faculty of Graduate Studies in Partial Fulfilment of the Requirements for the Degree of Master of Science

Department of Electrical and Computer Engineering
University of Manitoba
Winnipeg, Manitoba

© Copyright
2014, Sommayeh Asgari

Abstract

The role of high doping levels and the interfacial structure on the junction behavior between n-type silicon microwires and the conducting polymer, PEDOT:PSS, was investigated using tungsten probes, an established technique for Ohmic contact to individual microwires. The resistance and the doping density of carriers as a function of length along each microwire as well as the junction resistance between individual microwires and the conducting polymer were characterized by making Ohmic contact to microwires. The junction between highly-doped n-Si microwires and the conducting polymer had relatively symmetric current-voltage characteristics and a significantly lower junction resistance as compared to low-doped microwires. The current-voltage response of junctions formed between the polymer and low-doped microwires, which still incorporated the metal catalyst used in the growth process, was also studied. Junctions incorporating copper at the interface had similar current-voltage characteristics to those observed for the highly-doped microwire, while junctions incorporating gold exhibited significantly lower resistances.

Acknowledgments

During my study in University of Manitoba, I have received guidance and support from a lot of people. Firstly, I would like to express my immense appreciation to my supervisor, Dr. Derek Oliver for his support and insightful guidance in my research, his door was always open to my countless enquiries. This thesis would not have been possible without all of his guidance (and patience) along the way. I also thank them for his generous help in the non-academic area.

I would also like to express my deepest gratitude to my co-supervisor, Dr. Michael Freund, who has provided me with valuable instruction in every stage of my graduate study. Without his enlightening guidance, impressive kindness and patience, I was not able to complete my graduate study. His keen and vigorous academic observations enlightened me not only in this thesis but also in preparation of my technical papers.

My sincere thanks also go to Iman Yahyaie for training me to work with the SPM and Probe Station. I also gratefully acknowledge his patience and valuable aids in dealing with many problems I faced during my research.

I would also like to thank Shain Ardo, Mike McDonald, Kevin McEleney, and Jared Bruce for all the academic discussion and happy time working with them. I would like to express my special thank to Shain Ardo and Jared Bruce for fabrication of microwires for

this study. I shall extend my thanks to all my friends for their care, support and encouragement.

My thanks also go to my beloved parents for their love and great encouragement to me through all these years. Thanks to my husband Siamak for his understanding and love during the past years.

Contents

Front Matter

1 CHAPTER I: INTRODUCTION......1

1.1 SOLAR WATER SPLITTING CELLS......1

1.2 PROBLEM DEFINITION AND MOTIVATION......3

1.3 THESIS ORGANIZATION......7

CHAPTER II: THEORY AND REVIEW......8

2.1 WATER SPLITTING CELLS......8

2.1.1 Bulk electrical properties of Solar cells......13

2.1.2 Photoelectrode Materials......15

2.1.3 Surface Functionalization of Silicon......17

2.1.4 Nano- and Micro-photoelectrodes......18

2.1.5 Crystalline Silicon Microwire Array Growth......21

2.2 CANDIDATE MEMBRANE SYSTEMS......24

2.3 THE POLYMER/MICROWIRE SYSTEMS: REQUIREMENTS......27

2.4 PEDOT:PSS/SILICON ASSEMBLY......29

CHAPTER III: EXPERIMENTAL METHOD......40

3.1 SILICON MICROWIRES......42

3.1.1 Highly-doped Microwires: n^+-Si......42

3.1.2 Highly-doped Base Microwires: nn^+-Si......43

3.1.3 Metallic-capped Microwires: Cu/nn^+-Si 43

3.1.4 Metallic-capped Microwires: Au/nn^+-Si 44

3.2 OHMIC-CONTACT TO SILICON MICROWIRES 44

3.3 PEDOT:PSS/SI MICROWIRE ASSEMBLY 47

3.4 INSTRUMENTATION 49

CHAPTER IV: RESULTS AND DISCUSSION 52

4.1 RESULTS 52

4.1.1 Resistance Measurement of Single Microwires 54

4.1.1.1 Highly-doped Microwires: n^+-Si 57

4.1.1.2 Highly-doped Base Microwires: nn^+-Si 59

4.1.1.3 Metallic-capped Microwires: Cu/nn^+-Si 62

4.1.1.4 Metallic-capped Microwires: Au/nn^+-Si 64

4.1.1.5 Electrical properties of n-Si Microwires 66

4.1.2 PEDOT:PSS/Si Microwire Junction 66

4.1.2.1 PEDOT:PSS/nn^+-Si Microwires 67

4.1.2.2 PEDOT:PSS/n^+-Si Microwires 70

4.1.2.3 PEDOT:PSS/Cu/nn^+-Si Microwires 71

4.1.2.4 PEDOT:PSS/Au/nn^+-Si Microwires 72

4.1.2.5 PEDOT:PSS/modified n-Si Microwires 73

4.2 DISCUSSION 74

4.2.1 PEDOT:PSS/nn^+-Si 74

4.2.2 PEDOT:PSS/n^+-Si 77

4.2.3 PEDOT:PSS/Cu/nn^+-Si 79

4.2.4 PEDOT:PSS/Au/nn^+-Si 80

CHAPTER V: CONCLUSIONS AND FUTURE DIRECTIONS 82

5.1 CONCLUSIONS 82

5.2 FUTURE DIRECTIONS 83

List of Tables

Table 4.1: The results of resistance measurements on n-Si microwires using direct-contact technique by means of tungsten probes (W). Apart from the microwires with the copper and gold interface (1.0 μm in diameter) the microwires were 1.5 μm in diameter. R_w is representation of the maximum resistance one might obtain for the length of the wire. The intercept of the line fitted to the resistance versus probe separation data presented tungsten probe-microwire contact resistances (R_c) contributed in the resistance measurements. 66

Table 4.2: The total series resistance (R_{total}) and the current (I) at 10 mV for the combination of n-Si microwires and PEDOT:PSS with 7-10 μm of microwires embedded in the conductive polymer to the operational current. n is the doping concentration of carriers associated with the end of the microwires in contact with the polymer. 74

Table 4.3: The tunnelling current (I) at 10 mV, the junction resistance (R_J) and depletion layer width (W) obtained from the theoretical calculations and experiments for n^+n-Si microwires with 7-10 μm in contact with PEDOT:PSS. The microwires were ~60 μm length (~20 μm highly-doped and ~40 μm low-doped) and diameter of ~1.5 μm. In the case of calculations, the planar junctions were assumed to have a contact area the same as PEDOT:PSS/n-Si microwires radial junctions (Sec 3.3). 75

Table 4.4: The tunnelling current (I) at 10 mV, the junction resistance (R_J) and depletion layer width (W) obtained from the theoretical calculation and experiments for ~80 µm long n^+-Si microwires with doping distribution of ~2×10^{20} cm^{-3} with an average diameter of 1.5 µm. For the calculations, the planar junctions were assumed to have a contact area the same as PEDOT:PSS/n-Si microwires radial junctions (Sec 3.3). 78

Table 4.5: The tunnelling current (I) at 10 mV, the junction resistance (R_J) and the barrier heights ($q\phi b$) obtained from the theoretical calculation and experiments for PEDOT:PSS/Cu/nn^+-Si microwires. The microwires were ~40 µm in length and ~1 µm diameter. The microwires were 7-10 µm in contact PEDOT:PSS from low-doped end with copper catalyst. For the calculations, the planar junctions were assumed to have a contact area the same as PEDOT:PSS/n-Si microwires radial junctions (Sec 3.3). 79

List of Figures

Figure1.1: Schematic of a typical PEC device and its basic operation mechanism for hydrogen generation from water splitting. 3

Figure 1.2: Schematic diagram of the proposed artificial photosynthesis system. A portion of sunlight is absorbed by the photoanode and produces electrons and holes. The photogenerated holes oxidize water to hydrogen ions (protons) and oxygen molecules. The hydrogen ions move to the chamber with photocathode via the membrane. The portion of sunlight passed through the photoanode and the membrane is absorbed by the photocathode and generates electrons and holes. The photogenerated electrons reduce the hydrogen ions and then produce hydrogen. The membrane must be electrically and ionically conducting to transfer the photogenerated electrons/holes and generated hydrogen ions between the chambers. 4

Figure 2.1: Energy diagram of a single band-gap semiconductor (E_g > 1.23 eV) vs oxygen evolution reaction (OER) and hydrogen evolution reaction (HER) for overall water splitting. The semiconductor absorbs the incident light and generates electron-hole pairs. The photogenerated electrons and holes find their way to the semiconductor/ solution interface to participate in HER and OER. 9

Figure 2.2: The solar energy spectrum under AM1.5G irradiance (where angle between the overhead and actual position of the sun is 48°). The materials with smaller band-gap absorb a larger fraction of the solar energy than those with smaller band-gap, resulting in a higher solar conversion efficiency [32, 37]. Adapted with permission from [37]. Copyright (2012) Optics express. 11

Figure 2.3: Energy diagrams for a dual band-gap water splitting system with photo-anode and photo-cathode photoelectrodes electrically connected in series. 12

Figure 2.4: Functionalization of Si(111) surfaces by introducing methyl groups on the surface. 18

Figure 2. 5: Schematic of a PEC device (a) based on planar photoelectrodes and (b) based on nano- and micro photoelectrodes. 19

Figure 2.6: Photogenerated carriers (white and black circles) in a planar system (a) travel the entire thickness of the device, ~1/α, before collection, while in a microwire array assembly (b) with appropriate dimensions, carriers reach the microwire surface before recombination. 20

Figure 2.7: a) Schematic diagram of VLS-growth of Si microwire arrays [90], b) SEM images of a microwire array taken by 10 kV-500X (the magnified image on the left is taken by 10 kV-2500X). 23

Figure 2.8: Schematic diagram of the proposed artificial photosynthesis system. The components are: light harvesting electrodes (one absorber acting as a photocathode and the other as a photoanode); a membrane barrier for separating the products of the oxidation and reduction reactions in two chambers; and redox catalysts. 25

Figure 2.9: Chemical structure of Poly (EDOT) based on 3,4-ethylenedioxylthiophene or EDOT monomer.. 26

Figure 2.10: Chemical structure of conducting polymer PEDOT PSS............................ 27

Figure 2.11: Energy band diagram of a conducting polymer junction with (a) n-semiconductors in contact before (left) and after establishment of electrochemical equilibrium (right) and (b) p-semiconductors in contact before (left) and after establishment of electrochemical equilibrium (right). 30

Figure 2.12: Energy-band diagrams showing transport mechanisms in a Schottky diode (on n-type degenerate semiconductor) under (a) forward bias and (b) reverse bias. TE = thermionic emission. TFE = thermionic-field emission. FE = field emission [30]. 31

Figure 2.13: Band diagrams of Schottky barrier junctions for n- Si with $n \sim 10^{18}$ cm^{-3}, $n \sim 10^{19}$ $cm^{-3}$and $n \sim 10^{20}$ cm^{-3}; the Fermi energy levels for different doping density obtained from eq 2.3. 32

Figure 2.14: n-Si and p-Si microwire provide the photovoltage needed to evolve O_2 from H_2O and are embedded into a membrane that separate the products............................... 35

Figure 2.15: The energy level positions of Fermi levels (E_f) and conduction band (CB) of PEDOT:PSS/n-Si before and after establishment of electrochemical equilibrium; the Fermi energy levels for different doping density obtained from eq 2.3 for n-Si with $\boldsymbol{n}$~10^{16} cm^{-3}. 36

Figure 2.16: Metal deposition on Si and formation of silicide by thermal annealing. 38

Figure 3.1: Schematic diagram for junction between PEDOT:PSS and methyl-terminated n-type silicon microwires (a) highly-doped microwires (~10^{20} cm^{-3}), (b) highly- doped

base microwires with highly-doped base in contact (~10^{19} cm^{-3}), (c) highly- doped base microwires with low-doped end in contact (~10^{18} cm^{-3}), (d) highly- doped base microwires with copper (Cu) interface at low-doped end (e), and highly- doped base microwires with gold (Au) interface at low-doped end 41

Figure 3.2: Optical micrographs of microwires isolated on a glass substrate. 44

Figure 3.3: a) Optical micrograph of an isolated Si microwire on a glass substrate. The tungsten probes are approaching from the above to make contact with the microwire. It is possible to move microwire along the microwire and make resistance measurement at different probes spacing. b) Schematic diagram for resistance measurement along an individual Si microwire using tungsten probes [109]. 46

Figure 3.4: (a) The design used to the test half cell of artificial photosynthesis cells in this study. The thickness is t~ 200 nm, the width is W~ 2.5 cm and the length L ~ 0.5 cm for PEDOT:PSS thin film spin coated on a glass substrate. (b) Optical micrograph of a Si microwire embedded in to the polymer. 48

Figure 3.5: (a) Schematic diagram for a single microwire/polymer junction. It displays a microwire aligned at the polymer border and contact gold pads on the polymer films to provide Ohmic contact between the polymer and tungsten probe. (b) Optical micrograph of the half cell of artificial photoelectrolysis system under test. 49

Figure 3.6: *I-V* measurements were performed using an *Agilent 4155c* semiconductor parameter analyzer in a standard probe station. The stage, four W probe holders and the microscope are shown in the right side image. W probes can be seen in the magnified image on the left. 50

Figure 4.1: Schematic diagram of polymer/n-Si microwire junction measurements. This structure is used as a representation for the water splitting half-cell system in which n-type Si microwires aligned at the PEDOT:PSS /glass border.. 53

Figure 4.2: An example of the initial I-V measurement results for the probe spacing ~5µm on the n-Si microwire (120 µm long) with ~1 µm diameter and doping density of ~ 10^{19} cm^{-3} ,which was consistent with the expectation. 55

Figure 4.3: Contact formation along individual n-Si microwires (~1µm in diameter and ~120µm long) to make resistance measurement versus probe separation....................... 56

Figure 4.4: Contact resistance measurements for n^+-Si microwires with 1.5 µm diameter. The results shown here represent one microwire and were verified by repeating the experiment with other microwires from different regions of the growth substrate received in a batch. The linearity of the data along the length of microwires (squares) reflects the uniformity of the doping concentration within each region at the length scale considered. 58

Figure 4.5: Contact resistance measurements for nn^+-Si microwires with 1.5 µm diameter. Three independent measurements were carried out for each selected point along the microwire and were conducted in both directions, from (a) the top to the base and (b) the base to the top. The results shown here represent one microwire and were verified by repeating the experiment with other microwires from different regions of the growth substrate. The linearity of the data within the highly-doped base (diamonds) and remainder of the microwires (squares) reflects the uniformity of the doping concentration within each region at the length scales considered. 60

Figure 4.6: Contact resistance measurements for Cu/nn$^+$-Si microwires. These microwires were 1 μm in diameter. The results shown here represent one microwire and were verified by repeating the experiment with three other microwires from different regions of the growth substrate. Three independent measurements were carried out for each selected point. 63

Figure 4.7: Contact resistance measurements for Au/nn$^+$-Si microwires. The results shown here represent one microwire and were verified by repeating the experiment with other microwires from different regions of the growth substrate received in a batch. These microwires were 1 μm in diameter. Three independent measurements were performed for each selected point along microwire. 65

Figure 4.8: Schematic diagram of polymer/n-Si microwire junction measurements. This structure is used as a representation for the water splitting half-cell. 67

Figure 4.9: I-V profile for (a) PEDOT:PSS/nn$^+$-Si microwires and (b) PEDOT:PSS/n$^+$n-Si microwires. The microwires were 60-70 μm in length (~20 μm highly-doped and ~40 μm low-doped) and ~1.5 μm in diameter. The highly-doped base was 7-10 μm in contact with the conducting polymer. (a) I-V curve was asymmetric (rectifying) for voltages < 1 V with a very large total resistance of R_{total} > 20 MΩ for voltages < 10 mV. (b) The junctions exhibited a symmetric I-V curve (Ohmic-like behavior) compared with PEDOT:PSS/nn$^+$-Si and a total resistance 4.5 ± 0.3 MΩ (< 10 mV).The results shown here represent one microwire and were verified by repeating the experiment with other microwires from different region of the growth substrate. 69

Figure 4.10: I-V characteristic for PEDOT:PSS/n$^+$-Si microwires. The microwires with ~80 μm length and diameter of ~1.5 μm were 7-10 μm in contact with the conducting

polymer. PEDOT:PSS/n^+-Si microwire demonstrated a symmetrical I-V curve at large bias voltage (< 1 V). I-V curve is linear with end to end resistance of 4 ± 1 MΩ for small bias voltage (< 10 mV). The results shown here represent one microwire and were verified by repeating the experiment with other microwires from different region of the growth substrate. 70

Figure 4.11: I-V characteristic for PEDOT:PSS/Cu/nn^+-Si microwires. The microwires with ~40 µm length and diameter of ~1 µm were 7-10 µm in contact with the conducting polymer from low-doped end including copper catalyst. The presence of copper yielded a symmetrical I-V curve for large bias voltage (< 1 V). It also showed a linear I-V profile with total resistance of 3.4 ± 0.7 MΩ for small bias regime (< 10 mV). The results shown here represent one microwire and were verified by repeating the experiment with other microwires from different region of the growth substrate. 72

Figure 4.12: I-V characteristic for PEDOT:PSS/Au/nn^+-Si microwires. The microwires were ~120 µm in length and ~1 µm in diameter. They were 7-10 µm in contact with the conducting polymer from the low-doped end including gold catalyst. The presence of gold yielded a linear I-V profile for large bias regime (< 1 V) with a small total resistance of 0.15 ± 0.04 MΩ for small bias voltage (< 10 mV). The results shown here represent one microwire and were verified by repeating the experiment with other microwires from different region of the growth substrate. 73

Figure 4.13: The current pattern in (a) a large contact area and (b) a small contact area when r << L. 77

List of Copyrighted Material

K. D. Olson, and J. J. Talghader. "Absorption to reflection transition in selective solar coatings." *Optics express* (2012), vol. 20, no. 104, pp A555, Fig.1 11

C. Bulucea, "Recalculation of Irvin's resistivity curves for diffused layers in silicon using updated bulk resistivity data." *Solid-state electronics* 36.4 (1993), vol. 36, no. 4, pp. 489, Fig. 3...57

List of Symbols

Symbols and Constants

h	Planck constant; ~6.62× 10-34 m^2kg/s
$\hbar$	Reduced Planck constant; 1.05458×10^{-34} m^2kg/s
$h\nu$	Photon Energy
k_B	Boltzmann Constant; 1.38×10^{-23} JK^{-1}
m_0	Electron Mass; 9.1×10^{-31} kg
m^*/m_0	Effective Mass
n	Electron Density in the Conduction Band
p	Hole Density in the Valence Band
q	Charge on an Electron; 1.602×10^{-19}C
ΔE^0	Electrochemical Potential Difference Under Standard Conditions
s	Surface Recombination Velocities
A^{**}	The Effective Richardson Constant
α	Absorption Coefficient
ΔG	Free Energy Change
μ	Minority Carrier Mobility
ρ	Resistivity
τ	Minority Carrier Lifetime
Φ_b	Barrier Height
Φ_p	Work Function Of Polymer
Φ_{cu}	Work Function Of copper
Φ_{au}	Work Function Of gold
χ_S	Electron Affinity Of Semiconductor
Θ	Tunneling Probability
ε_o	Permittivity Of Vacuum; 8.85418~10-^{14} F/cm
V_R	Richardson Velocity
A	Cross-Sectional Area
Au	gold
C	Capacitance
Cu	copper
CH_3	methyl
CO_2	carbon dioxide

D	Minority Carrier Diffusion Coefficient; Dual Photosystem
E_c	Conduction Band-Edge Energy
E_F	Fermi Level Energy
E_g	Band-gap Energy
E_v	Valence Band-Edge Energy
H_2	hydrogen
H_2O	Water
HCl	hydrogen chloride
HF	Hydrofluoric Acid
I	Current
I_0	Reverse Saturation Current
I_{sc}	Short Circuit Photo-Generated Current
I_T	Tunneling Current
J	Current Density
J_0	Saturation Current Density
J_{SC}	Short-Circuit Current Density
J_g	Absorbed Photon Flux
KOH	potassium hydroxide
ℓ	Length
L_D	Minority Carrier Diffusion Length
N_C	Effective Density Of States in the Conduction Band
N_d	Doping Density
O_2	Oxygen
P	Phosphorus
P_t	Platinum
R	Resistance
R_s	Sheet Resistance
R_J	Junction Resistance
R_C	W Probe/Microwire Contact Resistance
R_w	Microwire Resistance
R_p	Polymer Film Resistance
R_{total}	Total Measured Resistance Of Half Cell Of Solar Water Splitting Device
Si	Silicon
t	Thickness
T	Absolute Temperature In Kelvin
TiO_2	Titanium Dioxide
V	Voltage
V_{oc}	Open-Circuit Voltage
W	Tungsten ; Width

Abbreviations

AM	Air Mass standardized solar irradiance
aq.	Aqueous
Caltech	California Institute Of Technology
CVD	Chemical Vapor Deposition
DC	Direct Current
EDOT	3,4-Ethylenedioxythiophene
HER	Hydrogen Evolution Reaction
NHE	Normal Hydrogen Electrode
OER	Oxygen Evolution Reaction
PEDOT	Poly(3,4-Ethylenedioxythiophene)
PEDOT:PSS	Poly(3,4-Ethylenedioxythiophene):Poly(Styrenesulfonate)
PH	Potential Hydrogen
PSS	Poly(Styrenesulfonate)
PV	Photovoltaic
VLS	Vapor-Liquid-Solid
SEM	Scanning Electron Microscopic
CB	Conduction Band
VB	Valence Band

Units

°C	Degrees Celsius
A	Ampere
eV	Electron Volt
g	gram
J	Joule
kg	kilogram
L	liter
m	Meter
cm	centimeter
mol	Mole, 6.02×10^{23} Elementary Entities of a Substance
Ω	Ohm
N	Newton
S	Siemens
V	Volt

Chapter One

Introduction

1.1 Solar Water Splitting Cells

There exists an increasing demand for new conversion and storage schemes for energy as a response to existing and projected increases in global energy consumption. The annual global consumption of energy is estimated to rise from 13.5 terawatt (TW), equivalent to 4.1×10^{20} joules/yr, in 2001 to 27 TW by 2050 and 43 TW by the end of the century [1, 2]. Most of the increased energy production is expected to come from the combustion of fossil fuels that currently power society. However, the finite reserves of fossil fuels fail to meet this enormous growing in the global demand for energy and burning fossil fuels leads to massive emissions of greenhouse gases which risk disrupting the climate. Solar energy is the largest (the solar radiation falling on the surface of the Earth is 120,000 TW [2, 3]) and the most easy accessible renewable energy resource on the Earth. There exist several different potential technologies to convert light into useful energy, including solar thermal conversion, photovoltaics, and photoelectrochemistry. Solar thermal systems concentrate the light from the sun to create heat, and that heat is used to run a heat engine, which turns a generator to make electricity. All of these

engines can be quite efficient, often between 30% and 40% in summer [4, 5]. They will be the major contributors in summer but they will not be as efficient in winter. The output during winter typically goes down to the level of 20% of the output during summer [4, 5]. Photovoltaic, or PV energy conversion, on the other hand, directly converts the sun's light into electricity (maximum efficiency of ~ 32%). This means that solar panels are only effective during daylight hours because storing electricity is not a particularly efficient process [6-8]. These two technologies discussed above are unable to provide electricity at night or during winter without the use of expensive storage technology such as batteries. A photoelectrochemical cell or PEC is an attractive solution to the energy storage problem which uses photogenerated charges to create new chemical bonds which can be stored as fuels. There are several potential photoelectrochemical systems, however the photo-electrolysis of water to produce hydrogen and oxygen are significantly focused in this field because hydrogen represents a potentially high-efficiency and environmentally clean fuel [9, 10].

In a photoelectrolysis cell (Fig 1.1), the semiconductor electrodes in contact with water produce electron-hole pairs when it is illuminated. In n-type semiconductor electrodes, the holes move to the surface and oxidize water to oxygen. The electrons separate from holes and flow to a second electrode and reduce water to hydrogen. In p-type semiconductor electrodes, the electrons reduce water to hydrogen and the holes separate flow to first electrode and oxidize water. The element is often used as fuel because of its high calorific value. Combustion generates plenty of energy. Hydrogen fuel cells generate electricity from oxygen and hydrogen. These electrochemical cells generate only water vapor so it is considered as environment friendly.

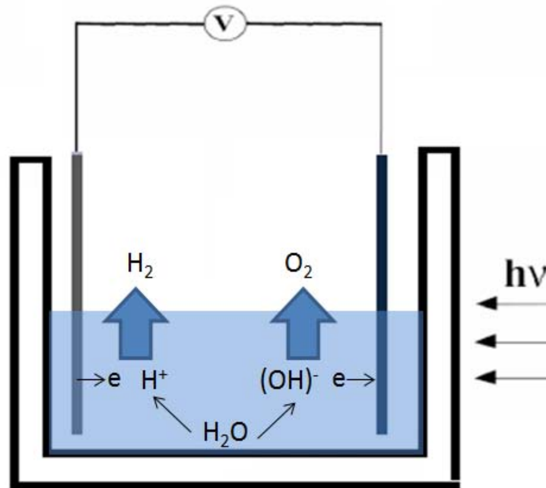

Figure1.1: Schematic of a typical PEC device and its basic operation mechanism for hydrogen generation from water splitting**.**

Having such a system with 10% efficiency and converging only 0.16% of the suns radiation on the surface of the Earth could yield 20 TW of power, which is nearly twice the rate of fossil energy being consumed in the world [2, 8]. The products of these systems, hydrogen, is a very light gas (0.08988 g/L), yielding a larger energy density (~140kJ/g) compared with any other fuels [11-13]. The products of these systems, hydrogen is utilized in a wide range of applications including internal combustion engines drive [13-15]; turbines drive for electricity production [8, 16].

1.2 Problem Definition and Motivation

Light-driven electrolysis of water is an attractive and potentially efficient method of conversion and storage of solar energy to chemical fuel in the form of a chemical bond, H-H. A proposed design for an efficient solar-driven water splitting system comprises

both p-type and n-type silicon microwire arrays embedded, in series, in a conducting polymer film (Fig 1.2) [9, 17-24].

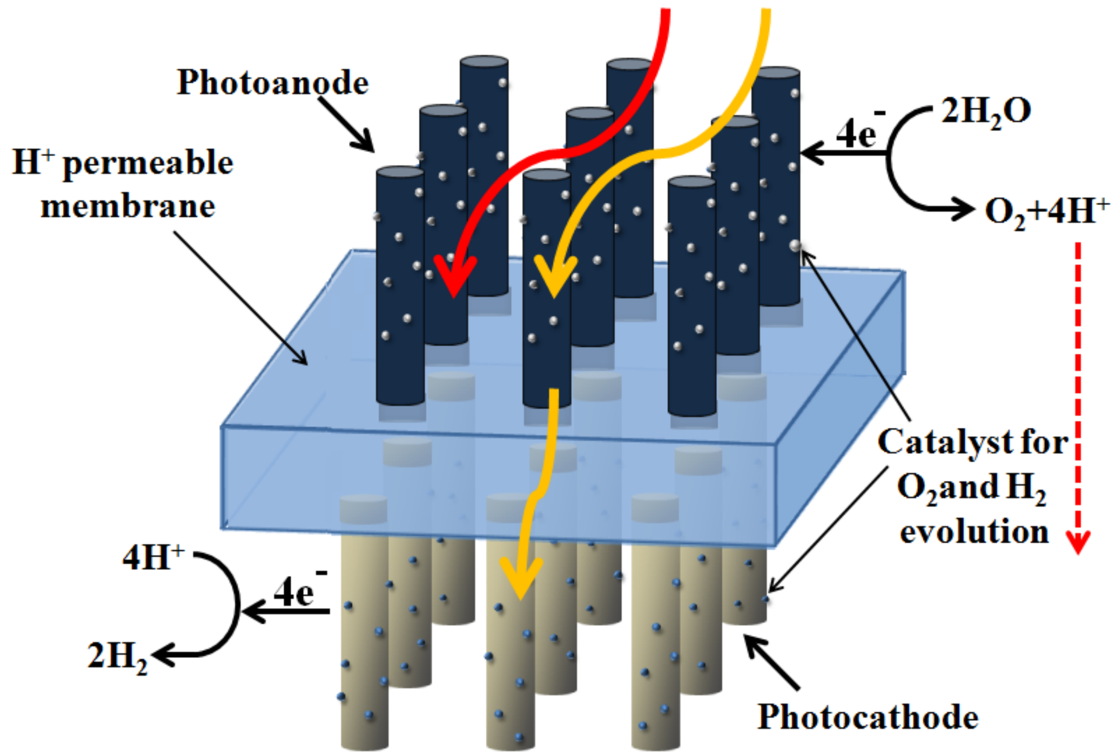

Figure 1.2: Schematic diagram of the proposed artificial photosynthesis system. Blue portion of sunlight is absorbed by the photoanode and produces electrons and holes. The photogenerated holes oxidize water to hydrogen ions (protons) and oxygen molecules. The hydrogen ions move to the chamber with photocathode via the membrane. Red portion of sunlight passed through the photoanode and the membrane is absorbed by the photocathode and generates electrons and holes. The photogenerated electrons reduce the hydrogen ions and then produce hydrogen. The membrane must be electrically and ionically conducting to transfer the photogenerated electrons/holes and generated hydrogen ions between the chambers.

Light incident upon the semiconductor with energy greater than the band-gap energy of the n-Si microwires (photoanodes) $hv > E_g$, results in the generation of an electron-hole pair. The photogenerated holes move toward the solution and the electrons are separated

and transferred via the membrane to the p-Si microwires (photocathodes). For the p-Si microwires (photocathodes), the photogenerated electrons moving to the surface and the holes transferred via the conducting polymer to the photoanodes. The photogenerated holes at the photoanode (n-Si) surface oxidize water molecules to form hydrogen ions (protons) and oxygen molecules, $2H_2O(l) \rightarrow O_2(g) + 4H^+(aq) + 4e^-$. The hydrogen ions are transferred via the membrane to the surface of the photocathodes (p-Si) in the reduction chamber. There they are reduced with photogenerated electrons at photocathodes surface, the result being H-H molecule via $2H^+(aq) + 2e^- \rightarrow H_2(g)$. A functional and effective water splitting system requires a membrane to act as a barrier to H_2(g) and O_2(g) diffusion in order to avoid recombination of water splitting products. The membrane needs to be electrically and ionically conducting to allow excess photogenerated charge carriers freely move across the system to maintain the overall charge neutrality; and the generated hydrogen ions be transferred to the reduction chamber. S. L. McFarlane *et al.* proposed a composite membrane, PEDOT:PSS/Nafion, for artificial photosynthesis applications made from an electronically conducting polymer, PEDOT:PSS (polyethylenedioxythiophene/polystyrene sulfonate) and an ionically conducting polymer, Nafion [25].

Absorption of photons with energy greater than the band-gap of the Si microwires array generates a maximum short-circuit photocurrent of ~21 nA per microware [26, 27]. Since the photogenerated electrons/holes in the photoanode/photocathodes should traverse the membrane to the photocathode/photoanode yielding the two half reactions of water splitting, the source of electrical loss must be minimized to effectively use the available photocurrent (photogenerated carriers) generated by the system to split water with

reasonable efficiency. The design consideration for such a device indicates that 0.5 MΩ end-end resistance of a single unit cell at 21 nA will result in an acceptable IR loss of less than 1% across the membrane in an ideal solar water splitting [27]. I. Yahyaie *et al.* explored the electrical properties of the junction between non-degenerate Si microwires and PEDOT:PSS/Nafion in which methyl-termination of the microwires was employed to avoid the formation of native oxides on the Si microwires and to improve the long-term stability of the conducting polymer/microwire junction performance [27, 28]. The studies showed an acceptable junction resistance ~ 0.1 MΩ for the junctions between a conducting polymer and methyl-terminated p-Si microwires [27-29]. However, the junction between methyl-terminated n-Si microwires and the conducting polymer showed a larger resistance (> 20 MΩ) far above the target [27-29]. The large junction resistance resulted from the formation of a Schottky barrier at the junction between the methyl-terminated n-Si microwires and the membrane [27-29].

There are two possible approaches to lower the effect of the Schottky barrier at n-Si microwire/membrane junctions, yielding an improvement on the electrical behaviour of this junction. One approach is raising the doping concentration of the microwires to lower the depletion region width [30]. A narrow depletion layer facilitates quantum mechanical tunnelling of the charge carriers, increasing the conductivity of the structure. Another possible approach is addition of a metallic interfacial layer to reduce the Schottky barrier height at the contact with semiconductor and make Ohmic contact with conducting polymer [30].

The electrical behavior of the junctions formed between a conducting organic polymer, PEDOT:PSS, and highly-doped microwires (n^+-Si) and highly-doped base microwires

(nn^+-Si, n^+ in contact) with doping density of 10^{19}-10^{20} cm^{-3} as well as the electrical behavior of junctions formed between the conducting polymer and the low-doped end of highly-doped base microwires (nn^+-Si, n in contact) with doping density of ~10^{18} cm^{-3} are investigated in this study. The current-voltage responses of the junctions with the presence of a metallic layer (copper or gold) at the polymer/microwires interface were also studied. These junctions are formed by embedding copper-capped (Cu/nn^+-Si) and gold-capped (Au/nn^+-Si) highly-doped based microwires in the membrane.

1.3 Thesis Organization

The following chapter of this thesis will overview the basic principles and components of the proposed solar water splitting devices and discuss the minimum electrical properties the systems required to work efficiently. Chapter 3 introduces the use of tungsten probes to make direct ohmic contacts to individual silicon microwires and single cells of the water splitting devices. Chapter 4 will present the results of individual silicon microwires and Si microwires/polymer systems and discuss how raising doping density of carriers and addition of metallic interfacial layer improved the electrical properties of the systems. Chapter 5 will conclude the results of measurements and researches performed in this study then discuss future directions for the project.

Chapter Two

Theory and Review

2.1 Water Splitting Cells

The goal of water splitting devices is conversion of pure water into O_2 and H_2; and decomposition of a molecule of water ($H_2O \rightarrow H_2 + ½O_2$) requires energy of ΔG = 237.2 kJ.mol^{-1} at 25 °C, which is equal to 2.48 eV per molecule of water. In other words, electrochemical potential difference ($\Delta E°$) of 1.23 V is required per electron transferred in a water electrolysis reaction [24]. In water splitting devices, the light harvested by the semiconductor materials is used to supply the required energy [10, 31]. Under irradiation, the photo-generated holes on the photoelectrode are used at the semiconductor/solution interface to oxidize water molecules to produce oxygen molecules (by-product) and hydrogen ions ($2H_2O(l) \rightarrow O_2(g) + 4H^+(aq) + 4e^-$, E^o = 1.23V) through an oxygen evolution reaction (OER). The electrons generated on the photoelectrode reduce hydrogen ions to generate hydrogen ($2H^+(aq) + 2e^- \rightarrow H_2(g)$, E^o = 0V) through a hydrogen evolution reaction (HER) [24]. The water splitting process can be driven by using a semiconductor material under illumination which has sufficiently wide band gap

energy (E_g); conduction band energy (CB) and valence band energy (VB) that brockets the electrochemical potentials associated with hydrogen and oxygen evolution reactions (Fig 2.1).

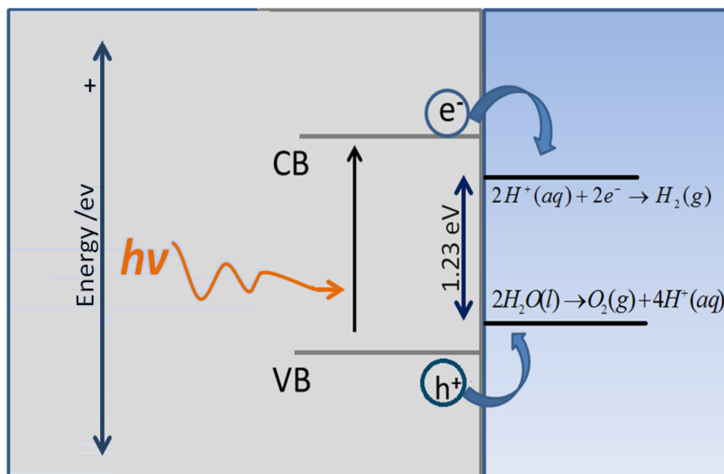

Figure 2.1: Energy diagram of a single band-gap semiconductor (E_g > 1.23 eV) vs oxygen evolution reaction (OER) and hydrogen evolution reaction (HER) for overall water splitting. The semiconductor absorbs the incident light and generates electron-hole pairs. The photogenerated electrons and holes find their way to the semiconductor/ solution interface to participate in HER and OER.

The above discussion indicated that the minimum energy needed to split the water molecule is 1.23 eV. In practice, the required energy is greater than 1.23 eV due to the energy loss contributions such as the resistance of the electrodes, the electrical connections, contacts; the combination of photo-generated electrons/holes; and polarization of the PEC [24, 32]. Hence, ~2 eV per electron-hole pair generated has been reported to be need for the photoelectrolysis operation to cover the estimated value of these combined losses [17, 24, 32, 33]. If a single semiconductor photoelectrode (single photosystem) is only used to absorb light for the water splitting process, the minimum

band-gap energy needed is greater than $E_g > 2$ eV ($\lambda < 620$ nm). The band-gap of the photo-absorber governs the fraction of the solar energy that can be absorbed since only photons with energy equal to or larger than that of the band-gap can be absorbed and used for the conversion. Materials with large band-gaps significantly limit light harvesting, leave out much of the solar spectrum, and reduce the maximum practically achievable efficiency (Fig 2.2) [32, 34, 35]. The theoretical efficiency for conversion of incident solar energy to chemical energy is expressed in eq 2.1.

$$\eta = \frac{J_g \mu_{ex} \varphi_{conv}}{S} \quad , \tag{2.1}$$

where J_g is the absorbed photon flux ($s^{-1}m^{-2}$) for energies > E_g of electrodes, μ_{ex} is chemical potential generated by light absorption in the system, φ_{conv} is the quantum yield for absorbed photons and conversion of photons into products, and S is the total incident solar irradiance (mW cm^{-2}) [17, 18, 24]. The photon flux is the area below the spectrum curve (number of photons vs. photon energy) for the photons available for conversion; and it is directly proportional to solar conversion efficiency (eq 2.1). The materials with larger band-gaps have smaller absorbed photon flux (Fig 2.2) and, in turn, lower conversion efficiencies. The maximum attainable solar conversion efficiency of a single band-gap solar cell, dictated is limited by the Shockley-Queisser limit ~33% at AM1.5G illumination, where the optimum band-gap for a single junction photovoltaic device is around 1.4 eV [36].

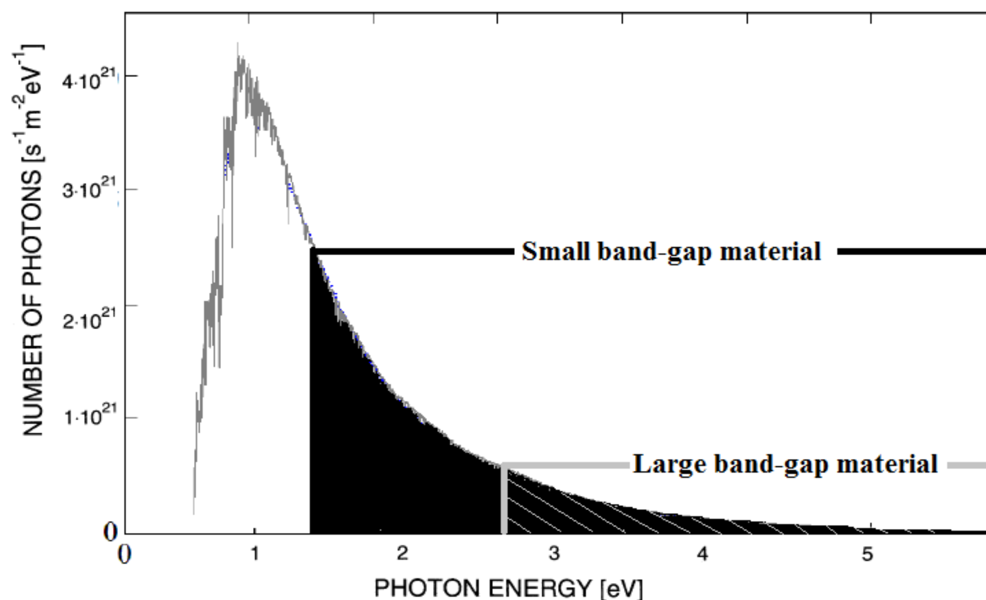

Figure 2.2: The solar energy spectrum under AM1.5G irradiance (where angle between the overhead and actual position of the sun is 48°). The materials with a smaller band-gap absorb a larger fraction of the solar energy than those with a larger band-gap, resulting in a higher solar conversion efficiency [32, 37]. Adapted with permission from [37]. Copyright (2012) Optics express.

Hence, utilizing a single band-gap device for water splitting will be inefficient because materials with $E_g > 2$ eV would have to be used, reducing the maximum theoretical efficiency by more than 33% since a part of the spectrum, where there is considerable solar photon flux, is left out from conversion [38-40].

In order to convert the solar energy, a dual band-gap photoelectrolysis cell configuration (dual photosystems) would provide the ability to utilize various combinations of different band-gap semiconductor materials. These materials will have wider combined range of light absorption, providing more efficient water splitting devices with a higher obtainable photovoltage (Fig 2.3) [32, 34, 41]. Considerable higher efficiencies can be achieved using these multijunction devices, although the quantum

yield is reduced by a factor of two because two photons are required to produce one molecule of H_2. A back-to-back wireless design for dual photosystems is proposed by Nozik in which two absorbers with different band-gaps are stacked in tandem (Fig 2.3) [42]. Light with high energy is absorbed with a higher band-gap material and the low energy light, which can be passed on to the second absorber, is absorbed by the lower band-gap material [17, 24, 32, 33]. Dual photoelectrolysis cell configurations also allow partitioning redox reactions between two photoanode/liquid (OER) and photocathode/liquid (HER) interfaces and obtaining a higher photovoltage (Fig 2.3).

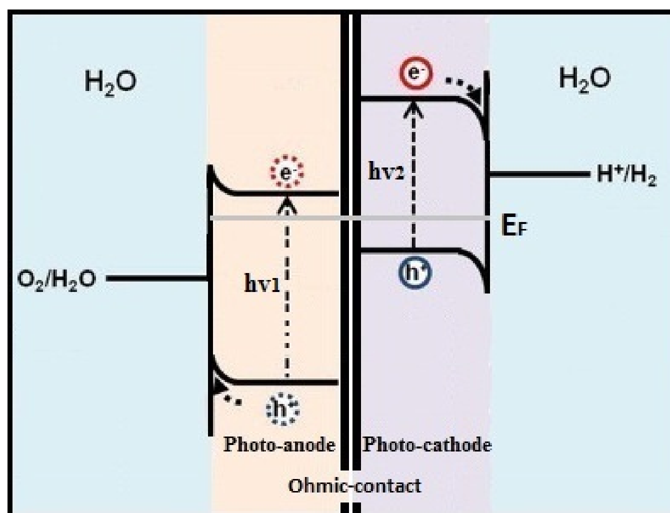

Figure 2.3: Energy diagrams for a dual band-gap water splitting system with photo-anode and photo-cathode photoelectrodes electrically connected in series.

Placement of the valence-band and conduction-band edge positions of a semiconductor photoelectrode relative to the potentials for the oxygen and hydrogen evolution reactions is another important factor in the operation of this kind of photo-electrochemical cells (PEC). The conduction band and valence band energy levels at the

semiconductor/solution interface must straddle the levels of energy corresponding to the hydrogen and oxygen evolution reaction, respectively [24]. A proposed configuration of an artificial photosynthesis device is a dual band-gap photosystem including an n-type and a p-type semiconductor, in series. Semiconductors with more positive valence bands compared to the OER's electrochemical potentials (E^o= 1.23 V) are well suited to drive OER. Semiconductors having a sufficiently negative conduction band compared to HER's electrochemical potentials (E^o= 0.0 V), are ideal to drive HER. Some of the large band-gap n-type and p-type semiconductors bracket the levels of energy corresponding to redox couple reactions (Fig 2.3) [24].

Dual band-gap water splitting systems require two photons (average of 1.23 eV per photon) or four photons (average of 0.615 eV per photons) to produce one molecule of H_2 [17, 18], the maximum efficiency of 41% is calculated for a dual band-gap photo system under AM1.5G irradiance (λ_1=2,610nm and λ_2=910nm) by Bolton [17].

2.1.1 Bulk electrical properties of Solar cells

The minority-carrier lifetime, τ , is a very important property of crystalline Si for photovoltaic applications. It is the average time it takes for a minority carrier to recombine; and it is inversely proportional to the trap density, $\tau = \frac{1}{\sigma N v_{th}}$, where σ is the cross section for electron capture, *N* is the density of taps or recombination centers, and v_{th} is the thermal velocity. This characteristic length is the minority carrier diffusion length defined by $L_D = \sqrt{D\tau}$ [43, 44], where D is the minority carrier diffusion coefficient. L_D determines how far photogenerated carriers can diffuse before recombination (30-100 μm for multicrystalline wafer silicon [45]) and is used to judge

material quality in photovoltaic applications. L_D strongly depends on the type and magnitude of recombination processes in the semiconductors. The recombination rate strongly depends on the number of defects present in the material, so the method used to fabricate the semiconductor wafer and the processing also have a major impact on defects density and, in turn, the diffusion length [43, 46]. Two important characteristics of solar cells, short circuit current (J_{sc}) and open circuit voltage (V_{oc}) that are strongly dependent on L_D. J_{sc} and V_{oc} are used to determine solar cells efficiency, $\eta = \frac{I_{sc} \times V_{oc} \times FF}{P_{in}}$, where $P_{in}$is total optical power in and FF is the ratio of maximum obtainable power to the product of the open-circuit voltage and short-circuit current. In the case of PECs, J_{sc} can be considered a measure of the number of light-generated carriers that are swept across a call per unit time. J_{sc} reduces as L_D decreases because photo-generated carriers are not able to reach water/photoelectrode junction and be collected without recombining. J_{sc} is expected to decrease from ~0.04 to ~0.0003 Acm^{-2} if L_D decreases from 125 μm to 1μm for a typical planar photoelectrode [43].

In the case of photochemical cells, V_{oc} is the photogenerated voltage cross a cell, which is required for water splitting. Considering the p-n junction of a PEC cell as an ideal diode in parallel with a pure light-generated current source leads to

$$V_{oc} = \frac{k_B T}{q} \ln\left(\frac{J_{sc}}{J_o}\right), \quad (2.2)$$

where q is the electronic charge, k_B is Boltzmann's constant, T is the temperature and J_o is the saturation current. When L_D reduces, carriers move to the recombination source very quickly and recombine, dramatically increasing the saturation current, $J_o \propto \frac{1}{L_D}$, and

reducing V_{oc}. V_{oc} is expected to decrease from ~0.7 V to ~0.58 V if L_D decreases from 125 μm to 1μm for a typical planar photoelectrode [43].

2.1.2 Photoelectrode Materials

The earliest work on photoelectrode materials was reported by Fujishima and Honda in 1972 on a water splitting cell made of TiO_2 photoanode and a Pt cathode [10]. TiO_2 is chemically stable, nontoxic, and a relatively inexpensive photocathode; however, utilization of TiO_2 (E_g~ 3 eV) is challenging since these materials hardly absorb visible light but UV radiations [25,41,42]. The application of Pt as a photocathode is also doubtful because of the limited amount of this metal on our planet and its high cost [47]. Later on, many studies have been reported on different types of photoelectrode materials. Photocathodes made of p-GaP have been reported in combination with n-Fe_2O_3 with efficiency of 0.1% [48]; however, the p-GaP electrode is not stable under illumination due to the photocorrosion [49, 50]; and the n-Fe_2O_3 electrode shows a poor electrical performance due to unfavorable surface properties. A dual band-gap structure comprising p-InP and n-GaAs has shown conversion efficiencies of 7–12% [51]; however, the n-GaAs electrodes cost too much for large-scale terrestrial application due to expensive fabrication techniques to passivate grain-boundary (the source of photocarrier traps) generated by arsenic in the structure of n-GaAs [51, 52]. The p-InP electrodes well absorb visible and the near-infrared spectrum, but E_v of p-InP lies above the O_2/H_2O level and its surface-oxide is a poor electrocatalyst for hydrogen evolution [53-56]. In another configurations, oxide semiconductors NiO and ZnO were used [57]. However, photoelectrochemical instability and the low ratio of photo-generated carriers to trapped

holes (high carrier recombination) [54, 58] as well as the low absorption of visible light of ZnO (E_g ~3.2 eV) had made these structures to be infeasible [55]. Photoelectrochemical cells incorporating n-CdSe have also been reported in combination with p-CdTe (conversion efficiencies of 6–10%)[59], but extreme susceptibility of n-CdS and p-CdTe in aqueous electrolytes limit the viability of these combinations [55, 56].

A silicon photoelectrode with a small band-gap of 1.12 eV and a high photocurrent generation ability, resulting a high conversion efficiency ~ 30% (a single p-n junction), is a desirable light absorber to use in dual band-gap water splitting cells [24, 34, 36]. Silicon is also prevalent in the electronics and PV industries. It is important to note that silicon is extremely susceptible to oxidation from being handled in air and there is a high interface trap density, N, at silicon-silicon oxide interfaces. The large surface trap and recombination density naturally reduces the minority-carrier lifetime, decreasing L_D; for instance, the large surface recombination centers reported for micro-, nano-crystalline thin films (due to the large surface-to-volume ratio) reduces L_D to 0.5-2 μm, while L_D is 30-100 μm for multicrystalline wafer silicon [45]. The small L_D resulting from the large density of recombination centers effectively impacts silicon performance as a photovoltaic cell by reducing V_{oc} and J_{sc}. This issue has led to a variety of attempts to stabilize silicon, and garnered tremendous interest in photovoltaic applications owing to the favourable band-gap and its natural earth abundance [60, 61]. Stabilization of silicon is especially critical for Si photocathodes and photoanodes to function properly because silicon-oxide layer not only changes electrical properties (J_{sc} and V_{co}), it generates a large potential barrier that blocks carrier collection at photoelectrode/solution junction.

Oxidation occurs on exposed surfaces of silicon; therefore, surface passivation (functionalization), which reduces the activity of the exposed surface, increases its ability to resist chemical degradation of the surface. There has been considerable interest in methods of silicon surface passivation to protect against oxidation by air or water and to prevent charge-carrier recombination.

2.1.3 Surface Functionalization of Silicon

The Si microwires used for characterization in this thesis were functionalized with methyl-group by collaborators in the Lewis research group at California Institute of Technology (Caltech). The technique used by collaborator to passivate the Si microwires surfaces with methyl-group for this study will be described in this section.

For the purposes of this section, the surface recombination velocity, S, is treated as a parameter to specify the recombination at a surface. In a surface with no recombination, the movement of carriers towards the surface is zero, and hence the surface recombination velocity is zero. In a surface with infinitely fast recombination, the movement of carriers towards this surface is limited by the maximum velocity they can attain, and for most semiconductors is on the order of $S{\sim}10^7$ cm/sec or larger [62-64]. There has been considerable interest on different chemical functionalization processes to prevent extensive oxidation of the Si surface while maintaining the surface recombination velocity as low as the H-terminated silicon surface. One strategy is the formation of surface Si-C bonds [65, 66]. Alkylation of H-terminated Si using alkylmagnesium reagents [67, 68]; radical halogenations [69]; chemical free-radical activation [69, 70]; irradiation with ultraviolet light [71, 72]; thermal activation [73, 74]; and hydrosilylation

[75, 76] have been reported for both the crystalline and porous Si (100) and Si (111) surfaces [74, 77]. Enhanced oxidative stability and a low surface recombination velocity for some of these surfaces have been reported. Our collaborators functionalized the Si microwires used in this study with methyl-group as this approach has been reported to improve oxidation resistance and surface recombination velocity (S~460 cm/sec for a planar device) [62, 78, 79].

The methyl-terminated Si surfaces were obtained through the following two steps: (i) a wet-chemistry-based chlorination procedure, and (ii) an alkylation procedure (Fig 2.4) [65, 78]. First, the samples were etched in NH_4F (aq), resulting in H-terminated Si surfaces [65, 78]. Then, the H-terminated Si samples were chlorinated by PCl_5 in chlorobenzene. Following the chlorination, the samples were methylated using CH_3MgX (X = Cl, Br) [65, 78, 79].

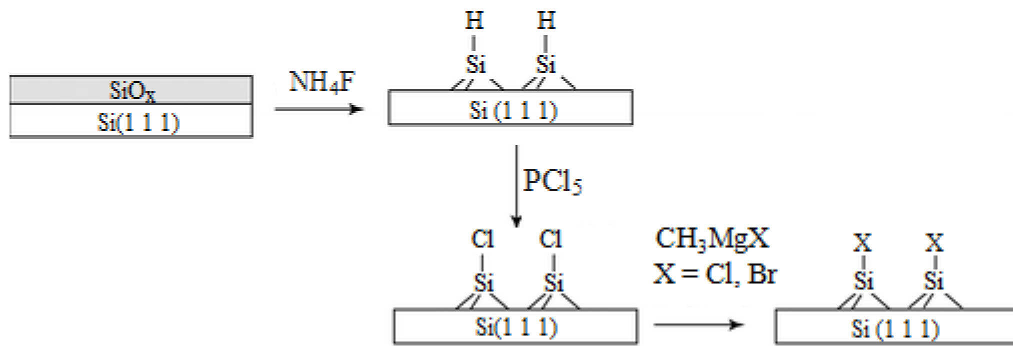

Figure 2.4: Functionalization of Si(111) surfaces by introducing methyl groups on the surface.

2.1.4 Nano- and Micro-photoelectrodes

Earlier work on PEC cells was mainly based on planar photoelectrodes (Fig 2.5) [9, 10, 31, 80]. The minority carrier length, L_D, of such a PEC should be greater than $1/\alpha$, where

α is the absorption coefficient of the semiconductor near the band-gap energy to have the maximum collection of photo-generated carriers [24]. These devices should be made of high purity semiconductors with lowest possible defect concentrations to reduce the number of recombination sites.

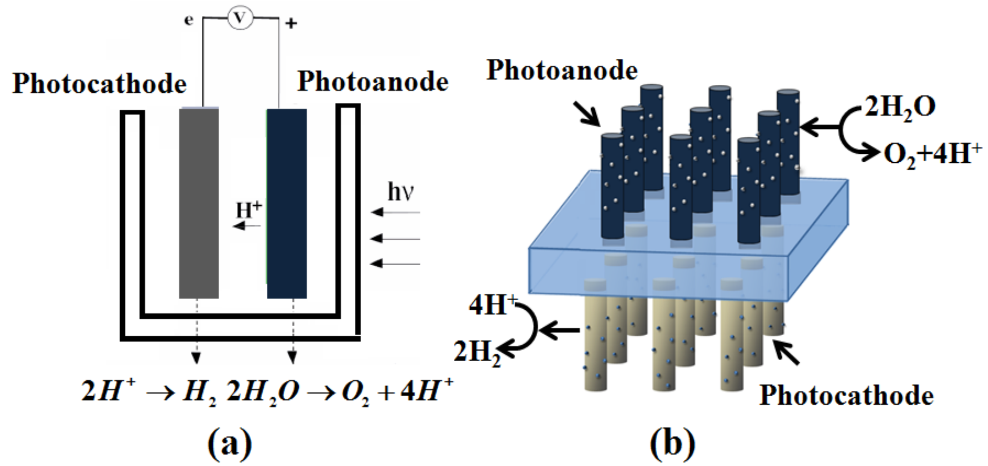

Figure 2. 5: Schematic of a PEC device (a) based on planar photoelectrodes and (b) based on nano- and micro photoelectrodes.

The small sizes of micro and nano-wires reduce the distance for photo-generated holes and electrons to reach the photoelectrode/electrolyte interface for water splitting, and hence enable near-unity collection efficiencies despite short minority carrier diffusion lengths (0.5-2 μm) for micro and nano-wires (Fig 2.6) [24, 43].

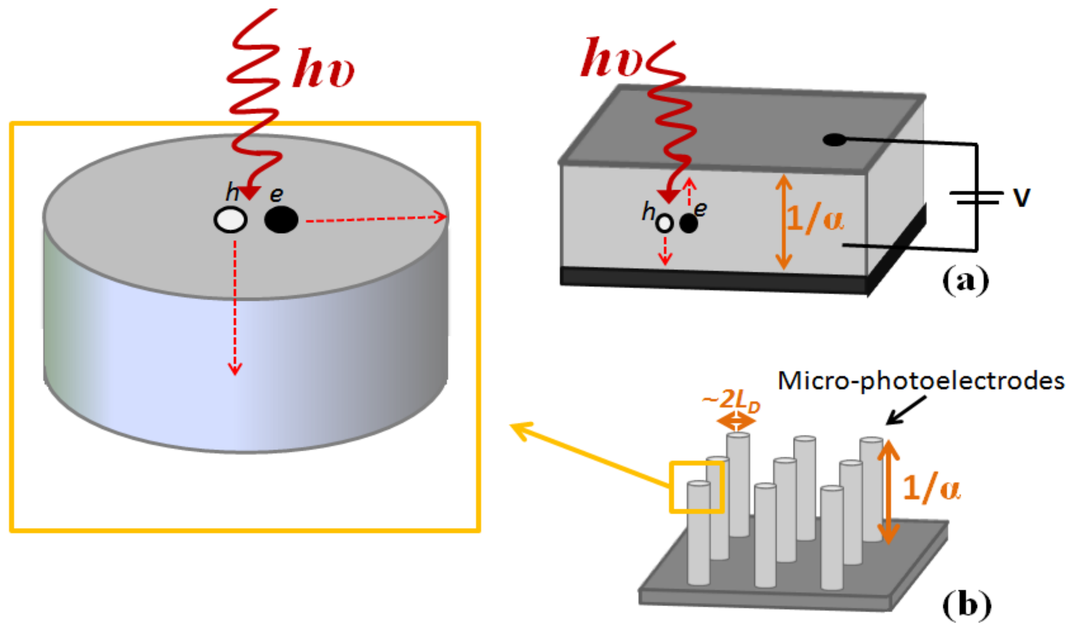

Figure 2.6: Photogenerated carriers (white and black circles) in a planar system (a) travel the entire thickness of the device, ~1/α, before collection, while in a microwire array assembly (b) with appropriate dimensions, carriers reach the microwire surface before recombination.

Employing micro- or nano- wire arrays also increases the absorption of light by improving the trapping and scattering of light. In comparison to the conventional planar PEC electrode, these structures can reduce the energy loss due to light reflection as the coating of micro- or nano- wires on conducting substrates naturally forms an antireflection layer [81].

Micro- or nano- wire array performance depends on the geometry of wires. It has been demonstrated that the photogenerated voltage, V_{oc}, reduces by increasing the junction area of the semiconductor photoelectrode (solution-semiconductor contact). This behavior is expected from the dependence of V_{oc} on the photogenerated current, J_{sc} and the saturation current, J_o (eq 2.2). The decreased V_{oc} (> 60 mV per order of magnitude increase in the junction area) results from the increased junction area which dilutes the

photogenerated charge carriers, yielding the reduced J_{sc} [82]. Distribution of the photogenerated charge carriers over a larger junction area yields a reduction in splitting of the quasi-Fermi levels (shifted Fermi energy levels because the populations of electrons and holes are displaced from equilibrium) at the solution-semiconductor interface.

J_{sc} can be considered as the number of light-generated carriers that are swept across the photoelectrodes. J_{sc} is therefore expected to increase as the thickness increases, yielding the more available area for light absorption and carrier generation, until the thickness becomes much larger than L_D, This factors highlight the junction area (thickness) should be enhanced to collect all the carriers generated by light, while ensuring that the junction area is as small as possible to avoid unwanted decrease in the V_{oc} (i.e. radius of the rods ~ L_D) [82].

J_{sc} is also expected to increase as the length of the rods increases, until some limiting value, when it becomes much larger than the optical thickness of the material. J_{sc} remains constant when the length of the rod becomes much longer than the optical thickness. Therefore, the silicon rods must be up to 125 μm (~1/α) long to absorb 90% of the incident light at wavelengths from 700 to 1100 nm [43, 81, 83].

2.1.5 Crystalline Silicon Microwire Array Growth

There are two basic approaches to synthesizing microwires: top-down and bottom-up. Top-down approaches such as electron beam lithography and deep-UV photo lithography are well established techniques (CMOS technology) for nano-patterning, contact formation and doping [84, 85]. There are also different methods to synthesize large-scale

rods array using the bottom-up approach such as Oxygen-Assisted-Growth (OAG) [86], Vapor-Solid-Solid (VSS) [87], Laser-Assisted Catalytic growth (LAC) [88], Vapor-Liquid-Solid (VLS) [44, 89].

The Si microwires used for electrical characterization in this thesis were grown by collaborators in the Lewis group at California Institute of Technology (Caltech) using The Vapor-Liquid-Solid (VLS) technique. In the VLS technique, the lithographically patterned gold on a silicon substrate catalyzes the growth of silicon rods or whiskers in chemical-vapor-deposition (CVD) conditions from the reaction of $SiCl_4$ and H_2 vapor phases (Fig 2.7). Mixing Au with Si greatly reduces the melting temperature of the alloy to (~363 °C) as compared to the alloy constituents. Au particles can form Au-Si eutectic droplets at temperatures above ~363 °C and adsorb Si from the vapor state ($SiCl_4$) until reaching a supersaturated state of Si in Au. Gaseous substances ($SiCl_4$ and H_2) react at the gold droplet surfaces and produce Si and HCl (volatile by-product) and Si diffuses into gold droplets. The supersaturation of droplets leads to axial crystalline silicon upon the substrate. The gold-catalyst droplets rise elevator-like from the substrate to the tips of the growing wires [89].

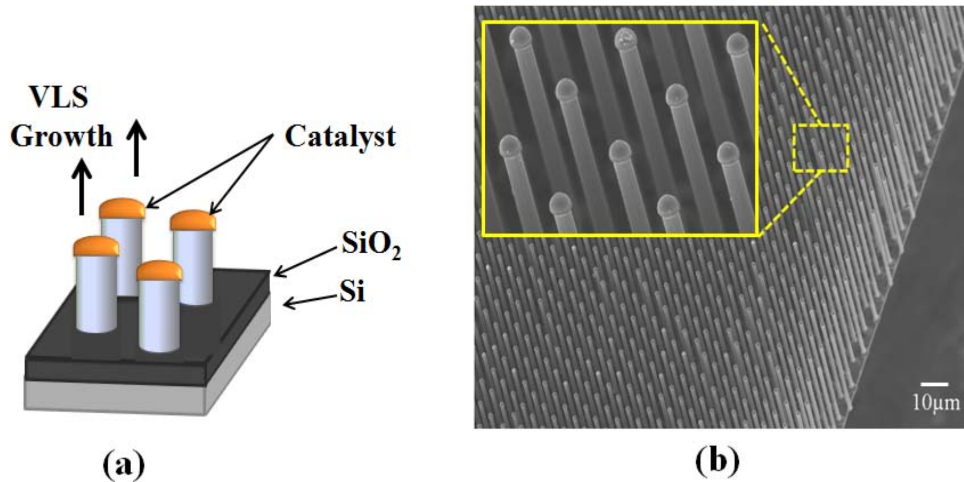

Figure 2.7: a) Schematic diagram of VLS-growth of Si microwire arrays [90], b) SEM images of a microwire array taken by 10 kV-500X (the magnified image on the left is taken by 10 kV-2500X).

This growth mechanism can produce highly anisotropic nano- and micro-rods (up to the cm scale) arrays with a well-defined orientation because the substrate influences the orientation and low defect density because the liquid alloy protects the growing crystal from foreign particles [89, 91]. This technique also produces rods with high growth rates (up to several μm/s) and at a low deposition temperature because the growth occurs at the liquid-solid transformation [92]. The diameter of the crystal can be well-controlled by the initial amount of catalysts used for alloying and the deposition temperature [91-94]. The length can be controlled by ceasing the growth when the temperature reduces or the gaseous substances (supply) stops [93].

In the case of Si, contrary to the previous works which had favored the use of Au catalyst, a variety of other metals such as Cu, Bi, Cd, Co, Fe and Al have also been used to catalyze the growth process [95, 96]. Different gaseous substances such as $SiCl_4$ (at ~ 1000°C), SiH_4 and Si_2H_6 (at ~500°C) have been reported to be used in VLS growth technique [97]. The collaborators used Cu and Au as catalysts and $SiCl_4$ as a gaseous

substance to grow microwires. The basic procedure followed by them to grow Si microwires was the same; but the flow rates and temperatures varied from system to system. The basic procedure for VLS growth of Si microwires is the same, and the flow rates and temperatures vary from system to system. In the beginning, SiO_2 is grown thermally on Si wafers and then positive photoresist is deposited on the oxide layer. The photoresist is patterned using standard photolithographic methods to produce an array of holes in photoresist. The oxide layer exposed through the holes is etched to expose the underlying Si substrate using HF. Then, catalyst is thermally evaporated onto the substrate and the photoresist is removed [98, 99]. Si microwires were then grown by annealing the samples in a H_2 atmosphere at 1000 °C for 20-25 min, followed by exposure to flowing $SiCl_4$ saturated in He or H_2 (ratio of 50:0.5-2:500), and BCl_3 or PH_3 (~0.25% in H_2). When the time for microwire growth elapsed, the samples were cooled to 600°C under H_2, and then cooled to room temperature under N_2 or He at ambient pressure [98-100].

2.2 Candidate Membrane Systems

An artificial photosynthesis device is a light-collecting device, which uses solar energy to split water molecules into H_2 and O_2. Hydrogen would be stored as a form of chemical fuel and the O_2 would be vented to the atmosphere [24, 101]. Two microstructure semiconductor photoelectrodes in series embedded in a supporting membrane is a practical approach to split water into its components using sunlight (Fig 2.8) [17, 33, 101].

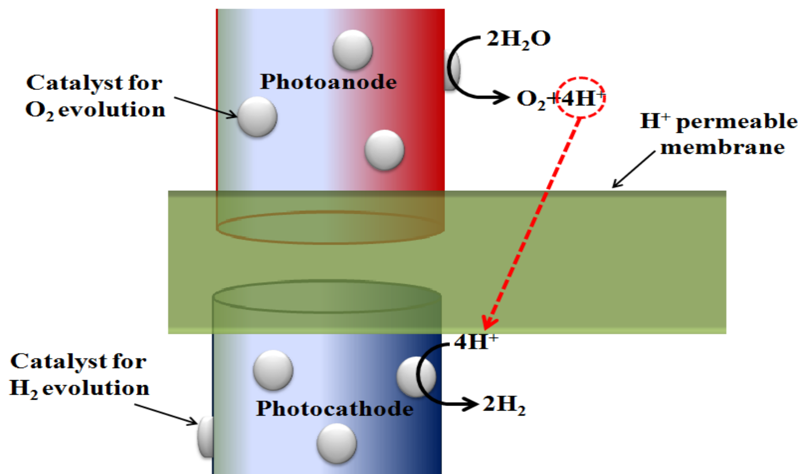

Figure 2.8: Schematic diagram of the proposed artificial photosynthesis system. The components are: light harvesting electrodes (one absorber acting as a photocathode and the other as a photoanode); a membrane barrier for separating the products of the oxidation and reduction reactions in two chambers; and redox catalysts.

The membrane must be (i) effectively adhesive to a wide range of semiconductors, mechanically stable, water insoluble and homogeneous to provide enough mechanical support; (ii) electrically conducting ($\sigma > 0.2$ mS cm^{-1} per micron of membrane thickness) to prevent any need for any external electrical wiring connections to keep overall charge neutrality of system when the protons and electrons are generated in oxidation and reduction chambers; (iii) impermeable to gases to effectively separate the gaseous products because H_2 and O_2 generated respectively from redox process to recombine and produce water; (iv) ionically conducting ($\sigma > 0.2$ mS cm^{-1} per micron of membrane thickness [25]) to transfer ions of H^+ produced from oxygen evolution reaction (OER) to other chamber to be use in the hydrogen evolution reaction (HER) and generate hydrogen fuels; (v) optically transparent, allowing light to be effectively absorbed by both microstructure electrodes assemblies [25, 102] ; and (vi) stable in the presence of various

pH conditions because cation H^+ and anion $(OH)^-$ generated respectively produce acidic media at the oxygen evolution reaction chamber and alkaline media at hydrogen evolution reaction.

In principle, there is no single material that able to satisfy all the mentioned requirements. Poly (3,4-ethylenedioxythiophene) or PEDOT is a conducting polymer carrying positive charges; its structure is based on 3,4-ethyleneqdioxylthiophene or EDOT monomer (Fig 2.9). PEDOT exhibits optical transparency in thin structures and a very high stability in the oxidized state. In addition, it also shows a conductivity between 1-300 S/cm with moderate band-gap (E_g = 1.6 ~ 1.7 eV) and a very low redox potential [103-105]. However, PEDOT was initially found to be poor in ionic conductivity (orders of magnitude lower than their electronic conductivity,) and water insoluble polymer, which cannot form a homogeneous solution of the solute in water. It is not possible to easily form a homogeneous, crack, and pinhole free membrane for those artificial photosynthesis system applications.

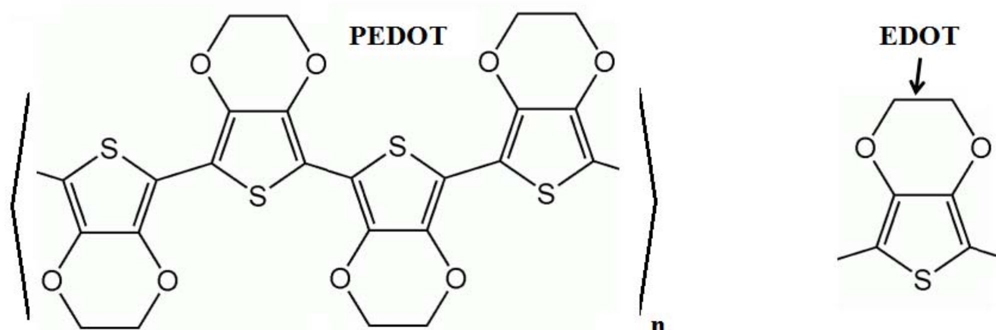

Figure 2.9: Chemical structure of Poly (EDOT) based on 3,4-ethylenedioxylthiophene or EDOT monomer.

Those problems can be circumvented by mixing PEDOT with a water-soluble polyelectrolyte, known as PSS poly (styrene sulfonicacid). The combination of PEDOT and PSS yields PEDOT:PSS composite membrane (Fig 2.10) with a very high electronic conductivity > 10 Scm^{-1} and ionic conductivity of ~8.1$mScm^{-1}$ [25, 106-108] as the

sulfonyl groups are deprotonated and carry a negative charge in the composite. PEDOT solubility increases by 30% in the presence of PSS [109]. PEDOT:PSS are sufficiently soluble to allow spin-coating and forming a homogenous and continuous films.

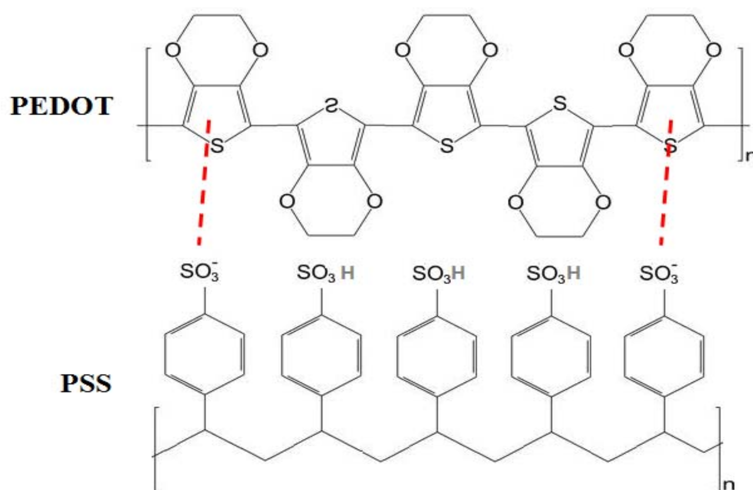

Figure 2.10: Chemical structure of conducting polymer PEDOT PSS.

Water based PEDOT:PSS inks are commercially available and they show good film forming properties. Its good film forming properties allow to obtain a continuous, homogeneous, crack, and pinhole free layer of PEDOT:PSS on the micron scale with long term stability by spin coating and driving out the water by heat.

Optimization of the material parameters for membrane will gain desirable efficiencies in the final device. This is especially important for electrical junctions between the photoelectrode microwires and the candidate membrane.

2.3 The Polymer/microwire Systems: Requirements

The solar water-splitting devices focused in this thesis comprise of two junctions in series, n-Si microwire/PEDOT:PSS and p-Si microwire/PEDOT:PSS [26, 29, 101, 110].

Absorption of photons with energy greater than the band-gap of the microwires and normally incident on a 7 μm pitch array have been estimated to result in a maximum short-circuit photocurrent of ~21 nA per microware [26, 27]. The source of electrical loss must be minimized to effectively use the available photocurrent generated by the system to split water with reasonable efficiency. To minimize the electrical losses in such a system, voltage drops of <10 mV yield losses that were 1% of total photogenerated voltage required for water splitting. Considering 21 nA flowing through the microwire–polymer system, the acceptable resistance to have voltage drops of < 10 mV in the junction to the polymer film is < 0.5 MΩ [27]. However, the required energy of 1.6-2.4 eV is frequently reported [24] for such a device to efficiently function in which 1.23 eV is used for water electrolysis reaction and 0.37-1.17 eV to cover the losses, yielding the minimum junction resistance of ~17 MΩ to 21nA photo-current in the system. In this thesis the worse situation was assumed in which 1.23 eV energy was available for electrolysis of water and 1% of this energy was allowed for losses; thus the total resistance was needed to be <0.5 MΩ [27]. Functionalization of Si microwires with methyl groups (CH_3) produces long-term electrical and chemical stability, with negligible native oxide growth over time [62, 66, 78]. Previous studies showed an acceptable junction resistance ~ 0.1 MΩ for the junctions between a conducting polymer and methyl-terminated p-Si microwires [26, 27]. However, the junction between methyl-terminated n-Si microwires and the conducting polymer showed a larger resistance > 20 MΩ far above the minimum requirements [27, 78, 111]. The large junction resistance resulted from the formation of a Schottky barrier at the junction between the methyl-terminated n-Si microwires and the membrane [27, 29].

Modification of n-Si microwires in contact with the membrane is expected to improve the electrical properties of the n-Si/PEDOT:PSS junction [27]. Two possible approaches to modify n-Si microwires can be raising the doping concentration of n-Si to lower the depletion region and facilitate quantum mechanical tunnelling of the charge carriers or by addition of a metallic interfacial layer to reduce the Schottky barrier height at the contact with semiconductor and make Ohmic contact with conducting polymer.

2.4 PEDOT:PSS/silicon Assembly

The mechanism of electron tunneling through the Schottky barriers is described in the next few pages to explain that raising the doping density in n-Si microwires embedded in PEDOT:PSS will potentially improve the electrical behavior of the junctions. When a conducting polymer is electrically connected to a semiconductor, electrons traverse the junction from higher energies to lower energies until Fermi energy of both polymer and semiconductor align and equilibrium is established. The Fermi energy in semiconductor materials depends on the doping density of carriers and the temperature, calculating from eq 2.3[30]:

$$E_f - E_i = (+/-)k_B T ln(\frac{n/p}{n_i}), \tag{2.3}$$

Where E_f is Fermi energy, is E_i the intrinsic energy (~ 4.6 eV), n is electron density, p is hole density, and n_i is intrinsic carrier concentration (~ 1.45×10^{10} cm^{-3} for Si at T = 300°K). The polymer in contact with the semiconductor forms a barrier at the junction, namely Schottky barrier. The barrier height ($q\phi_b$) of the junction is obtained using Schottky-Mott relationship $q\phi_b = E_g - q\phi_p + q\chi_s$ (for p-semiconductors) and $q\phi_b =$

$q\phi_p - q\chi_s$ (for n-semiconductors) [29, 30, 112, 113], where $q\phi_p$ is the work function of the conducting polymer and $q\chi_s$ is the electron affinity of the semiconductor (Fig 2.11).

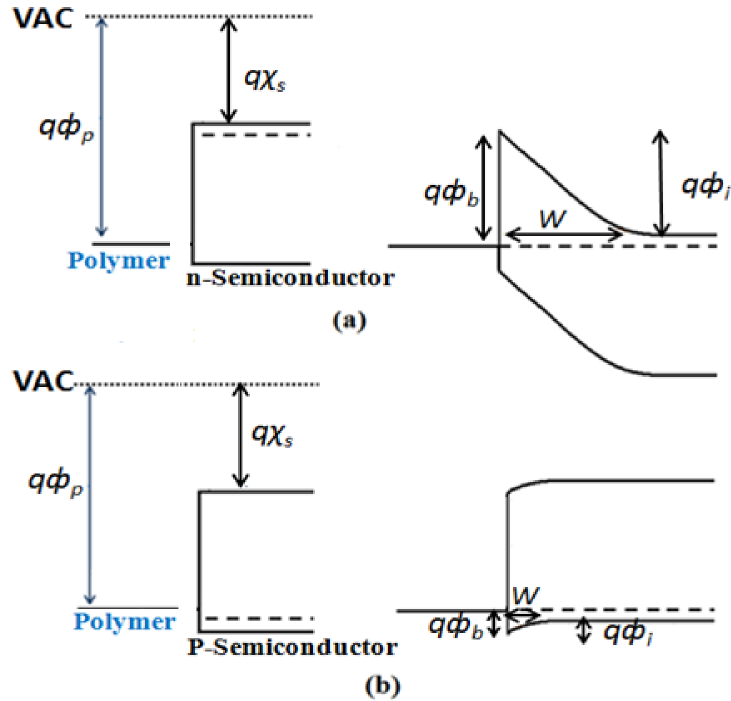

Figure 2.11: Energy band diagram of a conducting polymer junction with (a) n-semiconductors in contact before (left) and after establishment of electrochemical equilibrium (right) and (b) p-semiconductors in contact before (left) and after establishment of electrochemical equilibrium (right).

The polymers with a large work function normally make Ohmic contacts to the p-semiconductors with small barrier heights and rectifying junctions to n-semiconductors with large barrier heights. The region in the semiconductors close to the junction, which is depleted of mobile carriers, is the depletion region. The depletion layer width, W is obtained from eq 2.4 [30]:

$$W = \sqrt{\frac{2\varepsilon_s(\phi_i - V)}{qn}}, \tag{2.4}$$

where ϕ_i is the built-in potential (Fig 2.11), n is the majority carriers concentration of semiconductors and ε_s is the permittivity of the semiconductors. The built-in potential is obtained from $\phi_i = q\phi_b - \frac{E_C - E_F}{2}$ for n-type semiconductors [30].

Once a Schottky barrier forms, there are three distinctly different transport mechanisms for an electron to overcome the potential barrier [29, 114]: (i) thermionic emission (TE) over the barrier, (ii) field emission (FE) near the Fermi level, and (iii) thermionic-field emission (TFE) at an energy between TE and FE (Fig 2.12) [29, 30].

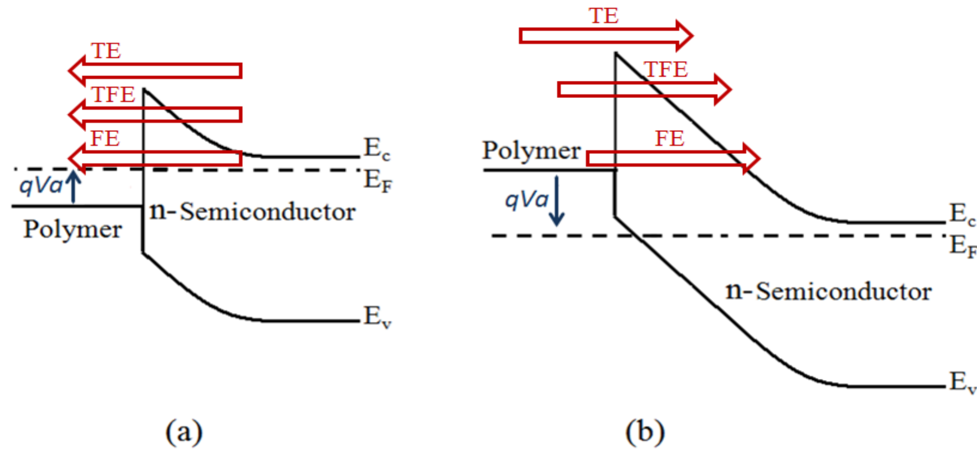

Figure 2.12: Energy-band diagrams showing transport mechanisms in a Schottky diode (on n-type degenerate semiconductor) under (a) forward bias and (b) reverse bias. TE = thermionic emission. TFE = thermionic-field emission. FE = field emission [30].

If the quantity of electrons arriving at the barrier through drift and diffusion mechanisms exceeds the number of electrons traversing over the barrier, thermionic emission dominates. It requires a large depletion layer compared to the mean free path and normally this condition is satisfied in the forward bias [30, 115]. When a forward bias voltage is applied to a Schottky contact (to the polymer or metal), the electrons on

the semiconductor side of the interface increase by the factor of $\exp(\frac{qV_a}{nk_BT})$, where V_a is the voltage across the junction, n is the ideality factor (typically varies from 1 to 2). So, there are more electrons with energy larger than the top of the barrier, yielding an extra current flow from the semiconductor through the junction [30, 116-119]. In reverse bias, FE and TFE are dominant in which carriers with energies lower than the barrier height are able to traverse across the barrier using the quantum mechanical tunneling mechanism. FE is a pure tunneling process; and TFE is tunneling of thermally excited carriers.

Basically, carriers can tunnel through a potential barrier if the width of the depletion region is narrow enough. In relatively highly doped semiconductors, the depletion region becomes so narrow (especially near the top) that electrons can tunnel through the barrier (Fig 2.13).

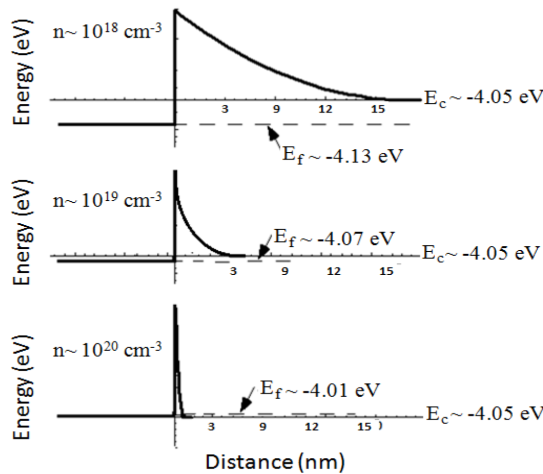

Figure 2.13: The depletion widths of Schottky junctions for n- Si with n ~ 10^{18} cm^{-3}, n ~ 10^{19} cm^{-3} and n ~ 10^{20} cm^{-3}. The width of the depletion layer calculated using eq 2.4. The relative permittivity of silicon was ε_s=11.7 and the barrier height was assumed to be $q\phi_b$=1.1eV. The Fermi energy levels for different doping density obtained from eq 2.3. The intrinsic carrier concentration was n_i~ 1.45×10^{10} cm^{-3}; the thermal energy was k_BT=0.0256 eV ; and the intrinsic energy was E_i~ 4.6 eV.

In general, the tunneling current J through the Schottky barrier is generally obtained by (eq 2.5):

$$J = qnv_R\Theta, \tag{2.5}$$

where v_R is the Richardson velocity, the average velocity of the carriers approaching the barrier, n is the carrier density of available electrons and Θ is the tunneling probability of electrons. The tunneling probability, Θ is given by (eq 2.6):

$$\Theta = \exp\left(\frac{-4}{3}\frac{\sqrt{2qm^*}}{\hbar}\frac{\phi_b{}^{3/2}}{E}\right), \tag{2.6}$$

where ϕ_b is the barrier height of the Schottky junction and E is the electric field across the Schottky barrier. The possibility of the electrons tunnelling through the barrier increases exponentially with the decrease in the barrier heights and the barrier width because the electrical field is inversely proportional to the barrier width. When the doping increases, the barrier becomes thinner and the number of electrons available for tunneling also increases. Hence, the electrons can tunnel through the barrier and the tunneling current is dominant at the doping density greater than 10^{18}-10^{19} cm^{-3} [30].

TFE dominates for doping density less than 10^{20}-10^{21} cm^{-3} and FE dominates for the doping density more than 10^{20}-10^{21} cm^{-3} because TFE is tunneling of thermally excited carriers which see a thinner barrier than FE (Fig 2.13) [30].

In TFE regime, current, J and contact resistance, R_J, are given by

$$J = \frac{A^{**}T}{k_B}\sqrt{\pi E_{00}q\left[V_a + \frac{\phi_b}{Cosh^2\left(\frac{E_{00}}{k_BT}\right)}\right]}\exp\left(-\frac{q\phi_b}{E_{00}}\right)\exp\left(\frac{qV_a}{\acute{\varepsilon}}\right), \tag{2.7}$$

$$R_J = \frac{k_B\sqrt{E_{00}}Cosh\left(\frac{E_{00}}{k_BT}\right)Coth(\frac{E_{00}}{k_BT})}{A^{**}\,Tq\sqrt{q\pi(\phi_b-\phi_i)}}\exp\left(\frac{q(\phi_b-\phi_i)}{E_{00}Coth\left(\frac{E_{00}}{k_BT}\right)}+\frac{q\phi_i}{k_BT}\right), \quad (2.8)$$

where

$$E_{00} \equiv \frac{q\hbar}{2}\sqrt{\frac{n}{m^*\varepsilon_s}}, \quad (2.9)$$

$$\acute{\varepsilon} = \frac{E_{00}}{\frac{E_{00}}{k_BT}+\tanh\,(E_{00})}, \quad (2.10)$$

where m^* is the effective mass, A^{**} is the effective Richardson constant. In FE regime, current, J and contact resistance, R_c, are given by

$$J = A^{**}\,(\frac{E_{00}}{k_B})^2\left[\frac{V_a+\phi_b}{\phi_b}\right]\exp\left(-\frac{2q{\phi_b}^{3/2}}{3E_{00}\sqrt{V_a+\phi_b}}\right), \quad (2.11)$$

$$R_J = \frac{k_BSin(\pi C_1k_BT)}{A^{**}\,Tq\pi}\exp\left(\frac{q\phi_b}{E_{00}}\right), \quad (2.12)$$

where

$$C_1 \equiv \frac{1}{2E_{00}}\log\,(\frac{4(\phi_b-V_a)}{-\phi_i}). \quad (2.13)$$

In the case of the solar water-splitting devices considered in this thesis, a unit cell of this structure would include two junctions in series, n-Si microwire/PEDOT:PSS and p-Si microwire/PEDOT:PSS (Fig 2.14) [26, 29, 101, 110]. Studies on the junction between Si ($q\chi_s$~ 4.05 eV) and PEDOT:PSS ($q\phi_p$~5 eV) reported a negligible barrier height, $q\phi_b$~0.15 eV for p-Si /PEDOT:PSS junction, yielding an low resistance, Ohmic contact, with an average contact resistance of 1−2 $\Omega\cdot cm^2$ over a voltage range of −1.0 to 1.0 V [29].

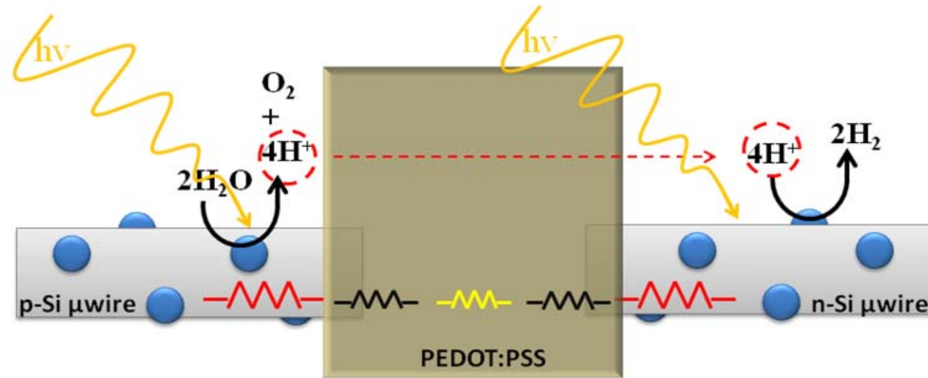

Figure 2.14: n-Si and p-Si microwire provide the photovoltage needed to evolve O_2 from H_2O and are embedded into a membrane that separate the products.

In contrast, this polymer results in a large barrier height ($q\phi_b$~0.888 eV) [29] at the junction with n-Si (n~10^{16} cm^{-3}), resulting in highly rectifying contacts for n-Si/PEDOT:PSS junction (Fig 2.15) [26, 27, 29]. Functionalization of Si surfaces with CH_3- groups (methyl-group) generates the surface dipoles, slowing down the silicon oxidation growth and yielding a more stable Si surface. However, methyl termination of silicon surface shifts the band edge energies of silicon from change in the electron affinity ($q\chi_s$) from 4.17 eV for H−Si (111) to 3.67 eV for methyl-terminated Si (111), yielding a larger potential barrier height ($q\phi_b$~ 1.01 eV) [29] at n-Si/PEDOT:PSS junction and accordingly greater rectifying behaviour compared to H-terminated n-Si. This process also yields a lower potential barrier height for p-Si/PEDOT:PSS junctions and improves the junction resistance [26, 27, 29, 110].

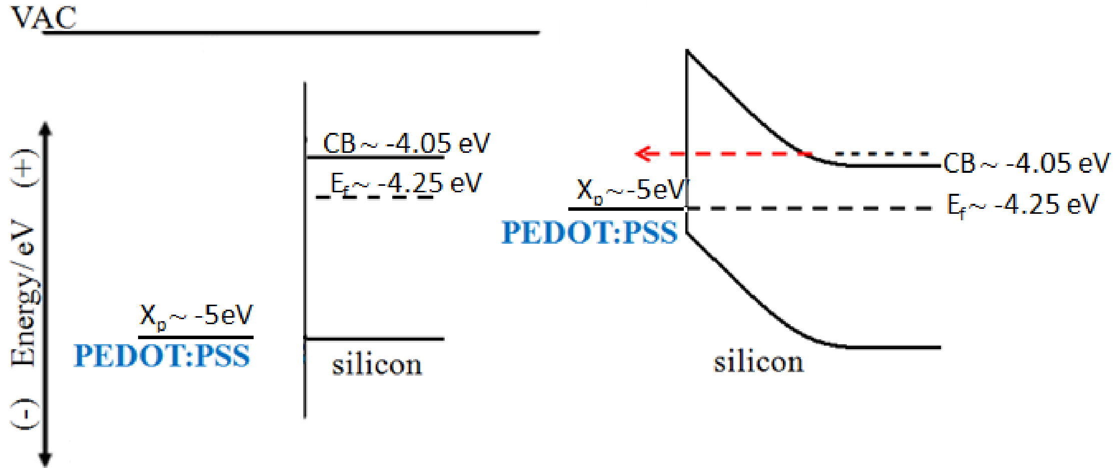

Figure 2.15: The energy level positions of Fermi levels (E_f) and conduction band (CB) of PEDOT:PSS/n-Si before and after establishment of electrochemical equilibrium; the Fermi energy levels for different doping density obtained from eq 2.3 for n-Si with $\boldsymbol{n}$~10^{16} cm^{-3}.

However, Ohmic low contact resistance (0.5−1.0 Ω·cm^2) junctions have been reported on methyl-terminated highly-doped n-type silicon electrodes (n$^+$-Si) with doping density n~ 10^{19} cm^{-3} in contact with PEDOT:PSS [29]. n$^+$-Si with doping density of ~ 10^{19} cm^{-3} forms a narrower depletion layer W~ 3 nm (eq 2.4) at the junction with PEDOT:PSS, yielding an Ohmic tunnel junctions, whereas n-Si with doping density of ~10^{16} cm^{-3} forms a wide depletion layer ~ 80 nm in contact with PEDOT:PSS (eq 2.4) yielding a rectifying junction [29].

In the same manner, the rectifying behavior and very large junction resistance of methyl-terminated n-Si in contact with PEDOT:PSS is expected to be modified by increased doping (n$^+$-Si, degenerate levels) to narrow the depletion region and facilitate quantum mechanical tunneling of charge carriers. In crystalline silicon wafers, one of the most important recombination losses occur through impurities that create energy levels within the band-gap. The effect of such recombination centers predicts that the lifetime is

a function of the doping density. Increasing the doping concentration of the semiconductor (>10^{18} cm^{-3}) from ~10^{18} cm^{-3} to ~10^{20} cm^{-3} increases the defects from ~10^{14} cm^{-3} -10^{16} cm^{-3} [120, 121] and consequently reduces carrier diffusion length from ~1 mm to 1 µm [30, 122]. In order to lower the depletion layer width to form an Ohmic tunneling junction at PEDOT:PSS/n-Si by raising the doping level and avoiding increasing recombination sites as the doping increases, it is possible to use low-doped n-Si (~10^{18} cm^{-3}) and raising doping level (10^{19} -10^{20} cm^{-3}) of Si where it is in contact with the polymer. Hence, methyl-terminated n^{+}-Si microwires with doping density of ~10^{20} cm^{-3}, and n^{+}n-Si microwires with highly-doped base ~10^{19} cm^{-3} were utilized in this thesis in order to make Ohmic tunneling junctions with PEDOT:PSS and explored the electrical behavior of the junctions.

Another common technique to improve the junction resistance of the Schottky barriers is to add a metallic interfacial layer with smaller work function, which can form Schottky barriers with smaller barrier heights. Effective reduction in the barrier heights of the Schottky diodes fabricated on the n-type semiconductor substrates using an interfacial layer have been shown in different studies [123, 124]. The effect of copper and gold interfacial layer at PEDOT:PSS/n-Si on the electrical behavior of the structure were explored in this thesis. For the purpose of this study, the n-Si microwires grown with Cu and Au catalysts were utilized; while the catalysts were kept intact on microwires, they were embedded in the polymer to form PEDOT:PSS/n-Si junction with metallic interfacial layers, PEDOT:PSS/Cu/n-Si or PEDOT:PSS/Au/n-Si.

In the case of PEDOT:PSS/Cu/n-Si, the structure include two junctions, PEDOT/Cu and Cu/n-Si junction. When a conducting polymer and a metal with their own Fermi

energy are electrically connected, such as PEDOT:PSS and Cu; electrons will move from one material to other one until the energy levels are equal, forming a well-defined Ohmic contact (with small contact resistance, R~ 0.01 μΩ/cm^2) [125].

It is important to give an introduction about silicides to describe the electric properties of Cu/n-Si and Au/n-Si junctions produced at T~ 1000 °C during fabrication process. The deposition of a metal over a silicon substrate followed by a thermal annealing at T greater than the eutectic temperature of the metal-silicon compound produces silicides (Figure 2.16) [30, 126]. Silicides are formed via interdiffusion of metals and Si atoms to a growth interface at temperatures above the eutectic temperature [126, 127]. Silicide/silicon junctions show stable electric characteristics compared to metal-silicon contacts [128]. The vast majority of the silicides exhibit metallic conductivity [126] and the silicide-silicon junction behaves as a metal semiconductor contact with smaller barrier heights, and consequently lower the contact resistances [30].

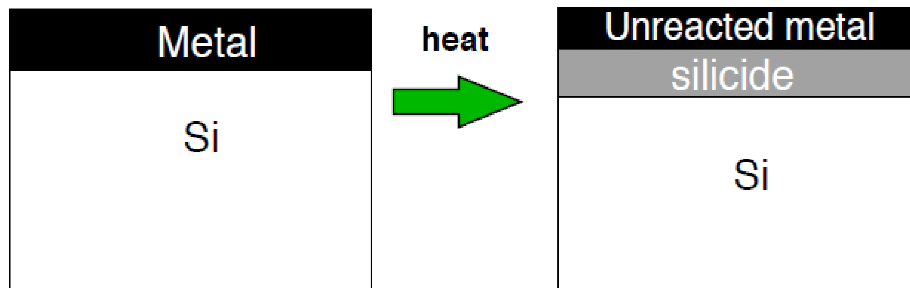

Figure 2.16: Metal deposition on Si and formation of silicide by thermal annealing.

Deposition of Cu with work function of $q\phi_{Cu}$~ 4.7 eV on n-Si forms a Schottky barrier ~0.65 eV and formation of copper silicide at T >800 °C reduces this barrier to ~0.59 eV [129, 130]. Taking Ohmic junctions of PEDOT:PSS/Cu into account, PEDOT:PSS/Cu/n-Si forms a structure with a smaller Schottky barrier ~0.59 eV compared with

PEDOT:PSS/n-Si ~1.01 eV; It results in a increase in tunneling current and a reduction in the junction resistance.

Gold with a work function $q\phi_{Au}$~ 5.2 eV in contact with n-Si produces a Schottky barrier ~0.8 eV; however, formation of gold silicide significantly decreases (T >350 °C) the barrier height in the way that gold silicide in contact with n-Si makes Ohmic like junction and it is normally used to make Ohmic contact into the n-Si for different applications [131-133]. Considering an Ohmic contact for both PEDOT:PSS/Au and Au/n-Si, PEDOT:PSS/Au/n-Si should exhibit an Ohmic behavior.

Chapter Three

Experimental Method

Fully Ohmic behavior at all inner contact junctions, PEDOT:PSS/ n-Si microwires and PEDOT:PSS/ p-Si microwires, is desirable for highly efficient water-splitting cells. It has been estimated that a 7 µm square array of semiconductor microwires with diameter of ~ 1.5 µm, length of ~100 µm generates a maximum of ~21nA photocurrent in each microwire by absorption of photons from the global AM 1.5 spectrum [134]. An electrical resistance < 0.5 MΩ for the microwire/membrane structure guarantees less than 1% IR losses (1% of 1.23V, ~10mV) for an idealized solar water splitting system. The resistance of the junction formed between the n-silicon microwires and the p-type conducting membrane is the largest contribution to the end-end resistance of this system [26, 27, 110]. Modification of the methyl-terminated n-Si microwires base either by increasing the doping concentration of carrier or adding a metallic interfacial layer suggests an improvement in the contact behavior because this approach narrows down the depletion region at polymer/ microwire junction and facilitate quantum mechanical tunneling of charge carriers.

A direct-contact formation technique was used to investigate the electrical properties of the junction between the conducting polymer membrane (PEDOT:PSS) and four different types of methyl-terminated n-type silicon microwires. They were: highly-doped microwires (n^+-Si), highly- doped base microwires (nn^+-Si), highly- doped base microwires with copper (Cu) interface at low-doped end (Cu/nn^+-Si), and highly- doped base microwires with gold (Au) interface at low-doped end (Au/nn^+-Si) (Fig 3.1).

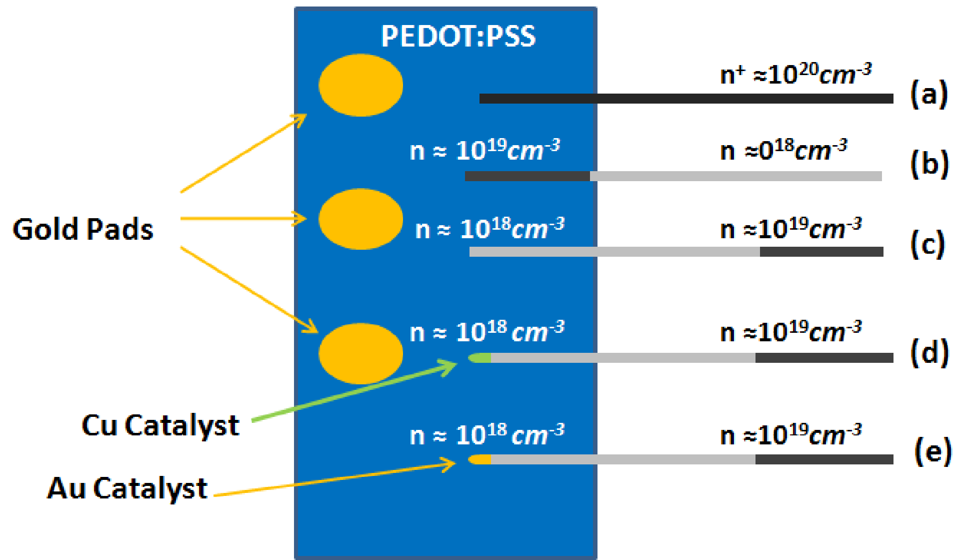

Figure 3.1: Schematic diagram for junction between PEDOT:PSS and methyl-terminated n-type silicon microwires (a) highly-doped microwires (~10^{20} cm^{-3}), (b) highly- doped base microwires with highly-doped base in contact (~10^{19} cm^{-3}), (c) highly- doped base microwires with low-doped end in contact (~10^{18} cm^{-3}), (d) highly- doped base microwires with copper (Cu) interface at low-doped end (e), and highly- doped base microwires with gold (Au) interface at low-doped end .

In order to investigate electrical properties of n-Si microwire/membrane systems, single microwires needed to be isolated and form electrical connections into the candidate polymer membrane. In this chapter, the experimental methods that were used to

characterize individual solar water splitting cells, including sample preparation, isolation of the microwires, conducting polymer film preparation and microwire/polymer junction formation are explained in detail.

3.1 Silicon Microwires

Silicon microwires were grown by collaborators in the Lewis group at California Institute of Technology (Caltech) using vapor liquid solid (VLS) chemical vapor deposition (CVD) from Si (111) wafers patterned with copper (Cu) or gold (Au) catalyst. The samples were doped with phosphorus (P) up to different doping concentration levels in a square arrangement with a 7 μm pitch [83, 89, 101, 135, 136]. The highly doped base microwires were grown in two steps with different flows of PH_3 and durations. For instance, ~50 sccm of PH_3 for 2 min followed by ~1.6 sccm of PH_3 for 6 min produce ~40 μm highly-doped base (~10^{19} cm^{-3}) with ~80 μm remaining (low-doped~10^{18} cm^{-3}).

3.1.1 Highly-doped Microwires: n^+-Si

Highly-doped microwires (n^+-Si) were uniformly grown with doping concentration ~10^{20} cm^{-3} from Si wafers patterned with copper (Cu) catalyst (Fig 2.8) [83, 89, 101, 135, 136]. The microwires were 1.5 μm in diameter and 80-85 μm in length and were arranged in a square pattern with a 7 μm pitch. The metallic growth catalyst, Cu, was removed using a two-step etching procedure conducted prior to surface treatment (methyl-termination) of microwires [27].

3.1.2 Highly-doped Base Microwires: nn^+-Si

Microwires with a modified base (nn^+-Si) were grown using copper catalyst in two steps. The microwires were 60-70 μm in length and 1.5 μm in diameter and were arranged in a square pattern with a 7 μm pitch. The initial (20-30 μm) (base) was grown with a doping concentration $\sim 10^{19}$ cm^{-3} and the remaining (30-40 μm) was grown with a doping concentration $\sim 10^{18}$ cm^{-3}. The metallic growth catalyst, Cu, was also removed using a two-step etching procedure conducted prior to surface treatment of microwires [27].

3.1.3 Metallic-capped Microwires: Cu/nn^+-Si

The n-doped Si microwires were fabricated similarly to the microwires with a modified base (above) in two steps. These Si microwires were 30-40 μm in length and 1.0 μm in diameter and were arranged in a square pattern with a 7 μm pitch. The base with 15-20 μm in length was grown with a doping concentration $\sim 10^{19}$ cm^{-3} and the remaining (low-doped) with 15-20 μm was grown with doping concentration $\sim 10^{18}$ cm^{-3}. The microwires did not undergo the metallic growth catalyst removal process and the copper catalyst was retained on the low-doped region. The microwire surfaces were functionalized with methyl groups to ensure CH_3-Si termination, exploiting the kinetic stability of the Si-C bond to minimize oxide formation [62, 65, 78]. This termination was achieved using a two-step chlorination-alkylation process [62, 65, 66, 78].

3.1.4 Metallic-capped Microwires: Au/nn$^+$-Si

The n-doped microwires (Au/nn$^+$-Si) were grown with 120 μm length using gold catalyst in two steps. The base with ~40 μm in length was grown with a doping concentration ~10^{19} cm^{-3} and the remaining (low-doped) with ~80 μm was grown with doping concentration ~10^{18} cm^{-3}. These Si microwires were 1.0 μm in diameter and were arranged in a square pattern with a 7 μm pitch. The gold (Au) catalyst at the top of each microwire did not undergo the metallic growth catalyst removal process. The microwires were functionalized with methyl groups using a two-step chlorination–alkylation procedure [62, 65, 66, 78].

3.2 Ohmic-Contact to Silicon Microwires

The microwires were removed from the growth substrate by scraping a corner of the substrate using a razor blade and were pushed onto a glass substrate. The electrical characterization on individual microwires and microwire/polymer junctions were performed on glass substrates in order to eliminate unwanted conduction paths into the substrate (Fig 3.2).

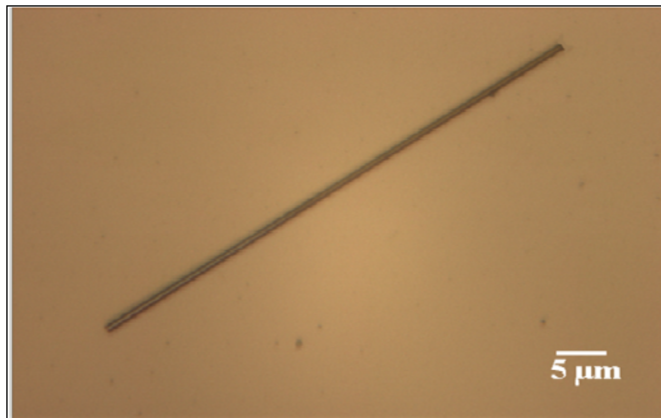

Figure 3.2: Optical micrographs of microwires isolated on a glass substrate.

In order to make electrical measurements, there exist many techniques to form Ohmic contacts to individual Si microwires. Direct-contact formation employing tungsten probes (W) (with a diameter of ~2 μm) eliminates the lithographic and high temperature micro-fabrication processes for contact formation that they are not compatible with combination of microwire/polymer systems [90, 137]. This technique is an inexpensive measurement compared to micro-fabrication based techniques and provides a simple, fast and more flexible method to characterize microstructure systems such as solar water splitting system. This non-destructive approach provides this ability to repeat measurements on a system under different conditions (Fig 3.3).

The contact between tungsten probe and silicon is naturally a Schottky contact. However, electronic band structure of Si has been reported to vary as a function of pressure on the lattice structure. The pressure that needs to be applied to silicon to make a transition from a semiconducting to a metallic phase is ~11 GPa, i.e. ~11 $mN\mu m^{-2}$ [138]. The transition from a semiconducting to metallic phase leads to change the Schottky contact to an Ohmic contact. Therefore, the application of sufficient local mechanical pressure on silicon structure using tungsten probes (W) can make a direct and reliable Ohmic contact to the Si microwires [26, 110]. The pressure applied to the Si microwire by the probe during the measurements can be estimated by measuring the force of the probe holder setup using a balance [28]. In this case, the probe holder was placed on a balance and the balance is then tared. Next, the probe was lowered until the recorded weight was saturated and a constant weight ~ 3.8 g was achieved. The weight shows that a maximum value of ~37.3 mN force exerted on the microwires by the W probes. Assuming a maximum circular contact diameter of 2 μm (the maximum diameter of the

microwires), the local mechanical pressure at the point of contact is > 12 mNμm^{-2} which is enough to pass the reported metallic transition threshold (~11 mNμm^{-2}) [138]. The contact area was overestimated to obtain the minimum amount of pressure [28]. Consequently, the basic electrical properties of a single Si microwire and Si microwire/polymer junction can be extracted using a standard probe station (Fig 3.3) [26, 27, 110].

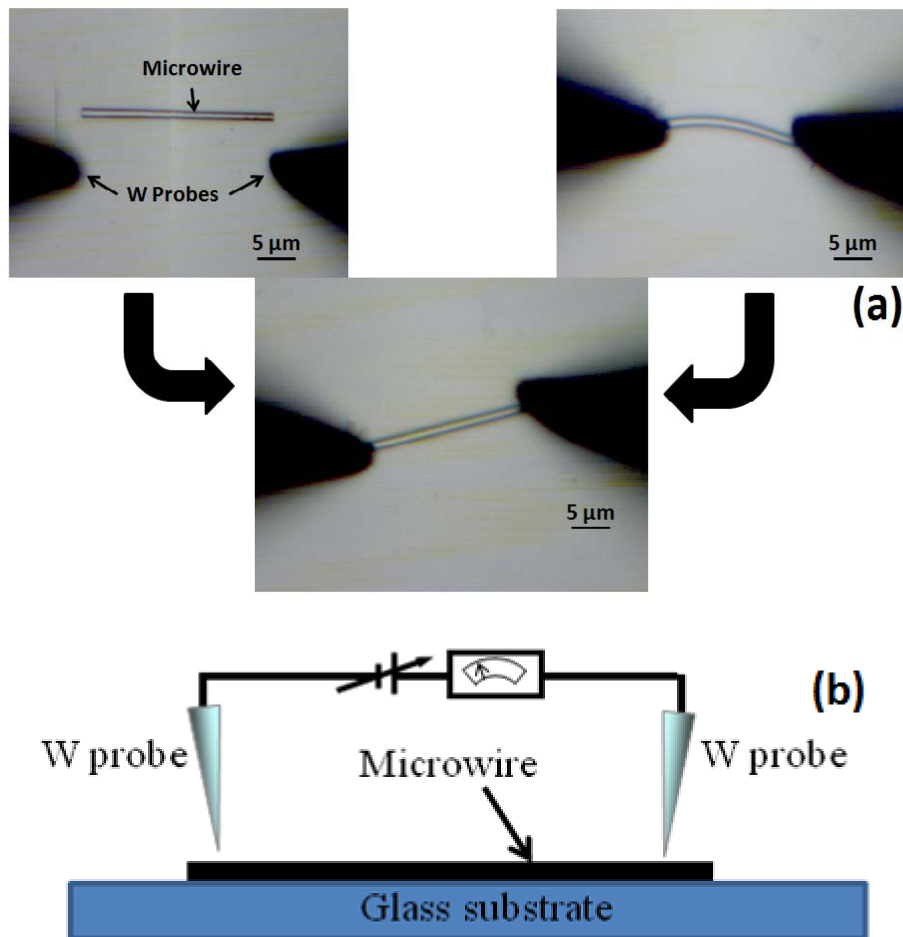

Figure 3.3: a) Optical micrograph of an isolated Si microwire on a glass substrate. The tungsten probes are approaching from the above to make contact with the microwire. It is possible to move microwire along the microwire and make resistance measurement at different probes spacing. b) Schematic diagram for resistance measurement along an individual Si microwire using tungsten probes [110].

3.3 PEDOT:PSS/Si microwire Assembly

PEDOT:PSS was purchased from HC Stark (Newton, MA) in the form of *Clevios F HC* (highly conductive blend 3.5 wt % in dimethyl sulfoxide, density 0.95 g/L). Samples of the conducting polymer (PEDOT:PSS) were spin coated at 2000 rpm for 20 seconds on glass substrates with prepositioned Parafilm masks separated by 0.5 cm, yielding a film thickness of 150-200 nm . The thickness of the film was determined using the function of thickness measurement of the four-point probe instrument. The results of measurements were also verified using Alpha-step profilometer technique. The four point probes technique measures the average resistance (R), resistivity (ρ), sheet resistance (R_s) and thickness (t) of a thin layer by passing current through the outside two points of the probe and measuring the voltage across the inside two points. The sheet resistance of the polymer film, $R_s \sim 600\ \Omega/\square$, is measured using four-point probe measurement (Fig 3.4 a). The unit for sheet resistance is the ohm; however, it is specified in unit of "ohms per square" to avoid confusion between R and Rs. The resistance of the polymer was also obtained from, $R_{polymer} = R_S \frac{\ell}{w} \sim 120\ \Omega$ [139], where W~ 2.5 cm and the length was L ~ 0.5 cm. After removal of the Parafilm masks, the microwires were scraped onto the substrate adjacent to the border between the conducting polymer and the substrate. Using the tungsten probes, single microwires were positioned perpendicular to the border between the conducting polymer and the glass substrate. The microwires were then inserted into the polymer by pushing microwires using the tungsten probes. Good electrical contact between the polymer and microwire was ensured by covering the 7-10 μm of the microwire that was in contact with the polymer with a small amount (<10 μL)

of the polymer solution. The contact area between microwires and the polymer is obtained by, $A=\pi(d/2)^2+\pi d\ell$,where ℓ is the length of microwires in contact with polymer and d is the diameter of microwires (Fig 3.4 a); and it is A~ 18×10^{-8}-25×10^{-8} cm^2 for microwires with d~1.5 μm and A~ 12×10^{-8}-16×10^{-8} cm^2 for microwires with d~ 1 μm. The n-Si microwire/polymer assembly was used as a model for a half cell of the proposed solar water splitting microwire array cell (Fig 3.4 b).

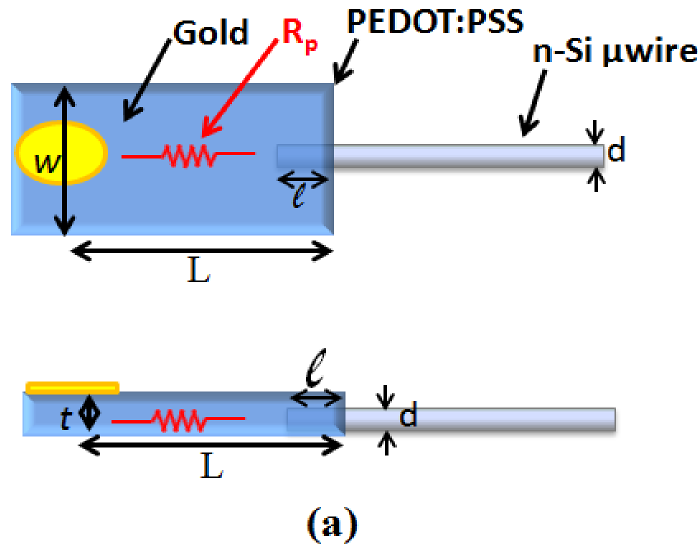

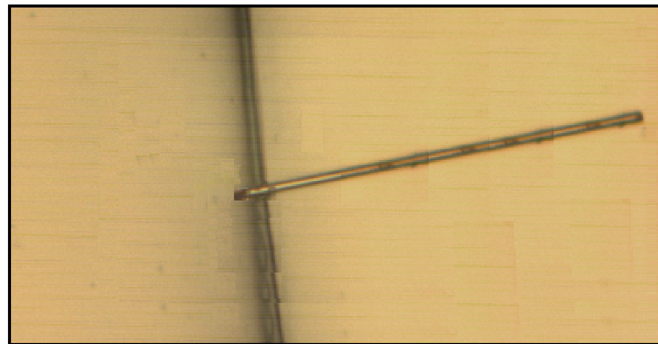

(b)

Figure 3.4: **(a)** The design used to the test half cell of artificial photosynthesis cells in this study. The thickness is t~ 200 nm, the width is W~ 2.5 cm and the length L ~ 0.5 cm for PEDOT:PSS thin film spin coated on a glass substrate. **(b)** Optical micrograph of a Si microwire embedded in to the polymer.

Contact pads on the polymer films were formed by sputtering gold through an aluminum shadow mask with circular apertures (5 mm diameter, 9 mm center to center spacing). The resulting 32 nm thick gold pads have been shown to form an Ohmic contact between the polymer and tungsten probes (Fig 3.5).

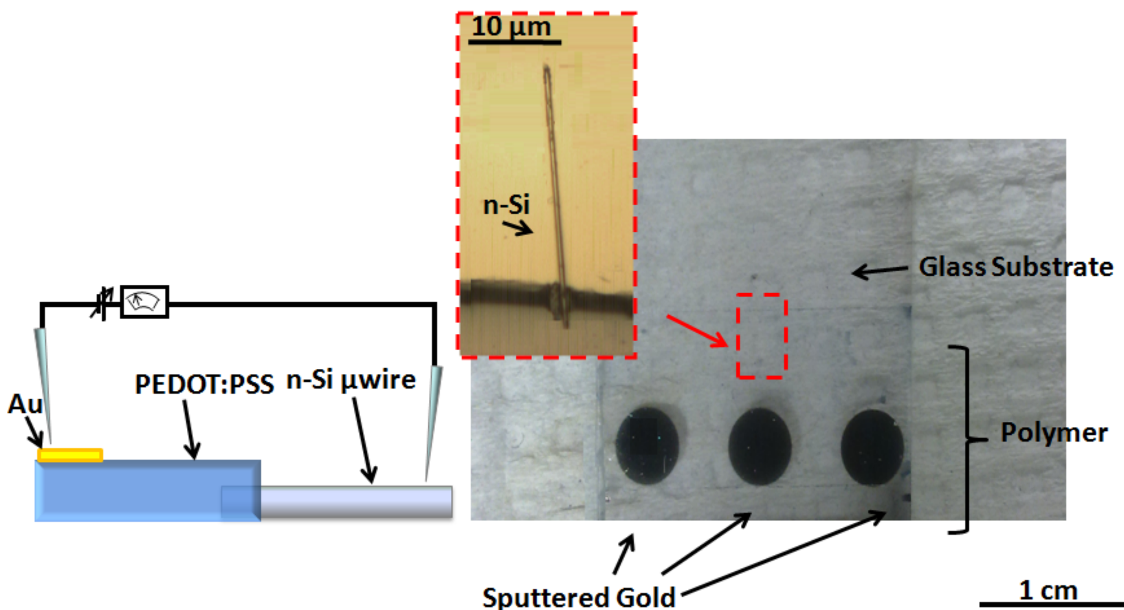

Figure 3.5: (a) Schematic diagram for a single microwire/polymer junction. It displays a microwire aligned at the polymer border and contact gold pads on the polymer films to provide Ohmic contact between the polymer and tungsten probe. (b) Optical micrograph of the half cell of artificial photoelectrolysis system under test.

3.4 Instrumentation

To make an Ohmic contact to the polymer, an *Edwards s150b* sputter coater was used to sputter Au pads onto the polymer surface. Direct Ohmic contacts were formed using tungsten probes (W) from *American Probes & Technologies* model *72T-G3/10* (with a diameter of ~2 µm) (Fig 3.6).

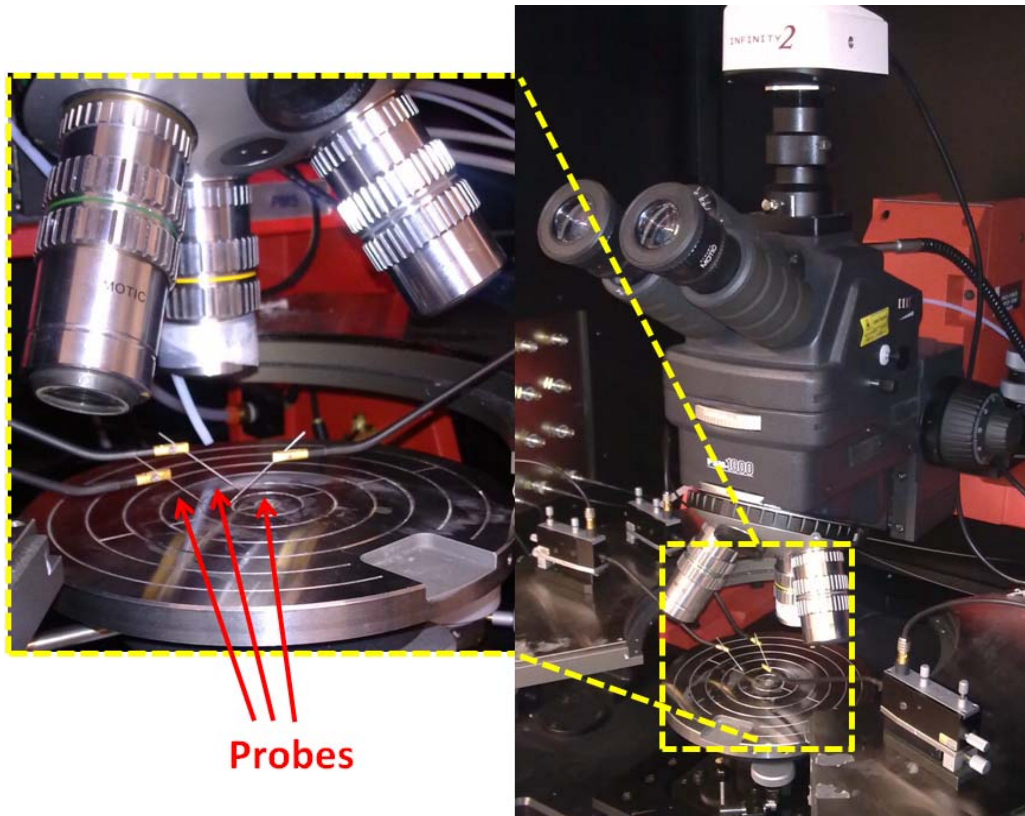

Figure 3.6: *I-V* measurements were performed using an *Agilent 4155c* semiconductor parameter analyzer in a standard probe station. The stage, four W probe holders and the microscope are shown in the right side image. W probes can be seen in the magnified image on the left.

In order to improve the quality of the contacts formed, the tungsten native oxide were removed by etching the probes for ~1 min in 2.0 M KOH(aq.) immediately before the experiments. Upon the direct-contact formed using standard tungsten probes (diameter of ~2 μm) in a *Suss MicroTec* standard probe station (Fig 3.6), current flows through the system was recorded for different applied voltage using an Agilent 4155c semiconductor parameter analyzer.

A four point probe is a simple apparatus for measuring the resistivity of semiconductor samples. By passing a current through two outer probes and measuring the voltage through the inner probes allows the measurement of the substrate resistivity. FPP 5000 -

four point probe manufactured by Miller Design and Equipment was used to measure the sheet resistance of the polymer film spin coated on a glass substrate with thickness of 150-200 nm. The thickness of the polymer was measured using the function of thickness measurement of the four-point probe instrument. The results of the thickness measurements were also verified by using **a KLA-Tencore AS-500 Alpha-Step which quantitatively measures the 2D topography of surfaces.**

Chapter Four

Results and Discussion

4.1 Results

There are two possible approaches to change the band structure of methyl-terminated n-Si microwire/PEDOT:PSS junction, yielding an improvement in the electrical behavior of the system. One approach is raising the doping concentration of the microwires to lower the depletion region width. A narrow depletion layer facilitates quantum mechanical tunnelling of the charge carriers, increasing the conductivity of the structure. Another practical approach is addition of a metallic interfacial layer to reduce the Schottky barrier height at the contact with semiconductor and make Ohmic contact with conducting polymer. This work reports the electrical behavior of the junctions formed between a conducting organic polymer, PEDOT:PSS, and highly-doped microwires (n^+-Si) and highly-doped base microwires (nn^+-Si, n^+ in contact) as well as the electrical behavior of junctions formed between the conducting polymer and the low-doped end of highly-doped base microwires (nn^+-Si, n in contact). The current-voltage responses of the junctions with the presence of a metallic layer (copper or gold) at the polymer/microwires interface were also studied. These junctions are formed by embedding copper-capped

(Cu/nn^+-Si) and gold-capped (Au/nn^+-Si) highly-doped based microwires in the membrane.

Figure 4.1 demonstrates the measurement system that was used to study the n-Si microwire/PEDOT:PSS junction. It resembled a half cell of the proposed artificial photosynthesis device structure in which microwires were physically embedded in the polymer film layer.

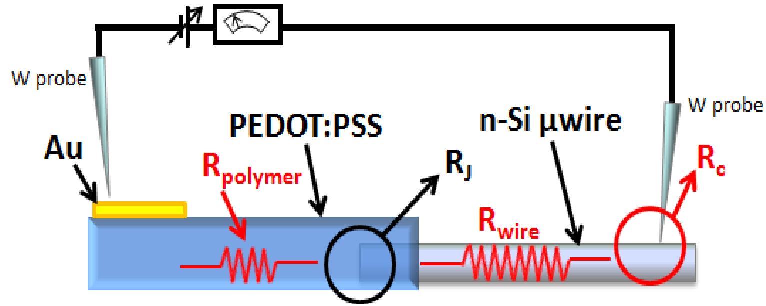

Figure 4.1: Schematic diagram of polymer/n-Si microwire junction measurements. This structure is used as a representation for the water splitting half-cell system in which n-type Si microwires aligned at the PEDOT:PSS /glass border

Taking the sputtered Au/PEDOT:PSS with well-defined Ohmic contact into consideration, the total resistance of such a system includes the contribution of the tungsten probe/microwire contact resistance (R_c); the microwire resistance (R_w); the microwire/polymer junction resistance (R_J); and the polymer film resistance (R_p) as follows:

$$R_{total} = R_c + R_w + R_J + R_p \quad (4.1)$$

Measurement of R_{total}, R_w, R_c and R_p allows calculation of the polymer/n-Si microwire junction resistance. Having known R_p~120 (Sec 3.3), R_w, R_c and R_{total}, were other main parameters in the final measurement structure (Fig 4.1) and estimating those allows for

calculation of the microwire/polymer junction resistance (R_J). R_w and R_c using the resistance measurement along single microwires were measured (Sec 4.1.1); and R_{total} using the resistance measurement of the polymer/microwires assemblies was determined (Sec 4.1.2).

4.1.1 Resistance Measurement of Single Microwires

The microwires were scraped from the growth substrate onto the glass substrate to perform resistance measurements on them. Then, the tungsten probes were moved down to the microwire until the contacts formed. The soft physical contact between the probes and Si microwires led to Schottky contact. This Schottky contact changed to Ohmic contact as the applied force by the probes on Si microwire was gradually increased to the threshold force level (~11 mNμm^{-2}) [26, 28]. The current flowing through the system was recorded for a range of applied voltages (-1, +1) in the forward (trace) and reverse (retrace) directions of voltage. Both I-V profiles were checked to see if trace and retrace were tracking each other well (i.e. look the same). I-V profiles (trace and retrace) for different probe separations were linear, and this was expected due to the Ohmic contact formation to the silicon microwires (Fig 4.2). The I-V curves show a resistance ~ 0.5 kΩ associated with ~5 µm of the n-Si microwire (120 µm long) with ~1 µm diameter.

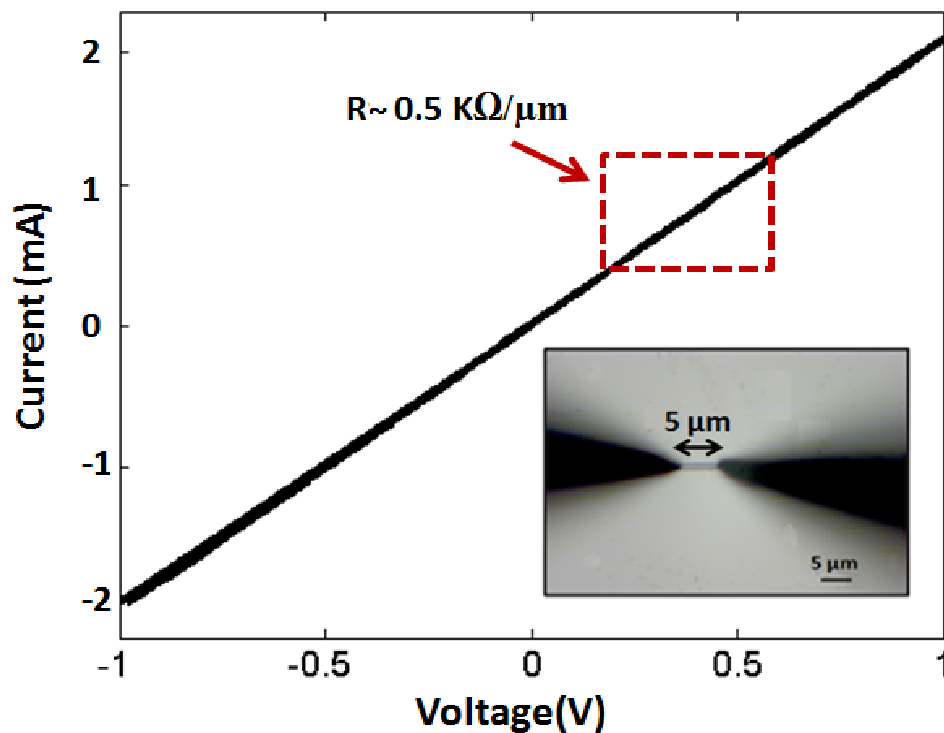

Figure 4.2: An example of the initial I-V measurement results for the probe spacing ~5µm on the n-Si microwire (120 µm long) with ~1 µm diameter and doping density of ~ 10^{19} cm^{-3}.

The electrical DC resistance of system was calculated from the slope of I-V curve. This technique provided the ability to form an Ohmic contact to each arbitrary point along microwires and obtain the resistance. It was possible to freely decrease or increase the probes separation across the length of the microwires and make resistance measurements versus probe separation (Fig 4.3). This information (resistance versus spacing) was used to determine the basic electrical properties of individual Si microwires (doping density along microwire).

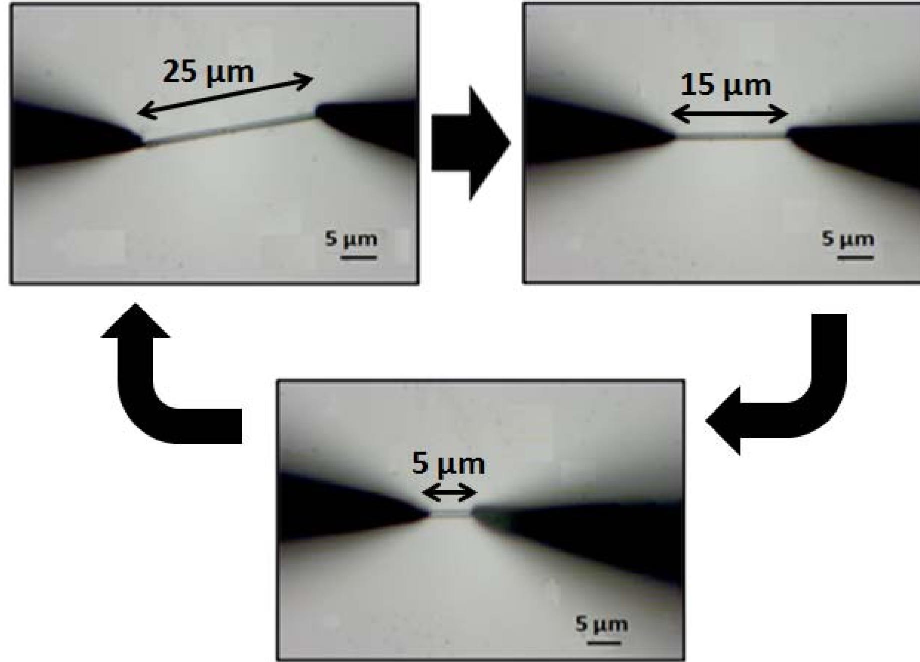

Figure 4.3: Contact formation along individual n-Si microwires (~1µm in diameter and ~120µm long) to make resistance measurement versus probe separation.

The gradient of the measured data (Ω/µm) was used to estimate the resistivity of the microwire and, in turn, the doping concentration for highly-doped and low-doped regions. The electrical resistivity ρ for a conductor similar to these microwires with a uniform cross section and a uniform flow of electric current is defined as:

$$\rho = R\frac{A}{\ell}, \tag{4.2}$$

where R is the electrical resistance of specimen (Ω), ℓ is the length of specimen (*cm*) and A is the cross-sectional area of the specimen (cm^2). In the case of silicon microwires, $\frac{R}{\ell}$ is the resistance per unit of length (Ω*/cm*) extracted from the slope of the line fitted to the data. The general formula for the resistivity is,

$$\rho = \frac{1}{q(\mu_p p + \mu_n n)}, \tag{4.3}$$

where q= 1.6×10^{-19} C, n is concentration of electrons (cm^{-3}), μ_n is electron mobility (cm^2/V.s) , p is concentration of holes (cm^{-3}), μ_p is hole mobility ($cm^2/V.s$). In the case of n-type semiconductors ($n >> p$), (4.3) can be simplified to $\rho = \frac{1}{q\mu_n n}$. The measured drift mobility is a function of doping density and is shown in Figure 4.4 [30, 140].

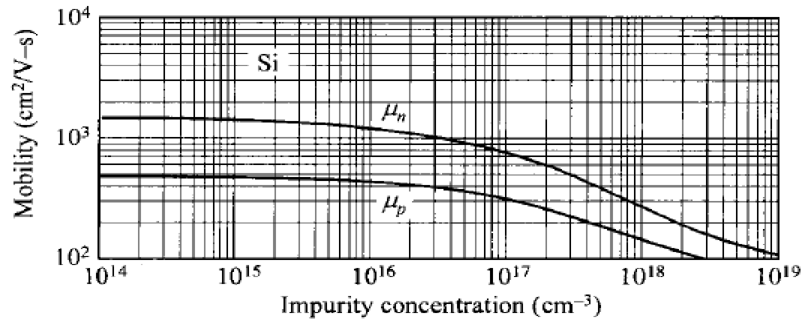

Figure 4.4: Drift mobility of Si at 300 K versus impurity concentration. Adapted with permission from[140]. Copyright (1993) Solid-State Electronics.

Referring to the resistance measurement performed (resistance ~ 0.5 k**Ω**) on ~5 µm of the n-Si microwire with ~1 µm diameter and doping density of ~ 10^{19} cm^{-3}, the resistance per length of $\frac{R}{\ell}$ ~ 100 **Ω**/µm resulted in a doping concentration of electrons n~ 6×10^{18} cm^{-3}. The result of the measurement was consistent with the expectation n~ 10^{19} cm^{-3}.

4.1.1.1 Highly-doped Microwires: n$^+$-Si

Ohmic contacts were formed to n$^+$-Si, at different spacing of the probes in which the probes was completely disconnected from the microwire before the contact for the next measurement was made (Fig 4.4). Figure 4.4 demonstrate the results of resistance

measurement for one pair of microwires and were verified by repeating the experiment with five other microwires from different regions of the growth substrate received in a batch. A linear fit was performed to the measured resistances versus contact separation with regression coefficient of r^2 ~ 0.99. The regression coefficient of r^2 >0.9 were measured for the data associated with all tested microwires. The uniform slope of the fitted line reflects constant resistance per length of ~10 Ω/μm and uniformity in the doping distribution over the length scale under consideration (μm).

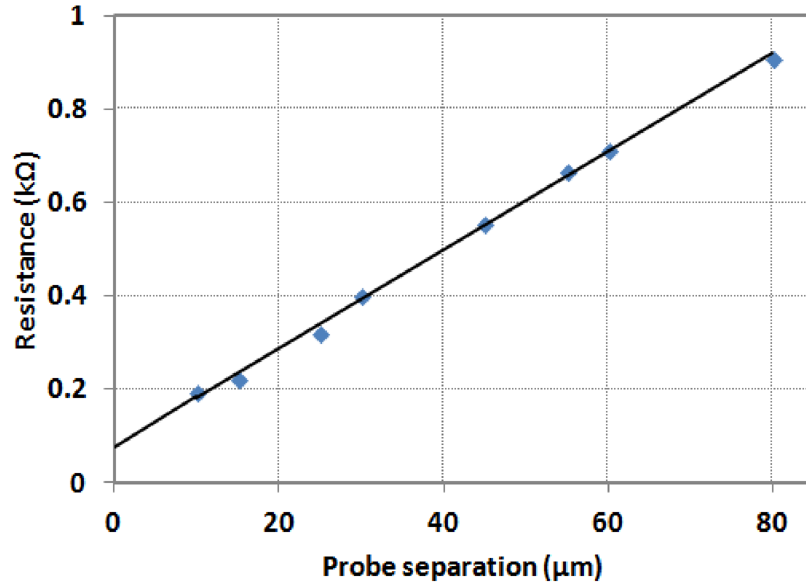

Figure 4.5: Contact resistance measurements for n^+-Si microwires with 1.5 μm diameter. The results shown here represent one microwire and were verified by repeating the experiment with five other microwires from different regions of the growth substrate received in a batch. The linearity of the data along the length of microwires (squares) reflects the uniformity of the doping concentration within each region at the length scale considered.

The resistance per length of $\frac{R}{\ell}$~ 10 Ω/μm resulted in a doping concentration of electrons $n \sim 2\times10^{20}$ cm^{-3}. The measured doping concentration of the microwires in these

measurements (on six microwires from different regions of the growth substrate) was consistent with the known doping concentration based on the fabrication process.

For the all resistance measurements along the microwires, the tungsten probes/microwire junction resistances ($2R_c$) were added to the resistance of microwires due to the contact formation. The intercept of the line fitted to the data (~ 80 Ω) presented the tungsten probes/microwire junction resistances ($2R_c$). Each probe-microwire contact resistance (R_c ~ 40 Ω) was half of the intercept value ($2R_c$ ~ 80 Ω). The probe-microwire contact resistance (R_c ~ 40 Ω) exhibited a negligible contribution to the total measured microwires resistances. The maximum resistance obtained for the length of these microwire (~ 80 μm) were R_w ~ 0.8 kΩ.

4.1.1.2 Highly-doped Base Microwires: nn^+-Si

The resistance measurements results for nn^+-Si are displayed in Figure 4.5. The measurements were performed in two directions between the top and the base of microwires. The results were obtained from one microwire and were verified by repeating the experiment with three other microwires from different regions of the growth substrate. Three independent resistance measurements were conducted at each point on the microwires to demonstrate the reliability and reproducibility of the Ohmic contacts performed. For each measurement, the probe was completely disconnected from the microwires before the contact for the next measurement was made.

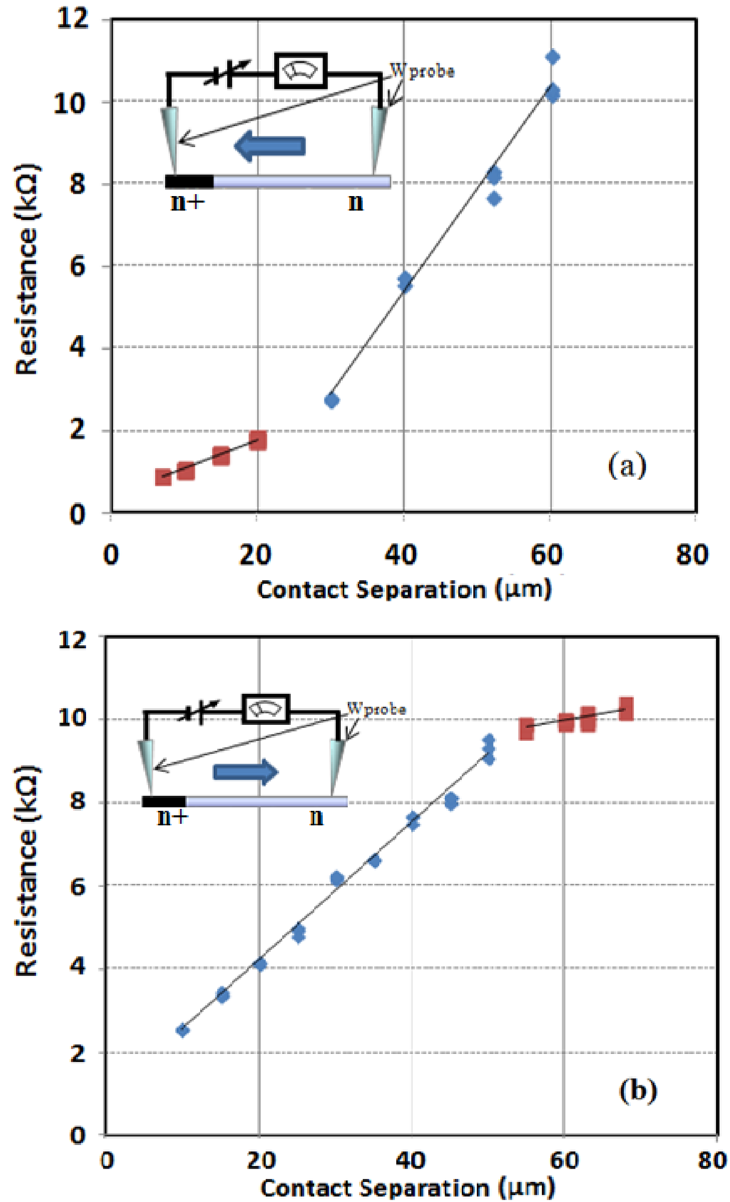

Figure 4.6: Contact resistance measurements for nn^+-Si microwires with 1.5 µm diameter. Three independent measurements were carried out for each selected point along the microwire and were conducted in both directions, from (a) the top to the base and (b) the base to the top. The results shown here represent one microwire and were verified by repeating the experiment with other microwires from different regions of the growth substrate. The linearity of the data within the highly-doped base (diamonds) and remainder of the microwires (squares) reflects the uniformity of the doping concentration within each region at the length scales considered.

The slope of the line fitted to the data in both directions changed once, yielding a change in doping concentration of carriers along the silicon microwire. The constant slope of the lines showed the uniform distribution of carriers within each region.

Fig 4.5.a depicts the resistance versus probe separation for when a probe was held at the highly-doped end of the microwire and a second probe was moved from the opposite end of the microwire toward the highly-doped region. Two lines were fitted to the data for highly-doped base (squares) with r^2 ~0.99 and for the remainder of the microwire (diamonds) with r^2~ 0.98. In the case of all microwires tested, $r^2 > 0.9$ were measured.

The slope of the fitted line was 70 Ω/μm for the base and 250 Ω/μm along the remainder of the microwire. The resistivity associated with these measurements corresponded to doping concentrations of ~4×10^{19} cm^{-3} and ~4×10^{18} cm^{-3} for the highly-doped and low-doped regions respectively.

The presence of a transition in doping concentration at ~30% of the microwire length (as measured from the base of the microwire) and the doping concentration within each region were consistent with expectation based on the microwire growth conditions. The intercept of the line fitted to the resistance versus probe separation data exhibited negligible tungsten probe-microwire contact resistance $2R_c$ ~ 900 Ω contributed in the resistance measurement. R_c increased about an order of magnitude for n^+n-Si microwires (~10^{18}-10^{19} cm^{-3}) compared with n^+-Si microwires (2×10^{20} cm^{-3}). This is consistent with the expectation based on eq 4.3 demonstrating a direct correlation between the doping concentration of carriers and the resistance.

Figure 4.5.b depicts the results for the resistance measurement conducted in the reverse direction. In this case, both probes were at the highly-doped base of a microwire at the beginning. Then, one of the probes was held at the base, while the second one was moved far to the opposite end of the microwire. Two lines were fitted to the data for the highly-doped base (squares) and for the remainder of the microwire (diamonds) with $r^2 \sim 0.97$ ($r^2 > 0.9$ for all microwires tested in the growth substrate).

The slope of the fitted line was 30 Ω/µm within the highly-doped base and 170 Ω/µm within the low-doped region. These gradients correspond to doping concentrations of $\sim 2\times10^{19}$ cm^{-3} and $\sim 3\times10^{18}$ cm^{-3} for the highly-doped region and the remainder of the microwire respectively.

The intercept of the line fitted to the data showed probe-microwire contact resistance to be $2R_c \sim 400$ Ω. It showed a very small contribution to the resistance measurements. The maximum resistance obtained for the length of these microwire (60-70 µm) was $R_w \sim 9$ kΩ.

4.1.1.3 Metallic-capped Microwires: Cu/nn^+-Si

Figure 4.6 presents the resistance versus contact separation obtained from direct-contact formation on Cu/nn^+-Si. The results were obtained from one microwire and were verified by repeating the experiment with three other microwires from different regions of the growth substrate.

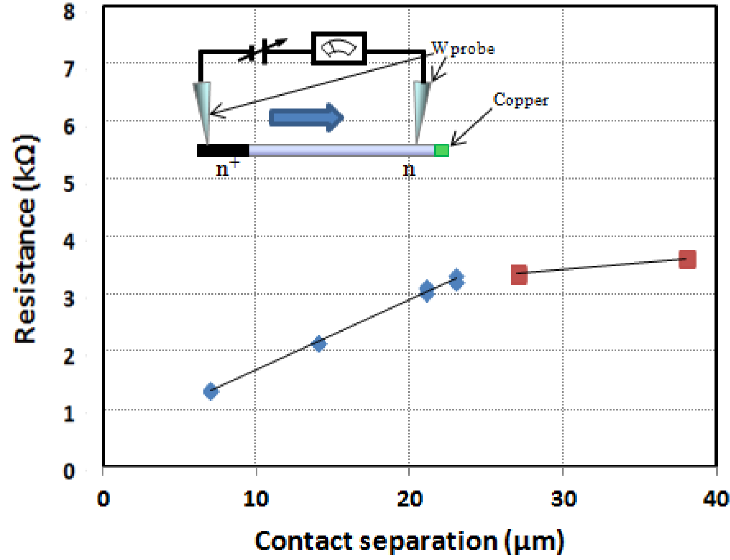

Figure 4.7: Contact resistance measurements for Cu/nn$^+$-Si microwires. These microwires were 1 µm in diameter. The results shown here represent one microwire and were verified by repeating the experiment with three other microwires from different regions of the growth substrate. Three independent measurements were carried out for each selected point.

In this resistance measurement, a probe was held at the highly-doped end of the microwire and a second probe moved from the opposite end of the microwire toward the probe at the highly-doped region. The resistance measurements were performed three times at each point along the silicon microwire.Two lines were fitted to the data (Fig 4.7) for highly-doped base (squares) and for the remainder of the microwire (diamonds) with regression coefficient of r^2~ 0.98 and r^2~ 0.99, respectively ($r^2 > 0.9$ was measured for all tested microwires).

The constant slope of the lines within each region reflected the uniform doping concentration of electrons. The slope of the fitted lines within highly-doped and low-doped regions were 25 Ω/µm and 120 Ω/µm, respectively. These gradients in the slope of

the line yielded doping concentrations of ~4×10^{19} cm^{-3} and ~4×10^{18} cm^{-3} for the highly-doped region and low-doped region respectively.

The probe-microwire contact resistance Rc ~ 200 Ω exhibited a small contribution to the resistance measurement. The maximum resistance obtained for the length of these microwires (35-40 μm) was R_w ~ 3 kΩ.

4.1.1.4 Metallic-capped Microwires: Au/nn^+-Si

To perform the resistance measurement on Au/nn^+-Si, a probe was held at the highly-doped end of the microwire and a second probe moved from the opposite end of the microwire toward the highly-doped region (Fig 4.7). The results were obtained from one microwire and were verified by repeating the experiment with three other microwires from different regions of the growth substrate. To validate the data obtained at each point, three independent resistance measurements were conducted at each point along the microwires. Two lines were fitted to the data (Fig 4.7) for highly-doped base (squares) and for the remainder of the microwire (diamonds) with regression coefficient of r^2~ 0.97 and r^2~ 0.91, respectively ($r^2 > 0.9$ was measured for all tested microwires).

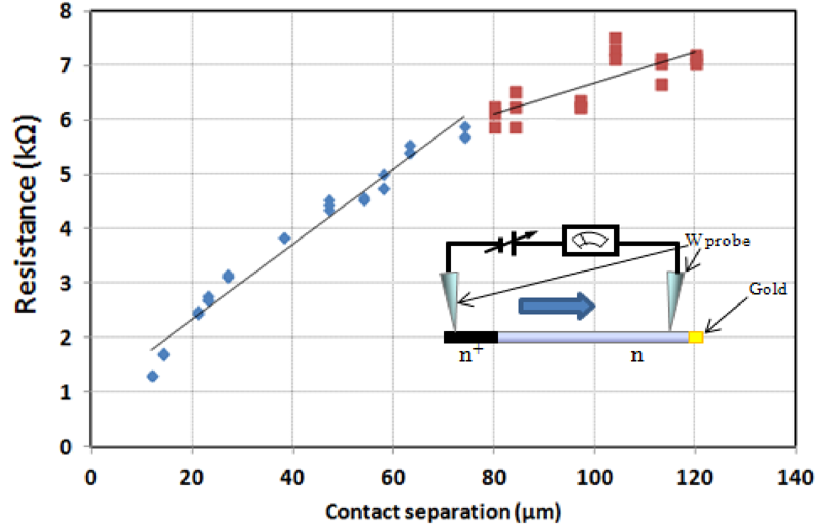

Figure 4.8: Contact resistance measurements for Au/nn^{+}-Si microwires. The results shown here represent one microwire and were verified by repeating the experiment with other microwires from different regions of the growth substrate received in a batch. These microwires were 1 µm in diameter. Three independent measurements were performed for each selected point along microwire.

The slope of the line fitted to the data varied once along silicon microwires and it yielded a change in doping distribution of carriers along the microwire. The slope of the lines was constant within each region and it implied uniform doping concentration of electrons.

The slope of the fitted line within highly-doped and low-doped regions was 20 Ω/µm and 100 Ω/µm, respectively. The doping concentrations calculated from the gradient of fitted lines were ~4×10^{19} cm^{-3} and ~6×10^{18} cm^{-3} for the highly-doped and low-doped regions, respectively.

The intercept of the line fitted to the data ($2Rc$ ~ 900 Ω) implied a small contribution attributable to probe-microwire contact resistance. R_w ~7 kΩ was the maximum resistance which might be obtained for the length ~120 µm of these microwires.

4.1.1.5 Electrical properties of n-Si Microwires

The doping concentration for highly-doped and low-doped regions and the maximum resistance represented by a microwire (R_w) and the individual tungsten probe/microwire contact resistance (R_c) for all sets of microwires obtained by making Ohmic contacts to individual microwires using W probes in a standard probe station are presented in Table 4.1.

Table 4.1: The results of resistance measurements on n-Si microwires using direct-contact technique by means of tungsten probes (W). Apart from the microwires with the copper and gold interface (1.0 μm in diameter) the microwires were 1.5 μm in diameter. R_w is representation of the maximum resistance one might obtain for the length of the wire. The intercept of the line fitted to the resistance versus probe separation data presented tungsten probe-microwire contact resistances (R_c) contributed in the resistance measurements.

	Intercept (kΩ) ±1%	Slope (Ω/μm) ±2%		Doping Cons. (cm^{-3}) ±2%		R_w(kΩ) ±1%
		n^+	**n**	**n^+**	**n**	
n^+-Si	0.08	10	—	~2×10^{20}	—	0.8
nn^+-Si (top to base)	0.9	70	250	~2×10^{19}	~3×10^{18}	9
nn^+-Si (base to top)	0.4	30	170	~4×10^{19}	~4×10^{18}	8
Cu/nn^+-Si	0.4	25	120	~4×10^{19}	~4×10^{18}	3
Au/nn^+-Si	0.9	20	100	~4×10^{19}	~6×10^{18}	7

4.1.2 PEDOT:PSS/Si Microwire Junction

To study PEDOT:PSS/n-Si microwire junctions, resistance measurements were performed on the configuration demonstrated in Fig 4.8. The structure would represent a half cell of the eventual device structure in which one n-Si microwire was physically embedded in polymer film layer. One tungsten probe was held in contact with the

microwire while the second probe was in contact with a gold pad sputtered on the polymer in a standard probe station (Fig 3.6). Then, different voltages were applied and the current flowing through the system was recorded using an *Agilent 4155c* semiconductor parameter analyzer (Fig 3.6).

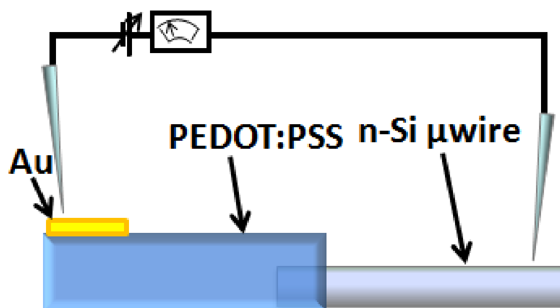

Figure 4.9: Schematic diagram of polymer/n-Si microwire junction measurements. This structure is used as a representation for the water splitting half-cell.

4.1.2.1 PEDOT:PSS/nn$^+$-Si Microwires

nn$^+$-Si microwires had ~20μm long highly-doped base (n$^+$) with doping concentration of 4×10^{19} cm^{-3} and ~40μm long low-doped region (n) with doping concentration of 3×10^{18} cm^{-3}. Prior to inserting a microwire into the conducting polymer film, tungsten probes were used to make two resistance measurements associated with 10 μm at both ends of the microwire to identify the low-doped end (n) with larger resistance and the high-doped end (n$^+$) with smaller resistance. In order to form PEDOT:PSS/nn$^+$-Si systems, 7-10 μm of the low-doped end were positioned perpendicular at the polymer/glass interface using tungsten probes, and inserted into the polymer by pushing the microwires. To form PEDOT:PSS/n$^+$n-Si combinations, 7-10 μm of the high-doped end were positioned at the polymer/glass interface, and inserted into PEDOT:PSS.

The I-V curve for PEDOT:PSS/nn^+-Si microwire showed an asymmetric profile and a strong rectifying behavior with total series resistance of R_{total} > 20 MΩ for small bias voltage < 10 mV (Fig 4.9.a). A very small leakage current of ~ 4×10^{-3} nA flowed through the junction at 10 mV and a bias voltage > 380 mV was necessary to have a 21 nA flow of current. The results presented in Figure 4.9.a were obtained from one microwire and were verified by repeating the experiment with another microwire from different region of the growth substrate.

I-V profile for PEDOT:PSS/n^+n-Si microwire systems were symmetric (non-rectifying) behavior compared with PEDOT:PSS/nn^+-Si for < 1 V (Fig 4.9.b). It also demonstrated resistance of R_{total} ~4.5 ± 0.3 MΩ for small bias voltages < 10 mV. A small bias voltage ~ 10mV led current ~1.73 nA through the system and a bias voltage >130 mV was required to be applied to the junction to have 21 nA current. The results presented in Figure 4.9.b were obtained from one microwire and were verified by repeating the experiment with two other microwires from different region of the growth substrate.

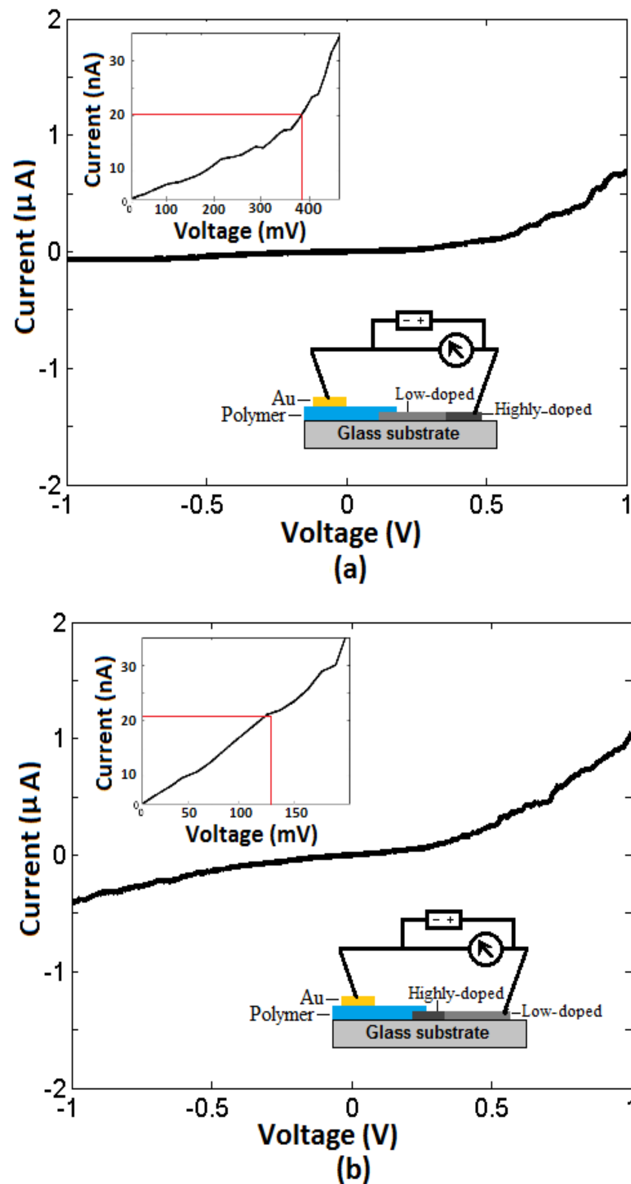

Figure 4.10: I-V profile for (a) PEDOT:PSS/nn^{+}-Si microwires and (b) PEDOT:PSS/n^{+}n-Si microwires. The microwires were 60-70 µm in length (~20 µm highly-doped and ~40 µm low-doped) and ~1.5 µm in diameter. The highly-doped base was 7-10 µm in contact with the conducting polymer. (a) I-V curve was asymmetric (rectifying) for voltages < 1 V with a very large total resistance of R_{total} > 20 MΩ for voltages < 10 mV. (b) The junctions exhibited a symmetric I-V curve (Ohmic-like behavior) compared with PEDOT:PSS/nn^{+}-Si and a total resistance 4.5 ± 0.3 MΩ (< 10 mV).The results shown here represent one microwire and were verified by repeating the experiment with other microwires from different region of the growth substrate.

4.1.2.2 PEDOT:PSS/n^+-Si Microwires

N^+-Si in the contact with the conducting polymer membrane (PEDOT:PSS/n^+-Si) displayed a symmetric I-V profile for large bias voltage < 1 V (Fig 4.10). A linear symmetric I-V curve with total series resistance of 4 ± 1 MΩ were observed for small bias voltages < 10 mV. The current level of 21 nA was anticipated to flow through system for V > 100 mV and the current of ~ 10.1 nA flowed through the junction at 10 mV. The results shown here represent one microwire and were verified by repeating the experiment with three other microwires from different region of the growth substrate.

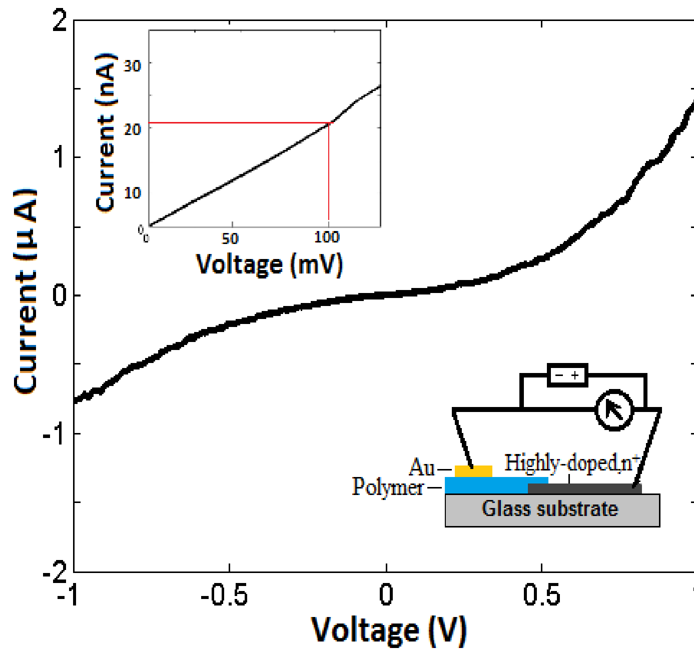

Figure 4.11: I-V characteristic for PEDOT:PSS/n^+-Si microwires. The microwires with ~80 µm length and diameter of ~1.5 µm were 7-10 µm in contact with the conducting polymer. PEDOT:PSS/n^+-Si microwire demonstrated a symmetrical I-V curve at large bias voltage (< 1 V). I-V curve is linear with end to end resistance of 4 ± 1 MΩ for small bias voltage (< 10 mV). The results shown here represent one microwire and were verified by repeating the experiment with other microwires from different region of the growth substrate.

4.1.2.3 PEDOT:PSS/Cu/nn$^+$-Si Microwires

Cu/nn$^+$-Si microwires had ~20μm long highly-doped base (n$^+$) with doping concentration of 4×10^{19} cm^{-3} and ~20μm long low-doped region (n) with doping concentration of 4×10^{18} cm^{-3} holding cold catalyst on the top (based on the fabrication process). Similarly to nn$^+$-Si microwires (Sec 4.1.2.1), the low-doped end (n) of Cu/nn$^+$-Si microwires holding copper catalyst were identified. Then, 7-10 μm of the end were inserted into the polymer film.

I-V characteristics of PEDOT:PSS/Cu/nn$^+$-Si showed a symmetric I-V curve for large bias voltage < 1 V (Fig 4.11). In comparison with PEDOT:PSS/nn$^+$-Si microwires (Sec 4.1.2.1), the presence of the copper at interface improved the I-V profile to a linear and symmetric one for small bias regime < 10 mV. It also improved the total resistance R_{total} ~ 3.4 ± 0.7 MΩ of such a system for small bias voltage < 10 mV. The current of ~ 3 nA flowed through the junction at 10 mV and a bias voltage ~70 mV was enough to flow 21 nA current through the junction. The results shown here represent one microwire and were verified by repeating the experiment with two other microwires from different region of the growth substrate.

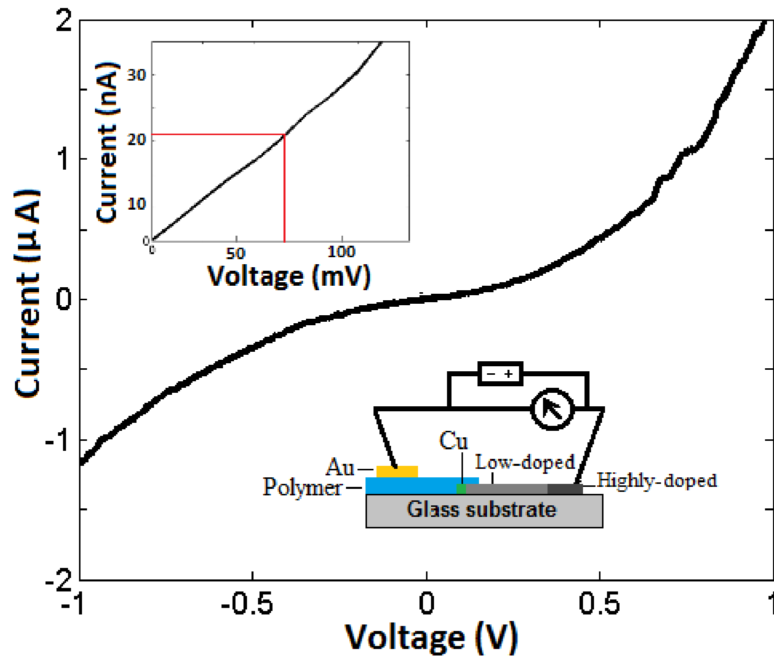

Figure 4.12: I-V characteristic for PEDOT:PSS/Cu/nn$^+$-Si microwires. The microwires with ~40 µm length and diameter of ~1 µm were 7-10 µm in contact with the conducting polymer from low-doped end including copper catalyst. The presence of copper yielded a symmetrical I-V curve for large bias voltage (< 1 V). It also showed a linear I-V profile with total resistance of 3.4 ± 0.7 MΩ for small bias regime (< 10 mV). The results shown here represent one microwire and were verified by repeating the experiment with other microwires from different region of the growth substrate.

4.1.2.4 PEDOT:PSS/Au/nn$^+$-Si Microwires

Au/nn$^+$-Si microwires had ~40µm long highly-doped base (n$^+$) with doping concentration of 4×10^{19} cm^{-3} and ~80µm long low-doped region (n) with doping concentration of 6×10^{18} cm^{-3} holding gold catalyst on the top (based on the fabrication process). Similarly to nn$^+$-Si microwires (Sec 4.1.2.1), the low-doped end (n) of Au/nn$^+$-Si microwires holding Au catalyst were identified; and 7-10 µm of the end were then inserted into the polymer film.

The presence of gold at the interface yielded a linear curve for large bias voltage < 1 V with total resistance R_{total} ~ 0.15 ± 0.04 MΩ for operational bias voltage < 10 mV (Fig 4.12). A very small bias voltage ~1 mV allowed 21 nA current to flow through the system. The results shown here represent one microwire and were verified by repeating the experiment with ten other microwires from different region of the growth substrate.

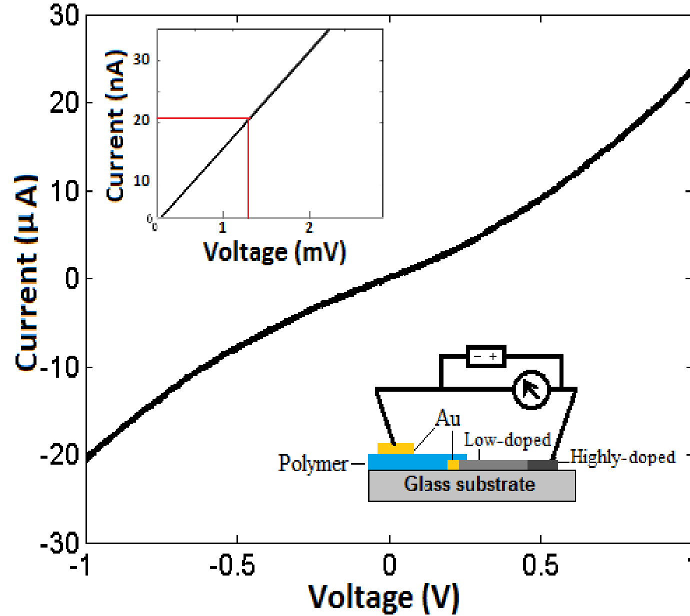

Figure 4.13: I-V characteristic for PEDOT:PSS/Au/nn$^+$-Si microwires. The microwires were ~120 µm in length and ~1 µm in diameter. They were 7-10 µm in contact with the conducting polymer from the low-doped end including gold catalyst. The presence of gold yielded a linear I-V profile for large bias regime (< 1 V) with a small total resistance of 0.15 ± 0.04 MΩ for small bias voltage (< 10 mV). The results shown here represent one microwire and were verified by repeating the experiment with other microwires from different region of the growth substrate.

4.1.2.5 PEDOT:PSS/modified n-Si Microwires

The resistance of the junction between methyl-terminated n-type silicon microwires, highly-doped (n$^+$) and highly-doped base (n$^+$n) microwires or metallic-capped microwire (n$^+$n-Au/Cu), and a conductive polymer membrane (PEDOT:PSS) were obtained by

making Ohmic contact to the microwires. The measured values for all combinations between PEDOT:PSS and proposed n-Si microwires, are summarized in Table 4.2.

Table 4.2: The total series resistance (R_{total}) and the current (I) at 10 mV for the combination of n-Si microwires and PEDOT:PSS with 7-10 μm of microwires embedded in the conductive polymer to the operational current. n is the doping concentration of carriers associated with the end of the microwires in contact with the polymer.

	Diameter (μm)	n (cm^{-3})	R_{total} (MΩ)	I (nA) at 10 mV
PEDOT:PSS/n^+-Si	1.5	~2×10^{20}	4 ± 1	10.1
PEDOT:PSS/n^+n-Si	1.5	~4×10^{19}	4.5 ± 0.3	1.73
PEDOT:PSS/nn^+-Si	1.5	~4×10^{18}	>20	4×10^{-3}
PEDOT:PSS/Cu/nn^+-Si	1.0	~4×10^{18}	3.4 ± 0.7	3
PEDOT:PSS/Au/nn^+-Si	1.0	~6×10^{18}	0.15 ± 0.04	~210

4.2 Discussion

Series resistance values of R_c, R_w, contributed in R_{total} of PEDOT:PSS/Si microwires system for small bias voltage (<10 mV) are found in Table 4.1. R_w < 9 kΩ and R_c < 0.5 kΩ are both 3 orders of magnitude less than R_{total}. R_p ~ 120 Ω (Sec 3.3) also represents a negligible contribution. Hence, R_{total} is a very good estimation of the microwire/polymer junction resistance, R_J (Table 4.2).

4.2.1 PEDOT:PSS/nn^+-Si

The PDOT:PSS/nn^+-Si represented a high resistance value > 20 MΩ to the junction and a very small leakage current ~ 4×10^{-3} nA flowed through the junction at 10 mV. The high junction resistance of > 20 MΩ was in agreement with the minimum attainable

junction resistance R_J > 20 MΩ at 21 nA [27] reported for methyl-terminated low doped n-Si microwires (10^{17}-10^{18} cm^{-3}) embedded in the conducting polymer. The results here implied that PEDOT:PSS produced Schottky (rectifying) contacts with large barrier heights on the low-doped end (n) of nn^+-Si. The behavior observed here was consistent with the expectation that the high work function ($q\phi_p \sim 5\ eV$) polymer, PEDOT:PSS, produces a large barrier heights $q\phi_b$~1.01 eV in contact with n-Si with $q\chi_s$ ~3.67 eV [29]. Under reverse bias, the Fermi energy of the polymer was raised with respect to the Fermi energy in the low doped silicon, yielding a larger depletion region, and therefore a pronounced rectifying behavior.

For a tunnelling current of 10 mV, the junction resistance and depletion layer width, obtained from the theoretical calculations (eq 2.4 for the depletion layer width, eq 2.8 for the tunneling current and eq 2.9 for junction resistance) and experiments are presented in Table (4.3). For the calculation, the planar junctions were assumed to have a contact area the same as PEDOT:PSS/n-Si microwires radial junctions (Sec 3.3); the relative permittivity was 11.68, the effective mass was $.98m_0$, the effective Richardson constant was 110 Acm^2-K^2, $q\phi_b$was 1.01 eV, and qV_a was 10 meV.

Table 4.3: The tunnelling current (*I*) at 10 mV, the junction resistance (R_J) and depletion layer width (*W*) obtained from the theoretical calculations and experiments for n^+n-Si microwires with 7-10 μm in contact with PEDOT:PSS. The microwires were ~60 μm length (~20 μm highly-doped and ~40 μm low-doped) and diameter of ~1.5 μm. In the case of calculations, the planar junctions were assumed to have a contact area the same as PEDOT:PSS/n-Si microwires radial junctions (Sec 3.3).

		W (nm)	*I* (nA)	R_J (MΩ)
PEDOT:PSS/nn^+-Si	Experiment	-	$\sim 4\times10^{-3}$	>20
PEDOT:PSS/n^+n-Si	Experiment	-	~1.7	~4.5
PEDOT:PSS/nn^+-Si	Theory	~15	$\sim 2.5\times 10^{-1}$	$\sim 5.5\times10^{5}$
PEDOT:PSS/n^+n-Si	Theory	~3	$\sim 8.2\times10^{3}$	~2.7

Theoretical calculation for a planar junction demonstrated that the raising doping density from ~4×10^{18} cm^{-3} to ~4×10^{19} cm^{-3} decreased the depletion region width to W~3 nm from W~15 nm (eq 2.4), and increased the tunneling current through the junction to I ~ 8.2 μA from I ~ 0.25 nA (eq 2.7), decreasing the junction resistances to R_J ~2.7 MΩ from R_J ~5.5×10^5 MΩ (eq 2.8). The thinner depletion layer width due to the high doping density made quantum mechanical tunnelling of carriers possible through the potential barrier and gave a reduction in the junction resistance.

The experiment results were quite consistent with trends in the theory, in comparison with PEDOT:PSS/nn$^+$-Si with I ~4×10^{-3} nA and R_J >20 MΩ, the PEDOT:PSS/n$^+$n-Si junction formed a narrower depletion region, and consequently increased the tunnelling current to ~4×10^{-2} nA at 10 mV and declined the junction resistance to ~ 4.5 MΩ.

In the table 4.3, R_J from theoretical calculations were significantly smaller than the experimental R_J and theoretically calculated I were also larger than the experimental I because the formulas used for calculation of I and R_J were for the planar structures and they were valid in large scales contact while the PEDOT:PSS/microwires junction were tested here had radial structures and the scale of the contacts were in the order of micrometers. When devices are miniaturized (Fig 4.13), the radius of the contacts (r) are significantly greater than the size of the conductors (L), r << L; the junction resistances cannot be simply obtained by $R_J = R/_A$, where R is the junction resistance per a unit of area and A is the contact area. In this case, a spreading resistance, R_{sp} should be added in series with junction resistances $R_J = R/_A + R_{sp}$ [30]. Therefore, smaller junction resistances and consequently larger current through the junctions were expected from theory than the experiments.

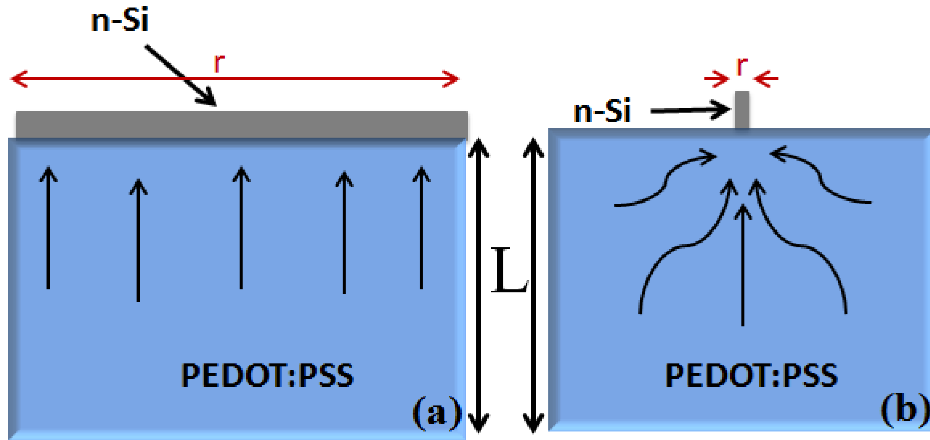

Figure 4.14: The current pattern in (a) a large contact area and (b) a small contact area when r<<L.

The formula used for the theoretical calculations are driven for Schottky contacts between metals and semiconductors. Although, PEDOT:PSS is a metallic like polymer and it is treated as a metal in the structures, it is naturally a polymer.

4.2.2 PEDOT:PSS/n$^+$-Si

Despite the highly rectifying nature of PEDOT:PSS/n-Si contacts, PEDOT:PSS films formed Ohmic tunnel-junction type contacts to n$^+$-Si microwires. The junction resistances obtained for n$^+$-Si microwires were significantly improved to 3-5 MΩ compared with respectively low-doped n-Si microwires (> 20 MΩ) and the current also increased to ~ 10.1 nA at 10 mV from ~ 4.2×10^{-11} A. The junction resistance, R_J ~ 3-5 MΩ, observed was in agreement with R_J ~ 0.5-4 Ω.cm^2 reported by Walter, *et al.*, using planar films [29].

I at 10 mV (eq 2.11), R_J (eq 2.12) and W (eq 2.4), obtained from the theoretical calculations and experiments are presented in Table (4.4). For the calculation, the planar junctions were assumed to have a contact area the same as PEDOT:PSS/n$^+$-Si microwires radial junctions (Sec 3.3); the relative permittivity was 11.68, the effective mass was

.98m$_o$, the effective Richardson constant was 110 Acm^2-K^2, $q\phi_b$ was 1.01 eV, and qV_a was 10 meV.

Table 4.4: The tunnelling current (I) at 10 mV, the junction resistance (R_J) and depletion layer width (W) obtained from the theoretical calculation and experiments for ~80 μm long n$^+$-Si microwires with doping distribution of ~2×10^{20} cm^{-3} with an average diameter of 1.5 μm. For the calculations, the planar junctions were assumed to have a contact area the same as PEDOT:PSS/n-Si microwires radial junctions (Sec 3.3).

		W (nm)	I (nA)	R_J(MΩ)
PEDOT:PSS/nn$^+$-Si	Experiment	-	~4×10^{-3}	>20
PEDOT:PSS/n$^+$Si	Experiment	-	~10.1	~4
PEDOT:PSS/nn$^+$-Si	Theory	15	2.5× 10^{-1}	5.5×10^5
PEDOT:PSS/n$^+$-Si	Theory	1	~10×10^5	0.6

Theoretical calculation for a planar junction demonstrated that the further increase in doping density to ~2×10^{20} cm^{-3} decreased W to ~3 nm from ~ 15 nm and consequently increased quantum mechanical tunnelling of carriers thought the potential barrier to I_T ~1 mA (at 10 mV), yielding a significant reduction in R_J to ~0.6 MΩ.

The junction behavior observed in this work was in accordance with trends in the theory; the degenerately doped n$^+$-Si microwires formed a narrow depletion region at the junction with the polymer and raised the number of electrons available for tunnelling through the junction. The thinner potential barrier and the high density of available electrons for tunnelling (two main factors of tunnelling current through a potential barrier) effectively facilitated tunnelling of carriers through the Schottky barrier at PEDOT:PSS/ n$^+$-Si junction, yielding an increase in I ~ 10.1 nA through the junction at 10 mV and an smaller junction resistance R_J~4 MΩ.

However, the measured junction resistance ~4 MΩ resistance is still significant compared with other reported junction resistances expected for solar water splitting

applications, demonstrating insufficient doping level to improve the junction resistance as much as is desired (R_J < 0.5 MΩ). However, this is still possible to increase the doping level of microwires up to ~10^{21} cm^{-3} [141]. Two order of magnitude reduction in the junction resistance (eq 2.12) is expected when the doping level elevates from ~ 10^{20} cm^{-3} to ~ 10^{21} cm^{-3} [30].

4.2.3 PEDOT:PSS/Cu/nn$^+$-Si

In comparison with PEDOT:PSS/nn$^+$-Si microwires (Sec 4.2.1), the presence of the copper at interface improved the total resistance R_J ~ 3.4 ± 0.7 MΩ of such a system for small bias voltage < 10 mV and the current also increased to ~ 3 nA at 10 mV.

The tunnelling current at 10 mV, the junction resistance and the barrier heights obtained from the theoretical calculations (eq 2.4 for $q\phi_b$, eq 2.8 for I and eq 2.9 for R_J) and experiments are presented in Table (4.5). For the calculations, the planar junctions were assumed to have a contact area the same as PEDOT:PSS/n-Si microwires radial junctions (Sec 3.3); the relative permittivity was 11.68, the effective mass was .98m0, the effective Richardson constant was 110 Acm^2-K^2, $q\phi_b$was 1.01 eV, and qV_a was 10 meV.

Table 4.5: The tunnelling current (I) at 10 mV, the junction resistance (R_J) and the barrier heights ($\boldsymbol{q\phi_b}$) obtained from the theoretical calculation and experiments for PEDOT:PSS/Cu/nn$^+$-Si microwires. The microwires were ~40 µm in length and ~1 µm diameter. The microwires were 7-10 µm in contact PEDOT:PSS from low-doped end with copper catalyst. For the calculations, the planar junctions were assumed to have a contact area the same as PEDOT:PSS/n-Si microwires radial junctions (Sec 3.3).

		$q\phi_b$ (eV)	I (nA)	R_J (MΩ)
PEDOT:PSS/nn$^+$-Si	Experiment	-	~4×10^{-3}	>20
PEDOT:PSS/Cu/nn$^+$-Si	Experiment	-	~3	~3.4
PEDOT:PSS/nn$^+$-Si	Theory	~15	~2.5×10^{-1}	~5.5×10^{5}
PEDOT:PSS/Cu/nn$^+$-Si	Theory	~1	~1.1×10^{4}	~0.9

A PEDOT:PSS/Cu/nn$^+$-Si consist two junctions in series, PEDOT:PSS/Cu and Cu/nn$^+$-Si. Highly conductive metal, Cu, in contact with the conductive polymer, PEDOT:PSS, forms an Ohmic junction. Deposition of copper with work function of ~ 4.7 eV on n-Si with $q\chi_s$~4.05 eV forms a Schottky barrier ~0.65 eV. The formation of a copper silicide layer at high temperature >800°C (T~1000°C according to the fabrication technique) reduces the Schottky barrier to ~0.59 eV [130]. Cu/n-Si junction with smaller barrier height (~0.59 eV) compared to with $q\phi_b$~1.01 eV resulting a significant tunneling current of ~11 μA at 10 mV and contact resistance of ~0.9 MΩ compared with PEDOT:PSS/nn$^+$-Si.

These expectations were consistent with the behavior observed herein for PEDOT:PSS/Cu/nn$^+$-Si, which were ohmic-like structure with significantly (orders of magnitude) smaller junction resistances ~ 3.4 ± 0.7 MΩ compared with PEDOT:PSS/n-Si (~4×10^{18} cm^{-3}).

It is important to note that both metallic-capped microwires had smaller diameters (~1 μm) compared with the rest of the microwires (~1.5 μm). The resistance of the junction is inversely proportional to contact area. Hence, an increase in the diameter of copper-capped microwires (~1.5 μm) is expected to make more improvement on PEDOT:PSS/Cu/nn$^+$-Si microwire junction resistance by a factor of ~1.5.

4.2.4 PEDOT:PSS/Au/nn$^+$-Si

The presence of the gold at the interface improved the junction resistance R_J ~ 0.15 MΩ of PEDOT:PSS/n-Si (~6×10^{18} cm^{-3}) for small bias voltage < 10 mV. A junction between

PEDOT:PSS and n-Si with gold interface comprises two junctions in series, PEDOT:PSS/Au and Au/n-Si. Au forms an Ohmic contact with the conductive polymer, PEDOT:PSS. Although deposition of gold with work function of ~ 5.2 eV on n-Si with $q\chi_s$~4.05 eV should produce a Schottky barrier ~0.7 eV and consequently a rectifying behavior, the formation of gold silicide at high temperature >350°C (T~1000°C according to microwires growth technique) makes an Ohmic contact between Au/n-Si. These expectations were in accordance with the behavior observed in this work, the presence of the gold interface at PEDOT:PSS/n-Si demonstrated Ohmic behavior with very small junction resistance R_J ~ 0.15 MΩ. In comparison with the gold interfacial layer at the junction, copper exhibited a nonlinear I-V curve with larger junction resistance because gold silicide makes almost a zero Schottky barrier at the junction with n-Si, while copper silicide makes a 0.56 eV high Schottky junction with n-Si [130, 142]. An increase in the diameter of gold-capped microwires (~1.5 µm) is expected to reduce the junction resistance of PEDOT:PSS/Au/nn^+-Si by a factor of ~1.5.

Chapter Five

Conclusions and Future Directions

5.1 Conclusions

To minimize the electrical losses in the solar water splitting devices, the polymer/Si microwire junction resistances < 0.5 MΩ yield losses that were 1% of total photogenerated voltage required for water splitting. This thesis has presented further evidence that raising the doping density of n-Si microwires in contact with PEDOT:PSS or addition of a metallic interfacial layer at PEDOT:PSS/n-Si microwires may offer a compelling route toward an improvement in electrical behavior of the junction between PEDOT:PSS and methyl-terminated n-Si microwires. This thesis has experimentally verified the elevation of doping density on the order of 10^{19}-10^{20} cm^{-3} exhibited a significant improvement in junction resistance of PEDOT:PSS/n-Si microwires relative to low doped n-Si microwires. However, the junction resistance for highly doped n-Si microwires (10^{19} -10^{20} cm^{-3}) is still about an order of magnitude larger than the resistance (R ~ 0.5 MΩ) expected to minimize the impact of IR losses in a functional system. It also has shown that the methyl-terminated n-type Si microwires (4×10^{18} cm^{-3}) in contact with

PEDOT:PSS with copper interface reduce the junction resistance of PEDOT:PSS/n-Si and have similar current-voltage characteristics to those observed for the highly-doped microwires, while junctions incorporating gold exhibited ohmic behavior and significantly lower resistances ~ 0.15 MΩ. Hence, PEDOT:PSS provides a potentially Ohmic contact with methyl-terminated n-Si microwires through increase of the doping and addition of copper and gold; among all the combinations, the PEDOT:PSS/n-Si junction with gold interfacial layer demonstrated an ohmic contact with sufficiently small junction resistance which met the minimum requirements for contact resistance of PEDOT:PSS/n-Si in the solar water splitting device applications.

5.2 Future Directions

There are several pathways as potential future work for examining and characterization of water splitting structures. Raising the doping concentration of the microwires ($\sim 10^{20}$ cm^{-3}) demonstrated a significant improvement in the junction resistance. It is possible to raise the doping level one order of magnitude ($\sim 10^{21}$ cm^{-3}) according to the solid-solubility limit of n-type dopants in silicon $\sim 10^{21}$ cm^{-3}. It has been shown that when doping level elevates from ~ 10^{20} cm^{-3} to ~ 10^{21} cm^{-3}, the junction resistance reduces one or two orders of magnitude [30] and consequently, acceptable improvement in junction resistance of such a system would be expected from significantly high doping of microwires ($\sim 10^{21}$ cm^{-3}). Hence, the effect of higher doping concentration (~ 10^{21} cm^{-3}) for n-Si microwires in contact with the polymer could be investigated as a potential future work. For the purpose of this study, heavily-doped n-Si microwires ~ 10^{21} cm^{-3} can be

possibly grown by increasing the concentration of PH_3 in the growth chamber concentration with either raising PH_3 flow or decreasing the H_2 flow.

This work demonstrated that addition of a metal interfacial layer at the junction of PEDOT:PSS/n-Si is a promising approach to address the large junction resistance, specially, the structures with gold interfacial layer; the junction resistance of PEDOT:PSS/Au/n-Si was less than (~10%) the critical value for the junction resistance in proposed structure of solar water splitting devices. However, the main purpose of a solar water splitting device is having a viable renewable energy system using earth abundant materials, but gold is not an abundant material, suggesting expensive large-scale production. Hence, the nature of PEDOT:PSS/n-Si junction with contribution of other metallic interfacial layers can be explored using the ohmic contact formation to the structures with W probes. Ni, Al, Ag, Bi, Cd, Co Dy, Fe, Ga, Gd, In, Mg, Mn, Os, Pb, Pd, Pr, Pt, Ru, Sn, Te, Ti, and Zn are the metallic catalysts have been reported in Si microwire array fabrication [99]; among them obviously Ni, Fe, Ga, In and Mg are in priority since they are more abundant and resistive to oxidation compared to the rest. The Schottky barrier heights at the junction between the candidate metallic silicides and n-Si is also another important parameter that should be considered in order to choose a proper metallic interfacial layer.

References

1. Haman, T. and K. Jumah, *Organic Solar Cells Based on High Dielectric Constant Materials: An Approach to Increase Efficiency*. 2013.
2. Lewis, N.S. and G. Crabtree, *Basic Research Needs for Solar Energy Utilization: report of the Basic Energy Sciences Workshop on Solar Energy Utilization, April 18-21, 2005.* 2005.
3. Würfel, P. and U. Würfel, *Physics of Solar Cells: From Basic Principles to Advanced Concepts*. 2009: John Wiley & Sons.
4. Kalogirou, S.A., *Solar thermal collectors and applications.* Progress in energy and combustion science, 2004. **30**(3): p. 231-295.
5. Mills, D., *Advances in solar thermal electricity technology.* Solar Energy, 2004. **76**(1): p. 19-31.
6. Matthews, H.S., G. Cicas, and J.L. Aguirre, *Economic and environmental evaluation of residential fixed solar photovoltaic systems in the United States.* Journal of infrastructure systems, 2004. **10**(3): p. 105-110.
7. Glavin, M. and W. Hurley. *Battery management system for solar energy applications*. in *Universities Power Engineering Conference, 2006. UPEC'06. Proceedings of the 41st International*. 2006: IEEE.
8. Yilanci, A., I. Dincer, and H. Ozturk, *A review on solar-hydrogen/fuel cell hybrid energy systems for stationary applications.* Progress in energy and combustion science, 2009. **35**(3): p. 231-244.

9. Lewis, N.S., *Light work with water.* Nature, 2001. **414**(6864): p. 589-590.
10. Fujishima, A., *Electrochemical photolysis of water at a semiconductor electrode.* Nature, 1972. **238**: p. 37-38.
11. Graetz, J., *New approaches to hydrogen storage.* Chemical Society Reviews, 2009. **38**(1): p. 73-82.
12. Yoon, J.H., J. Hae Shin, M.-S. Kim, S. Jun Sim, and T.H. Park, *Evaluation of conversion efficiency of light to hydrogen energy by< i> Anabaena variabilis</i>.* International journal of hydrogen energy, 2006. **31**(6): p. 721-727.
13. Schlapbach, L. and A. Züttel, *Hydrogen-storage materials for mobile applications.* nature, 2001. **414**(6861): p. 353-358.
14. White, C., R. Steeper, and A. Lutz, *The hydrogen-fueled internal combustion engine: a technical review.* International journal of hydrogen energy, 2006. **31**(10): p. 1292-1305.
15. Eichlseder, H., T. Wallner, R. Freymann, and J. Ringler, *The potential of hydrogen internal combustion engines in a future mobility scenario.* Diesel Engine, 2003. **2013**: p. 04-08.
16. Heck, R.M., H.-S. Hwang, and R.M. Yarrington, *Fuel cell electric power production*. 1985, Google Patents.
17. Bolton, J.R., S.J. Strickler, and J.S. Connolly, *Limiting and realizable efficiencies of solar photolysis of water.* Nature, 1985. **316**(6028): p. 495-500.
18. Bolton, J.R., *Solar photoproduction of hydrogen: A review.* Solar Energy, 1996. **57**(1): p. 37-50.
19. Turner, J.A., *A realizable renewable energy future.* Science, 1999. **285**(5428): p. 687-689.
20. Lewis, N.S. and D.G. Nocera, *Powering the planet: Chemical challenges in solar energy utilization.* Proceedings of the National Academy of Sciences, 2006. **103**(43): p. 15729-15735.
21. Bard, A.J. and M.A. Fox, *Artificial photosynthesis: solar splitting of water to hydrogen and oxygen.* Accounts of Chemical Research, 1995. **28**(3): p. 141-145.
22. Lewis, N.S., *Powering the planet.* MRS bulletin, 2007. **32**(10): p. 808-820.
23. Gray, H.B., *Powering the planet with solar fuel.* Nat Chem, 2009. **1**(1): p. 7-7.
24. Walter, M.G., E.L. Warren, J.R. McKone, S.W. Boettcher, Q. Mi, E.A. Santori, and N.S. Lewis, *Solar Water Splitting Cells.* Chemical Reviews, 2010. **110**(11): p. 6446-6473.

25. McFarlane, S.L., B.A. Day, K. McEleney, M.S. Freund, and N.S. Lewis, *Designing electronic/ionic conducting membranes for artificial photosynthesis.* Energy & Environmental Science, 2011. **4**(5): p. 1700-1703.

26. Yahyaie, I., K. McEleney, M.G. Walter, D.R. Oliver, D.J. Thomson, M.S. Freund, and N.S. Lewis, *Electrical characterization of Si microwires and of Si microwire/conducting polymer composite junctions.* The Journal of Physical Chemistry Letters, 2011. **2**(6): p. 675-680.

27. Yahyaie, I., S. Ardo, D.R. Oliver, D.J. Thomson, M.S. Freund, and N.S. Lewis, *Comparison between the electrical junction properties of H-terminated and methyl-terminated individual Si microwire/polymer assemblies for photoelectrochemical fuel production.* Energy Environ. Sci., 2012. **5**(12): p. 9789-9794.

28. Yahyaie, I., *Electrical Characterization of Microwire-Polymer Assemblies for Solar Water Splitting Applications.* Ph.D Thesis, Dept. Electrical Engineering and Computer Science, University of Manitoba, Winnipeg, Manitoba,, 2012: p. 47-48.

29. Walter, M.G., X. Liu, L.E. O'Leary, B.S. Brunschwig, and N.S. Lewis, *The Electrical Junction Behavior of Poly (3, 4-ethylenedioxythiophene)(PEDOT) Contacts to H-Terminated and CH3-Terminated p-, n-and n+-Si (111) Surfaces.* The Journal of Physical Chemistry C, 2013. **117**(28): p. 14485-14492.

30. Sze, S.M. and K.K. Ng, *Physics of semiconductor devices*. Hand Book. 2006: Wiley-interscience.

31. Fujishima, A. and K. Honda, *Electrochemical Evidence for the Mechanism of the Primary Stage of Photosynthesis.* NOTES, 1971. **44**(4): p. 148-150.

32. Bak, T., J. Nowotny, M. Rekas, and C.C. Sorrell, *Photo-electrochemical hydrogen generation from water using solar energy. Materials-related aspects.* International journal of hydrogen energy, 2002. **27**(10): p. 991-1022.

33. Osterloh, F.E. and B.A. Parkinson, *Recent developments in solar water-splitting photocatalysis.* MRS bulletin, 2011. **36**(1): p. 17-22.

34. Wolf, M., *Limitations and possibilities for improvement of photovoltaic solar energy converters: part I: considerations for earth's surface operation.* Proceedings of the IRE, 1960. **48**(7): p. 1246-1263.

35. Yum, J.-H., E. Baranoff, S. Wenger, M.K. Nazeeruddin, and M. Grätzel, *Panchromatic engineering for dye-sensitized solar cells.* Energy & Environmental Science, 2011. **4**(3): p. 842-857.

36. Shockley, W. and H.J. Queisser, *Detailed balance limit of efficiency of p-n junction solar cells.* Journal of Applied Physics, 1961. **32**(3): p. 510-519.

37. Olson, K.D. and J.J. Talghader, *Absorption to reflection transition in selective solar coatings.* Optics express, 2012. **20**(104): p. A554-A559.

38. Licht, S., B. Wang, S. Mukerji, T. Soga, M. Umeno, and H. Tributsch, *Efficient Solar Water Splitting, Exemplified by RuO2-Catalyzed AlGaAs/Si Photoelectrolysis.* The Journal of Physical Chemistry B, 2000. **104**(38): p. 8920-8924.

39. Yu, G., G. Srdanov, J. Wang, H. Wang, Y. Cao, and A.J. Heeger, *Large area, full-color, digital image sensors made with semiconducting polymers.* Synthetic metals, 2000. **111**: p. 133-137.

40. Licht, S., *Multiple band gap semiconductor/electrolyte solar energy conversion.* The Journal of Physical Chemistry B, 2001. **105**(27): p. 6281-6294.

41. Marti, A. and G.L. Araújo, *Limiting efficiencies for photovoltaic energy conversion in multigap systems.* Solar Energy Materials and Solar Cells, 1996. **43**(2): p. 203-222.

42. Nozik, A., *Photochemical diodes.* Applied Physics Letters, 1977. **30**(11): p. 567-569.

43. Kayes, B.M., H.A. Atwater, and N.S. Lewis, *Comparison of the device physics principles of planar and radial pin junction nanorod solar cells.* Journal of Applied Physics, 2005. **97**(11): p. 114302-114302-11.

44. Kayes, B.M., M.A. Filler, M.C. Putnam, M.D. Kelzenberg, N.S. Lewis, and H.A. Atwater, *Growth of vertically aligned Si wire arrays over large areas (≫ 1 cm2) with Au and Cu catalysts.* Applied Physics Letters, 2007. **91**(10): p. 103110-103110-3.

45. Ciszek, T. *Silicon material quality and throughput: the high and the low, the fast and the slow*. in *Photovoltaic Specialists Conference, 1988., Conference Record of the Twentieth IEEE*. 1988: IEEE.

46. Vallat-Sauvain, E., A. Shah, and J. Bailat, *Advances in microcrystalline silicon solar cell technologies.* Thin Film Solar Cells: Fabrication, Characterization, and Application, 2006. **1**: p. 133-171.

47. Gordon, R.B., M. Bertram, and T. Graedel, *Metal stocks and sustainability.* Proceedings of the National Academy of Sciences of the United States of America, 2006. **103**(5): p. 1209-1214.

48. Mettee, H., J.W. Otvos, and M. Calvin, *Solar induced water splitting with p/n heterotype photochemical diodes: n-Fe< sub> 2</sub> O< sub> 3</sub>/p-GaP*. Solar Energy Materials, 1981. **4**(4): p. 443-453.

49. Butler, M. and D. Ginley, *P-Type GaP as a Semiconducting Photoelectrode.* Journal of The Electrochemical Society, 1980. **127**(6): p. 1273-1278.
50. Bockris, J.M. and K. Uosaki, *The Stability of Photoelectrodes.* Journal of The Electrochemical Society, 1977. **124**(1): p. 98-99.
51. Grätzel, M., *Photoelectrochemical cells.* Nature, 2001. **414**(6861): p. 338-344.
52. Johnston, W., H. Leamy, B. Parkinson, A. Heller, and B. Miller, *Effect of ruthenium ions on grain boundaries in gallium arsenide thin film photovoltaic devices.* Journal of The Electrochemical Society, 1980. **127**(1): p. 90-95.
53. Heller, A., *Conversion of sunlight into electrical power and photoassisted electrolysis of water in photoelectrochemical cells.* Accounts of Chemical Research, 1981. **14**(5): p. 154-162.
54. Dare-Edwards, M., J. Goodenough, A. Hamnett, and N. Nicholson, *Photoelectrochemistry of nickel (II) oxide.* Journal of the Chemical Society, Faraday Transactions 2: Molecular and Chemical Physics, 1981. **77**(4): p. 643-661.
55. Rajeshwar, K., P. Singh, and J. DuBow, *Energy conversion in photoelectrochemical systems—a review.* Electrochimica Acta, 1978. **23**(11): p. 1117-1144.
56. Rajeshwar, K., *Materials aspects of photoelectrochemical energy conversion.* Journal of applied electrochemistry, 1985. **15**(1): p. 1-22.
57. Belhadi, A., S. Boumaza, and M. Trari, *Photoassisted hydrogen production under visible light over NiO/ZnO hetero-system.* Applied Energy, 2011. **88**(12): p. 4490-4495.
58. Koffyberg, F. and F. Benko, *A photoelectrochemical determination of the position of the conduction and valence band edges of p-type CuO.* Journal of Applied Physics, 1982. **53**(2): p. 1173-1177.
59. Gerritsen, H., W. Ruppel, and P. Würfel, *A Photoelectrochemical Storage Cell with n-CdSe and p-CdTe Electrodes.* Journal of The Electrochemical Society, 1984. **131**(9): p. 2037-2041.
60. Shah, A., P. Torres, R. Tscharner, N. Wyrsch, and H. Keppner, *Photovoltaic technology: the case for thin-film solar cells.* Science, 1999. **285**(5428): p. 692-698.
61. Brendel, R., *Thin-film crystalline silicon solar cells: physics and technology*. Hand Book. 2011: John Wiley & Sons.
62. Royea, W.J., A. Juang, and N.S. Lewis, *Preparation of air-stable, low recombination velocity Si (111) surfaces through alkyl termination.* Applied Physics Letters, 2000. **77**(13): p. 1988-1990.

63. Eades, W.D. and R.M. Swanson, *Calculation of surface generation and recombination velocities at the Si-SiO2 interface.* Journal of Applied Physics, 1985. **58**(11): p. 4267-4276.

64. Baek, D., S. Rouvimov, B. Kim, T.-C. Jo, and D. Schroder, *Surface recombination velocity of silicon wafers by photoluminescence.* Applied Physics Letters, 2005. **86**(11): p. 112110.

65. Bent, S.F., *Organic functionalization of group IV semiconductor surfaces: principles, examples, applications, and prospects.* Surface Science, 2002. **500**(1): p. 879-903.

66. Nemanick, E.J., P.T. Hurley, B.S. Brunschwig, and N.S. Lewis, *Chemical and electrical passivation of silicon (111) surfaces through functionalization with sterically hindered alkyl groups.* The Journal of Physical Chemistry B, 2006. **110**(30): p. 14800-14808.

67. Mitchell, S., R. Boukherroub, and S. Anderson, *Second harmonic generation at chemically modified Si (111) surfaces.* The Journal of Physical Chemistry B, 2000. **104**(32): p. 7668-7676.

68. Webb, L.J., E.J. Nemanick, J.S. Biteen, D.W. Knapp, D.J. Michalak, M.C. Traub, A.S. Chan, B.S. Brunschwig, and N.S. Lewis, *High-resolution X-ray photoelectron spectroscopic studies of alkylated silicon (111) surfaces.* The Journal of Physical Chemistry B, 2005. **109**(9): p. 3930-3937.

69. Bansal, A. and N.S. Lewis, *Stabilization of Si photoanodes in aqueous electrolytes through surface alkylation.* The Journal of Physical Chemistry B, 1998. **102**(21): p. 4058-4060.

70. Linford, M.R., P. Fenter, P.M. Eisenberger, and C.E. Chidsey, *Alkyl monolayers on silicon prepared from 1-alkenes and hydrogen-terminated silicon.* Journal of the American Chemical Society, 1995. **117**(11): p. 3145-3155.

71. Boukherroub, R. and D.D. Wayner, *Controlled Functionalization and Multistep Chemical Manipulation of Covalently Modified Si (111) Surfaces1.* Journal of the American Chemical Society, 1999. **121**(49): p. 11513-11515.

72. Terry, J., M.R. Linford, C. Wigren, R. Cao, P. Pianetta, and C.E. Chidsey, *Determination of the bonding of alkyl monolayers to the Si (111) surface using chemical-shift, scanned-energy photoelectron diffraction.* Applied Physics Letters, 1997. **71**(8): p. 1056-1058.

73. Boukherroub, R., J. Wojtyk, D.D. Wayner, and D.J. Lockwood, *Thermal hydrosilylation of undecylenic acid with porous silicon.* Journal of The Electrochemical Society, 2002. **149**(2): p. H59-H63.

74. Sung, M.M., G.J. Kluth, O.W. Yauw, and R. Maboudian, *Thermal behavior of alkyl monolayers on silicon surfaces.* Langmuir, 1997. **13**(23): p. 6164-6168.

75. Zazzera, L., J. Evans, M. Deruelle, M. Tirrell, C. Kessel, and P. McKeown, *Bonding Organic Molecules to Hydrogen-Terminated Silicon Wafers.* Journal of The Electrochemical Society, 1997. **144**(6): p. 2184-2189.

76. Buriak, J.M., M.P. Stewart, T.W. Geders, M.J. Allen, H.C. Choi, J. Smith, D. Raftery, and L.T. Canham, *Lewis acid mediated hydrosilylation on porous silicon surfaces.* Journal of the American Chemical Society, 1999. **121**(49): p. 11491-11502.

77. Bansal, A. and N.S. Lewis, *Electrochemical properties of (111)-oriented n-Si surfaces derivatized with covalently-attached alkyl chains.* The Journal of Physical Chemistry B, 1998. **102**(7): p. 1067-1070.

78. Webb, L.J. and N.S. Lewis, *Comparison of the electrical properties and chemical stability of crystalline silicon (111) surfaces alkylated using grignard reagents or olefins with Lewis acid catalysts.* The Journal of Physical Chemistry B, 2003. **107**(23): p. 5404-5412.

79. Johansson, E., S.W. Boettcher, L.E. O'Leary, A.D. Poletayev, S. Maldonado, B.S. Brunschwig, and N.S. Lewis, *Control of the pH-Dependence of the Band Edges of Si (111) Surfaces Using Mixed Methyl/Allyl Monolayers.* The Journal of Physical Chemistry C, 2011. **115**(17): p. 8594-8601.

80. Fujishima, A., T.N. Rao, and D.A. Tryk, *Titanium dioxide photocatalysis.* Journal of Photochemistry and Photobiology C: Photochemistry Reviews, 2000. **1**(1): p. 1-21.

81. Kelzenberg, M.D., S.W. Boettcher, J.A. Petykiewicz, D.B. Turner-Evans, M.C. Putnam, E.L. Warren, J.M. Spurgeon, R.M. Briggs, N.S. Lewis, and H.A. Atwater, *Enhanced absorption and carrier collection in Si wire arrays for photovoltaic applications.* Nature materials, 2010. **9**(3): p. 239-244.

82. Maiolo, J.R., H.A. Atwater, and N.S. Lewis, *Macroporous silicon as a model for silicon wire array solar cells.* The Journal of Physical Chemistry C, 2008. **112**(15): p. 6194-6201.

83. Kayes, B.M., M.A. Filler, M.C. Putnam, M.D. Kelzenberg, N.S. Lewis, and H.A. Atwater, *Growth of vertically aligned Si wire arrays over large areas (>>1 cm2) with Au and Cu catalysts.* Applied Physics Letters, 2007. **91**(10): p. 103110-103110-3.

84. Wagner, D. and A. Jayatissa, *Nanoimprint lithography: Review of aspects and applications.* Nanofabrication: Technologies, Devices, and Applications II, 2005. **6002**: p. 60020R.

85. Rothschild, M., A.R. Forte, M.W. Horn, R.R. Kunz, S.C. Palmateer, and J.H. Sedlacek. *193-nm lithography (Review Paper)*. in *Photonics West'96*. 1996: International Society for Optics and Photonics.
86. Zhang, R.Q., Y. Lifshitz, and S.T. Lee, *Oxide-Assisted Growth of Semiconducting Nanowires.* Advanced Materials, 2003. **15**(7-8): p. 635-640.
87. Wang, Y., V. Schmidt, S. Senz, and U. Gösele, *Epitaxial growth of silicon nanowires using an aluminium catalyst.* Nature nanotechnology, 2006. **1**(3): p. 186-189.
88. Huang, Y., X. Duan, Q. Wei, and C.M. Lieber, *Directed assembly of one-dimensional nanostructures into functional networks.* Science, 2001. **291**(5504): p. 630-633.
89. Wagner, R.S. and W.C. Ellis, *Vapor-liquid-solid mechanism of single crystal growth.* Applied Physics Letters, 1964. **4**(5): p. 89-90.
90. Kelzenberg, M.D., D.B. Turner-Evans, M.C. Putnam, S.W. Boettcher, R.M. Briggs, J.Y. Baek, N.S. Lewis, and H.A. Atwater, *High-performance Si microwire photovoltaics.* Energy & Environmental Science, 2011. **4**(3): p. 866-871.
91. Wagner, R., *Defects in silicon crystals grown by the VLS technique.* Journal of Applied Physics, 2004. **38**(4): p. 1554-1560.
92. Wagner, R. and W. Ellis, *Vapor-liquid-solid mechanism of crystal growth and its application to silicon*. Hand Book. 1965: Bell Telephone Laboratories.
93. Wagner, R. and C. Doherty, *Controlled Vapor-Liquid-Solid Growth of Silicon Crystals.* Journal of The Electrochemical Society, 1966. **113**(12): p. 1300-1305.
94. Cui, Y., L.J. Lauhon, M.S. Gudiksen, J. Wang, and C.M. Lieber, *Diameter-controlled synthesis of single-crystal silicon nanowires.* Applied Physics Letters, 2001. **78**(15): p. 2214-2216.
95. Schmidt, V., J. Wittemann, and U. Gosele, *Growth, thermodynamics, and electrical properties of silicon nanowires†.* Chemical reviews, 2010. **110**(1): p. 361-388.
96. Schmidt, V., J.V. Wittemann, S. Senz, and U. Gösele, *Silicon nanowires: a review on aspects of their growth and their electrical properties.* Advanced Materials, 2009. **21**(25-26): p. 2681-2702.
97. Hochbaum, A.I., R. Fan, R. He, and P. Yang, *Controlled growth of Si nanowire arrays for device integration.* Nano letters, 2005. **5**(3): p. 457-460.
98. Kelzenberg, M., *Silicon Microwire Photovoltaics.* Ph.D Thesis, Dept. Chemistry,California Institute of Technology, Pasadena, California, 2010: p. 98-129.

99. Warren, E.L., *Silicon microwire arrays for photoelectrochemical and photovoltaic applications*, in *Ph.D Thesis, Dept. Chemistry,California Institute of Technology, Pasadena, California*. 2013, 12-17.

100. Kayes, B.M. *Radial pn junction, wire array solar cells*. 2009: Ph.D Thesis, Dept. Chemistry,California Institute of Technology, Pasadena, California.

101. Boettcher, S.W., E.L. Warren, M.C. Putnam, E.A. Santori, D.B. Turner-Evans, M.D. Kelzenberg, M.G. Walter, J.R. McKone, B.S. Brunschwig, and H.A. Atwater, *Photoelectrochemical hydrogen evolution using Si microwire arrays.* Journal of the American Chemical Society, 2011. **133**(5): p. 1216-1219.

102. Spurgeon, J.M., K.E. Plass, B.M. Kayes, B.S. Brunschwig, H.A. Atwater, and N.S. Lewis, *Repeated epitaxial growth and transfer of arrays of patterned, vertically aligned, crystalline Si wires from a single Si (111) substrate.* Applied Physics Letters, 2008. **93**(3): p. 032112-032112-3.

103. Groenendaal, L., F. Jonas, D. Freitag, H. Pielartzik, and J.R. Reynolds, *Poly (3, 4-ethylenedioxythiophene) and its derivatives: past, present, and future.* Advanced materials, 2000. **12**(7): p. 481-494.

104. Zotti, G., S. Zecchin, G. Schiavon, F. Louwet, L. Groenendaal, X. Crispin, W. Osikowicz, W. Salaneck, and M. Fahlman, *Electrochemical and XPS studies toward the role of monomeric and polymeric sulfonate counterions in the synthesis, composition, and properties of poly (3, 4-ethylenedioxythiophene).* Macromolecules, 2003. **36**(9): p. 3337-3344.

105. Winder, C. and N.S. Sariciftci, *Low bandgap polymers for photon harvesting in bulk heterojunction solar cells.* Journal of Materials Chemistry, 2004. **14**(7): p. 1077-1086.

106. Nardes, A.M., M. Kemerink, M.M. De Kok, E. Vinken, K. Maturova, and R.A.J. Janssen, *Conductivity, work function, and environmental stability of PEDOT: PSS thin films treated with sorbitol.* Organic Electronics, 2008. **9**(5): p. 727-734.

107. Li, G. and P.G. Pickup, *Ion transport in poly (3, 4-ethylenedioxythiophene)-poly (styrene-4-sulfonate) composites.* Physical Chemistry Chemical Physics, 2000. **2**(6): p. 1255-1260.

108. Jonas, F., W. Krafft, and B. Muys. *Poly (3, 4- ethylenedioxythiophene): Conductive coatings, technical applications and properties*. in *Macromolecular Symposia*. 1995: Wiley Online Library.

109. Elschner, A., S. Kirchmeyer, W. Lovenich, U. Merker, and K. Reuter, *PEDOT: principles and applications of an intrinsically conductive polymer*. 2010: CRC Press.

110. Yahyaie, I., K. McEleney, M.G. Walter, D.R. Oliver, D.J. Thomson, M.S. Freund, and N.S. Lewis, *Characterization of the electrical properties of individual p-Si microwire/polymer/n-Si microwire assemblies.* The Journal of Physical Chemistry C, 2011. **115**(50): p. 24945-24950.

111. Grimm, R.L., M.J. Bierman, L.E. O'Leary, N.C. Strandwitz, B.S. Brunschwig, and N.S. Lewis, *Comparison of the Photoelectrochemical Behavior of H-Terminated and Methyl-Terminated Si (111) Surfaces in Contact with a Series of One-Electron, Outer-Sphere Redox Couples in CH3CN.* The Journal of Physical Chemistry C, 2012. **116**(44): p. 23569-23576.

112. Chand, S. and J. Kumar, *Effects of barrier height distribution on the behavior of a Schottky diode.* Journal of Applied Physics, 1997. **82**(10): p. 5005-5010.

113. Werner, J.H. and H.H. Guttler, *Barrier inhomogeneities at Schottky contacts.* Journal of Applied Physics, 1991. **69**: p. 1522.

114. Inganas, O., T. Skotheim, and I. Lundstrom, *Schottky barrier formation between polypyrrole and crystalline and amorphous hydrogenated silicon.* Physica Scripta, 1982. **25**(6A): p. 863.

115. Rhoderick, E.H. and R.H. Williams, *Metal-semiconductor contacts*. Vol. 129. 1988: IEE Proceedings I (Solid-State and Electron Devices).

116. Schmidt, P.H., S.R. Forrest, and M.L. Kaplan, *Organic- Inorganic Contact Barrier Heights A Survey of Materials.* Journal of The Electrochemical Society, 1986. **133**(4): p. 769-771.

117. Frank, A.J., S. Glenis, and A.J. Nelson, *Conductive polymer-semiconductor junction: characterization of poly (3-methylthiophene): Cadmium sulfide based photoelectrochemical and photovoltaic cells.* The Journal of Physical Chemistry, 1989. **93**(9): p. 3818-3825.

118. Koezuka, H. and S. Etoh, *Schottky barrier type diode with an electrochemically prepared copolymer having pyrrole and N-methylpyrrole units.* Journal of Applied Physics, 1983. **54**(5): p. 2511-2516.

119. Salaneck, W.R., S. Stafstrom, and J.L. Bredas, *Conjugated polymer surfaces and interfaces: electronic and chemical structure of interfaces for polymer light emitting devices*. 2003: Cambridge University Press.

120. Brammer, T. and H. Stiebig, *Defect density and recombination lifetime in microcrystalline silicon absorbers of highly efficient thin-film solar cells determined by numerical device simulations.* Journal of Applied Physics, 2003. **94**(2): p. 1035-1042.

121. Landsberg, P.T. and G.S. Kousik, *The connection between carrier lifetime and doping density in nondegenerate semiconductors.* Journal of Applied Physics, 1984. **56**(6): p. 1696-1700.
122. Cuevas, A. and D. Macdonald, *Measuring and interpreting the lifetime of silicon wafers.* Solar Energy, 2004. **76**(1): p. 255-262.
123. Wu, C.Y., *Interfacial layer theory of the Schottky barrier diodes.* Journal of Applied Physics, 2008. **51**(7): p. 3786-3789.
124. Liu, B., E. Lambers, W. Alexander, and P. Holloway, *Effects of a Ni cap layer on transparent Ni/Au ohmic contacts to p-GaN.* Journal of Vacuum Science & Technology B: Microelectronics and Nanometer Structures, 2002. **20**(4): p. 1394-1401.
125. Ohring, M., *Reliability and failure of electronic materials and devices*. Hand Book. 1998: Academic Press.
126. Chen, L.J., *Silicide Technology for Integrated Circuits (Processing)*. Vol. 5. 2004: Iet.
127. Huang, Y. and K.-n. Tu, *Silicon and Silicide Nanowires: Applications, Fabrication, and Properties*. Hand Book. 2013: CRC Press.
128. Gambino, J. and E. Colgan, *Silicides and ohmic contacts.* Materials Chemistry and Physics, 1998. **52**(2): p. 99-146.
129. Istratov, A. and E. Weber, *Electrical properties and recombination activity of copper, nickel and cobalt in silicon.* Applied physics A, 1998. **66**(2): p. 123-136.
130. Aboelfotoh, M., A. Cros, B. Svensson, and K. Tu, *Schottky-barrier behavior of copper and copper silicide on n-type and p-type silicon.* Physical Review B, 1990. **41**(14): p. 9819.
131. Maeda, K. and E. Kitahara, *Metal-induced gap states model of nonideal Au/Si Schottky barrier with low defect density.* Applied surface science, 1998. **130**: p. 925-929.
132. Young, T., J. Chang, and H. Ueng, *Study on annealing effects of Au thin films on Si.* Thin Solid Films, 1998. **322**(1): p. 319-322.
133. Hiraki, A., E. Lugujjo, and J.W. Mayer, *Formation of silicon oxide over gold layers on silicon substrates.* Journal of Applied Physics, 2003. **43**(9): p. 3643-3649.
134. Green, M.A., K. Emery, Y. Hishikawa, W. Warta, and E.D. Dunlop, *Solar cell efficiency tables (version 39).* Progress in photovoltaics: research and applications, 2012. **20**(1): p. 12-20.
135. Boettcher, S.W., J.M. Spurgeon, M.C. Putnam, E.L. Warren, D.B. Turner-Evans, M.D. Kelzenberg, J.R. Maiolo, H.A. Atwater, and N.S. Lewis, *Energy-Conversion Properties*

of Vapor-Liquid-Solid Grown Silicon Wire-Array Photocathodes. Science, 2007. **327**(5962): p. 185-187.

136. Maiolo, J.R., B.M. Kayes, M.A. Filler, M.C. Putnam, M.D. Kelzenberg, H.A. Atwater, and N.S. Lewis, *High aspect ratio silicon wire array photoelectrochemical cells.* Journal of the American Chemical Society, 2007. **129**(41): p. 12346-12347.
137. Kelzenberg, M.D., D.B. Turner-Evans, B.M. Kayes, M.A. Filler, M.C. Putnam, N.S. Lewis, and H.A. Atwater, *Photovoltaic measurements in single-nanowire silicon solar cells.* Nano letters, 2008. **8**(2): p. 710-714.
138. Bradby, J.E., J.S. Williams, and M. Swain, *In situ electrical characterization of phase transformations in Si during indentation.* Physical Review B, 2003. **67**(8): p. 085205.
139. Berger, H., *Contact resistance and contact resistivity.* Journal of The Electrochemical Society, 1972. **119**(4): p. 507-514.
140. Bulucea, C., *Recalculation of Irvin's resistivity curves for diffused layers in silicon using updated bulk resistivity data.* Solid-state electronics, 1993. **36**(4): p. 489-493.
141. Lourdudoss, S. and S.L. Zhang, *High concentration phosphorus doping of polycrystalline silicon by low temperature direct vapor phase diffusion of phosphine followed by rapid thermal annealing.* Applied Physics Letters, 1994. **64**(25): p. 3461-3463.
142. Alialy, S., H. Tecimer, H. Uslu, and Ş. Altındal, *A Comparative Study on Electrical Characteristics of Au/N-Si Schottky Diodes, with and Without Bi-Doped PVA Interfacial Layer in Dark and Under Illumination at Room Temperature.* Journal of Nanomedicine & Nanotechnology, 2013. **4**(3).